Optofluidic Nanostructures for Transport, Concentration and Sensing

by

CARLOS ESCOBEDO

B.Sc. Universidad Nacional Autónoma de México, 2000

M.A.Sc., University of Toronto, 2002

A Dissertation Submitted in Partial Fulfillment

of the Requirements for the Degree of

DOCTOR OF PHILOSOPHY

in the Department of Mechanical Engineering

Supervisory Committee

Optofluidic Nanostructures for Transport, Concentration and Sensing

by

Carlos Escobedo
B.Sc. Universidad Nacional Autónoma de México, 2000
M.A.Sc., University of Toronto, 2002

Supervisory Committee

Dr. David Sinton, Department of Mechanical Engineering, University of Victoria
Supervisor

Dr. Ned Djilali, Department of Mechanical Engineering, University of Victoria
Departmental Member

Dr. Nikolai Dechev, Department of Mechanical Engineering, University of Victoria
Departmental Member

Dr. Alexandre G. Brolo, Department of Chemistry, University of Victoria
Outside Member

Abstract

Supervisory Committee

Dr. David Sinton, Department of Mechanical Engineering, University of Victoria
Supervisor

Dr. Ned Djilali, Department of Mechanical Engineering, University of Victoria
Departmental Member

Dr. Nikolai Dechev, Department of Mechanical Engineering, University of Victoria
Departmental Member

Dr. Alexandre G. Brolo, Department of Chemistry, University of Victoria
Outside Member

This thesis presents optofluidic nanostructures for analyte transport, concentration and sensing. This work was part of a larger collaborative project between the BC Cancer Agency and the departments of Chemistry, Electrical and Mechanical Engineering at the University of Victoria. In this work, arrays of nanoholes are used as optofluidic platforms for sensing, combining the characteristics of these nanostructures for both fluidic transport and plasmonic (optical) sensing. Two different modes are considered: flow-over mode, where the sample solution containing the analyte flows on top of the nanohole arrays, and a novel flow-through mode, where the nanoholes are used as nanochannels, enabling solution transport and analyte sieving. Flow-through nanohole array operation and sensing is first demonstrated, offering a six-fold improvement in sensor response compared to established flow-over sensing formats. Through a subsequent theoretical scaling analysis and computational analyses, the benefits of the flow-through nanohole sensing format are further quantified. A first analysis is dedicated to study the enhancement offered by the flow-through operation mode using a mass transport approach. A second analysis offers an ample study of benefits and limitations of the flow-through nanostructure operation using the combination of mass transport and binding

kinetic parameters for different analytes with characteristics of clinical relevance. The mass transport analysis indicates much higher analyte collection efficiency (~ 99%) offered by the flow-through mode, compared to the flow-over platform (~ 2%). The analysis including both mass transport and binding kinetics demonstrate up to 20-fold improvement in response time for typical biomarkers.

This thesis also presents the use of the flow-through optofluidic platform as an active analyte concentrator. In combination with a pressure bias, an electric field is used to concentrate electrically charged analyte for subsequent sensing. Fluorescein enrichment of 180-fold in 60 s was achieved, and 100-fold enrichment and simultaneous surface plasmon resonance (SPR) sensing of a protein (bovine serum albumin, BSA) was demonstrated. These experiments represent the first active utilization of a nanohole metallic layer as an electrode, and the first demonstration of a photonic nanostructure achieving both concentration and sensing of analytes.

Towards the integration of optofluidic nanostructures into microfluidic environments for portable lab-on-chip diagnostic systems, this dissertation also includes the development of two nanohole array based sensing systems with simple flow-over operation. The first system consisted of a hand-held device with a dual-wavelength light source to increase the spectral diversity. The second system consisted of nanohole arrays integrated with a microfluidic concentration gradient generator for the detection and quantification of ovarian cancer antibody and antigen.

Additionally, this dissertation includes a novel technique to actuate liquids in microchannels through ground-directed electric discharges. Experiments demonstrate average fluid velocities on the order of 5cm/s and applicability of the technique in

serpentine channels, for on-demand fluid routing, to initiate a mixing process, and through an on-chip integrated microelectrode.

Table of Contents

List of Figures

Acknowledgements

I would like to express my deepest gratitude and appreciation to Dr. David Sinton, who has been not only an excellent supervisor, but also a magnificent teacher and mentor. I also wish to thank Dr. Dongqing Li for inspiring and enabling my research start-up in the microfluidics matter.

My gratitude extends to Dr. Reuven Gordon and Dr. Alexandre G. Brolo for their guidance throughout the development of this thesis, and to Dr. Ned Djilali, Dr. Rustom Bhiladvala, Dr. Carolyn L. Ren and Dr. David Erickson who have served as outstanding teachers and an excellent source of inspiration.

I would like to thank my current and past colleagues and friends for the support, insights and fun provided along my doctoral studies: Mohsen Akbari, Chih-Che Chueh, Ian Stewart, Kyle Lange, Aimy Bazylak, Laura Bianucci, Nigel David, Carmen Correa, Francisco Tovar, Antonio Espinoza, Diego Sorrentino, Slava Berejnov, Paul Wood, Brent Scarff, Alejandro de Anda, Edgar Salgado, Catalina Lartiga, Peggy White, Sue Walton, Patricio Lillo, Hector, Silvia, Gaby y Vero Sanchez, Marc Secanell, Erik Kjeang, Jorge Mendoza, Jay Sui, Te-Chun Wu, Jacqueline Ferreira, Fatemeh Eftekhari, Franco Silletta, Michael Fryer, Chiara Valsecchi, Serge Vincent, Hossein Fadaei, Myeongsub Kim, Matt Ooms, Andrew Ansell, Rajan Nirwan and Joe Wang.

I am also grateful and would like to acknowledge the financial support from the Natural Science and Engineering Research Council of Canada (NSERC), and from University of Victoria.

I also wish to express my gratitude and infinite love to my wife, Karla, for her incessant support along my doctoral program, for tolerating the most intolerable me, and for sharing this journey that we live and build together. My love and gratitude extends to my mother for her love and encouragement that allowed me to be who I am today. And last, but definitely not least, my innermost thankfulness to my daughter Ana Sofia for filling our hearts with love and joy, for making each day the best day, and for bringing home the brightest sunshine, even during rainy days.

To Ana Sofia and Chicharini

Chapter 1

Introduction

1.1 Background

Diagnosis of disease at early stages requires the detection of biomarkers (analytes) that are present at extremely low concentrations in clinical samples and, in many cases, well below the limits of detection (LOD) of current sensing technologies. Additionally, current global health challenges require not only improved LODs but also a point-of-care (POC) and point-of-use (POU) approach [1-3]. In order to satisfy these needs, the development of sensing platforms with the ability to (1) perform label-free sensing, (2) be integrated into lab-on-chip devices, (3) quantify analyte concentrations in samples, and (4) detect ultralow concentrations of analytes, is required.

Surface plasmon resonance (SPR) based biosensors have received great attention in the last decades due to their high sensitivity and low LOD, and to the possibility of integration in lab-on-chip technologies. SPR-sensing systems are already available commercially and remain improving their sensing capabilities [4-6]. As an alternative approach to established SPR sensing strategies, the use of arrays of periodic nanoholes as SPR-based biosensors has grown rapidly over the last several years [7]. Nanohole array based biosensors present additional advantages over other label-free and SPR-based sensors, including a smaller footprint, the possibility to achieve denser integration, their compatibility with relatively simple optical detection, and the potential of enhancing the current limits of detection. In many applications, nanohole arrays rely on the affinity-

based binding kinetics of the analyte to a monolayer immobilized over the sensing surface. This interaction is then transduced to a detectable signal by electrical, mechanical or optical means. The key parameter in the molecular interaction is the specificity, which is usually defined by the intrinsic affinity of the biomolecular system (e.g. antigen-antibody) and not by the sensing platform per se. From the sensing device viewpoint, the key parameters are sensitivity, response time and the limits of detection. Even when current technologies have achieved high sensitivities, challenges such as the detection of ultralow concentration of biomarkers, analyte mass transport limitations and improvement of response time still remain [8]. Specific opportunities for nanohole arrays are (1) the development of integrated microfluidic systems incorporating nanohole array based sensors for the quantification of biomarkers on-chip, (2) the use of nanohole arrays as optofluidic platforms in which both the optical characteristics of the nanostructure, and the fluid confinement inside the nanoholes are exploited, (3) the use of nanohole arrays to actively concentrate analyte in order to facilitate its detection at ultralow concentrations, and (4) new mechanisms for fluid transport in microfluidic structures.

1.2 Specific Contributions of the Candidate

The specific contributions of the candidate in each of the articles and manuscripts contained in the six appendices are listed below. The specific percentage for each contribution is also presented. Note that the contributions of the candidate and other lab personnel (students and postdoctoral fellows) are what are quantified here. The contributions of supervisors, most notably in envisioning the overall project and editing, are not included.

Appendix A. Nanoholes as Nanochannels: Flow-through Plasmonic Sensing.

The candidate designed, fabricated and implemented all the microfluidic components; integrated the nanohole arrays into the microfluidics; performed all the simulations, experiments and analysis of results on the structural behaviour studies of the nanostructure substrate; performed all the flow-through fluorescence experiments; performed the SPR sensing experiments in collaboration (70% in participation) with a graduate student from the Chemistry department; analyzed the flow-through; and wrote the bulk of the paper. The contributions represent, in percentage, the following:

- Experimental: 80%
- Analysis: 50%
- Simulations: 100%
- Paper writing: 70%

Appendix B. Flow-Trough vs. Flow-Over: Analysis of Transport and Binding in Nanohole Array Plasmonic Biosensors.

The candidate was the primary contributor. All the simulations, theoretical analysis and paper writing was completed by the candidate. The contributions represent, in percentage, the following:

- Experimental: n/a
- Analysis: 100%
- Simulations: 100%
- Paper writing: 100%

Appendix C. Optofluidic concentration: Photonic nanostructure as concentrator and sensor

The candidate was the primary contributor. All the fabrication, simulations, experiments and paper writing was completed by the candidate. The contributions represent, in percentage, the following:

- Experimental: 100%
- Analysis: 100%
- Simulations: 100%
- Paper writing: 100%

Appendix D. Integrated Nanohole Array Surface Plasmon Resonance Sensing Device using a Dual-Wavelength Source

The candidate designed and fabricated all the microfluidics; integrated the plasmonic nanostructure into the microfluidics; planned, designed and performed the biosensing experiments; analyzed the results and theoretical estimates; and wrote the bulk of the paper. The contributions represent, in percentage, the following:

- Experimental: 50%
- Analysis: 50%
- Simulations: 100%
- Paper writing: 80%

Appendix E. Quantitative Real-Time Plasmonic Sensing with an Integrated Microfluidic Concentration Gradient Generator

The candidate designed and fabricated all the microfluidics; integrated the plasmonic nanostructure into the microfluidics; performed the fluorescence characterization experiments; analyzed results; and wrote the paper. The contributions represent, in percentage, the following:

- Experimental: 50%
- Analysis: 50%
- Simulations: n/a
- Paper writing: 100%

Appendix F. Microfluidic Liquid Actuation through Ground-Directed Electric Discharge

The candidate was the primary contributor. The contributions represent, in percentage, the following:

- Experimental: 100%
- Analysis: 100%
- Simulations: 100%
- Paper writing: 100%

1.3 Motivation

Biosensing at early stages of disease impose several challenges that include the detection of ultra-low analyte concentrations in clinical samples. The LOD, in the context of sensing, can be defined as the lowest quantity of analyte that can be sensed from the absence of that analyte (zero value) within a determined confidence limit [9]. LOD enhancement is commonly a primary goal in biosensing, which is usually limited by physical and operational parameters of the technologies. An alternative strategy, however, is to provide a combined analyte concentration and sensing scheme with adequate sensitivity and LOD. This thesis presents an integrated optofluidic platform for the combined concentration and sensing of analyte that makes use of microfluidics, nanofluidics and nanohole array based sensing.

Microfluidics is the field dedicated to the study of fluid flows with volumes ranging typically on the order of nanolitres to picolitres. Microfluidics, compared to macroscale flows, exploits several phenomena such as the increased effect of surface tension, increased area-to-volume ratio, low Reynolds number and electrokinetic effects, which are the essence of most microfluidic-based applications. Capillary forces, for instance, are used in numerous applications nowadays in both basic research and commercial systems with the ability of processing valuable samples in shorter times and more efficiently [2, 10, 11]. The amount of microfluidics-related scientific publications has experienced a remarkable increase over the years since the earliest visionary works in 1990 [12]. The applications spectrum of microfluidics has extended over the years, from its origin in analytical chemistry to portable diagnostics and therapeutic medical devices [13].

Microfluidic functions are now part of many miniaturized systems and are being incorporated with other technologies, such as integrated sensing platforms, offering benefits in terms of cost, reagent sample volume usage and enhanced response times, with diverse applications including medical and point-of-care (POC) diagnostics [2, 14, 15].

Nanofluidics is the field dedicated to the study of fluid flows in nanoscale geometries. The shorter diffusion paths, higher surface-to-volume ratios and exclusive electrokinetic phenomena at the nanoscale differentiate this regime from microfluidic flows. The broad spectrum of applications of Nanofluidics includes cell physiology, membrane science, analyte concentration and sensing [16-20].

The combination of microfluidics and nanofluidics with optics has recently originated a field referred to as Optofluidics. Several publications and conference sessions dedicated specifically to this discipline have helped to distinguish it as a separate research field [21, 22]. Applications of optofluidic systems include the use of liquid core waveguiding structures [23, 24], optofluidic chips for single particle detection [25], optofluidic particle trapping [26] and optofluidic sensing [27, 28].

Ordered arrays of nanoscale holes in metal films exhibit extraordinary optical transmission (EOT) at plasmon resonant wavelengths [29, 30]. EOT, in the context of nanohole array based sensing, refers to the enhancement of the light transmitted through the nanoholes due to the excitation surface plasmons at the metallic film. Surface plasmons are electromagnetic waves which travel along the metallic surface plane, which are enabled when the momenta of the light and the plasmon are coupled via the nanostructured metallic film (e.g. nanohole array). The role of surface plasmon resonance

(SPR) on resonant transmission through nanohole arrays has motivated their application as surface-based biosensors [31, 32]. As compared to common SPR sensing, nanohole arrays present many advantages, including a smaller foot-print, lower limits of detection, denser integration, multiple analyte testing, and collinear optical detection. The characteristics of nanohole array-based sensors make them particularly well suited to planar integration with microfluidics in an on-chip format. Integration of nanohole arrays in microfluidic platforms has evolved rapidly from single-array, single-channel arrangements that facilitate fluid delivery and optical access, to multiple arrays of nanohole arrays with complex fluidic structures for multiple and parallel analyte sampling.

In this thesis, nanohole arrays are incorporated into microfluidics for analyte quantification in two different platforms. The first platform includes a microfluidic concentration gradient generator integrated with nanohole array sensors, operating under flow-over mode, in a single system. The second platform consists of nanohole array based sensors and microfluidics integrated into a handheld system with a dual-wavelength light source. Nanohole array based sensors under flow-over operation presented in this thesis and in the literature , however, have been employed in a flow-over format and, from a transport perspective, do not present clear advantages over micro-sized surface based sensor technologies. With the benefits of exclusive in-hole sensing established [33], effective analyte transport to the in-hole surface presents an opportunity to harness the rapid cross-stream diffusion characteristic of nanofluidic transport: the diffusive pathway length within the nanoholes is much smaller than that in microchannels. Therefore, the main component of this thesis was dedicated to

demonstrate an optofluidic scheme in which nanohole arrays can serve as nanochannels. The flow-through array sensor scheme introduced in this work combines the benefits of nanohole array based sensing with confined transport through the combination of nanofluidics and nanoplasmonics.

Facilitating flow-through sensing is, however, more complicated than flow-over which can be achieved with a single fluidic channel. For a given application the potential benefit offered by flow-through sensing will be a function of operating parameters and binding kinetics of the specific analyte system. Transport and binding kinetics have been studied extensively for the flow-over format typical of surface based microsensors and nanowires [34, 35]. Zimmermann *et al.* [36] investigated the analyte surface capture using a 2-D model under different input parameters such as flowrate and binding kinetics constants. Hu *et al.* [37] presented a 2-D flow-over model and demonstrated a better performance of electrokinetically driven immunoassays over pressure-driven ones in terms of reaction kinetics. Fu *et al.* [38] presented a 2-D computational model to identify operating ranges for sensitivity improvement in microfluidic heterogeneous immunoassays. Squires *et al.* [39] provided an elegant and practical analysis of microfluidic and nanowire surface-based sensors highlighting limiting factors in each case. The efficacy of a flow-through strategy has not been quantified as a function of running parameters and binding kinetics and no guidelines are available to assess applicability as a function of surface chemistry specifics. For these reasons, part of the work presented in this thesis was dedicated to compare the efficacy of flow-through nanohole sensing to the established flow-over format as a function of operating parameters and surface chemistry through scaling analysis and numerical simulation.

The reduced size and sample volumes, in addition to the scarcity of target molecules in raw samples impose limits for biosensing [40-42]. Detection of biomarkers at early stages of disease, in particular, requires ultrahigh sensitivity detectors or the use of preconcentration steps prior to detection [43, 44]. Several analyte concentration strategies have been reported in the past, including field amplified stacking [40, 45], isotachophoresis [40], electrokinetic trapping [20, 46-48], conductivity gradient focusing [49] and temperature gradient focusing [50]. Electrokinetic trapping has achieved the highest level of analyte enrichment. Due to its inherent flexibility, different approaches have been used with this technique. Concentration polarization, for instance, exploits the preferential permeation of ionic species (ionic permselectivity) of nanoporous membranes occurring at microfluidic/nanofluidic interfaces under the influence of applied electric fields [47, 51-53]. Electric field gradient focusing (EFGF) is another recently reported approach that exploits the formation of a steep field gradient in a microchannel containing a buffer and a floating electrode[48, 54, 55]. Under an applied voltage, the floating electrode acts in bipolar mode, nearly eliminating the electric field in its vicinity, which results in a non-uniform distribution of ionic species and, consequently, a non-uniform distribution of the electric field along the microchannel. The electric field gradient affects the electrokinetic transport mechanism of electrically charged species [48] (e.g. buffer ions, tracers and biomarkers). Specifically, for negatively charged molecules, the increased electric field in the vicinity of the floating electrode results in an increased electrophoretic force that eventually balances the counteracting forces imposed by the bulk flow at some position along the microchannel. The charged molecules then become quasi-stationary and are locally enriched at some

distance away from the floating electrode [54, 56]. The use of metallic nanohole array based sensors as optofluidic elements for sensing offers the possibility of using them in dual mode, as sensor and as active element for achieving analyte concentration by EFGF. The final part of this thesis was dedicated to demonstrate this novel and unique functionality of optofluidic nanohole arrays based sensors.

1.1.1 Objective

The general objective of this thesis is to develop and integrate microfluidics and nanofluidics with existing nanophotonics into an optofluidic platform for biosensing applications. Specific objectives include the development of: (1) a microfluidic flow-over platform to be integrated with a nanohole array based sensor to serve as biosensor for the detection and quantitative assessment of biomarkers for medical diagnostics; (2) the study, development and testing of flow-through nanohole array-based platforms for biosensing and analyte preconcentration; and (3) the study of the mass transport and reaction kinetics associated with the flow-through nanohole array based sensing. In order to achieve the objectives of this thesis, experimental and computational approaches were employed. The experimental element of this thesis comprises fabrication, characterization, integration and testing of both the microfluidics and the nanohole arrays. Techniques used to achieve the experimental goals of this thesis included soft lithography microfabrication, focused ion beam lithography, fluorescence microscopy, SPR spectrometry, and imaging techniques. The computational element of this thesis consists of simulations via finite element analysis (FEA) using ANSYS and COMSOL software. This thesis represents the mechanical, microfluidic and nanofluidic components

of a collaborative project between the BC Cancer Agency and the departments of Chemistry, Electrical and Mechanical Engineering at the University of Victoria.

1.1.2 Structure

The dissertation presented here is organized into 3 chapters. Chapter 1 presents the general and specific objectives and motivation of the thesis, an overview of the theoretical background from previous research relevant to this work, and an overview of the experimental methods utilized to achieve the research goals of this work. Chapter 2 provides a summary of each of the peer-reviewed journal publications resulted from the research of this thesis. Chapter 3 presents the conclusions, a summary of the contributions and a brief discussion on the anticipated future work related to this thesis. The bulk of this thesis is presented in six Appendices. Each appendix is a complete scientific journal article which is either published, in press, or presently under review.

1.2 Theoretical Background

1.2.1 Transport phenomena at the micro- and nanoscale

Fluid transport considered in this work is based in the continuum assumption where the mean free path is significantly smaller than the characteristic dimension of the flow [57]. This is valid for typical liquid flows in the channels used in this study, which are greater than 100 nm in cross section. In such cases, the mass continuity equation can be expressed as follows:

$$\frac{\partial \rho}{\partial t} + \nabla \cdot \left(\rho \vec{V} \right) = 0 \tag{1}$$

where ρ is the density of the fluid and $\vec{V}$ is the velocity vector. Assuming incompressibility conditions, this equation simplifies to:

$$\nabla \cdot \vec{V} = 0 \tag{2}$$

The velocity field for a Newtonian fluid may be characterized by the Navier-Stokes equations which, assuming incompressibility conditions can be expressed, in vectorial form, as [58]:

$$\rho \left(\frac{\partial \vec{V}}{\partial t} + \vec{V} \cdot \nabla \vec{V} \right) = -\nabla p + \mu \nabla^2 \vec{V} + \rho \vec{g} \tag{3}$$

where p is the pressure, μ is the dynamic viscosity of the fluid and $\vec{g}$ is the gravitational acceleration. The Reynolds number is a dimensionless quantity that describes the ratio of inertial to viscous forces on flow behaviour [58] and can be defines as:

$$\mathrm{Re} = \frac{\rho U l}{\mu} \tag{4}$$

where U is the average velocity of the fluid and l is the characteristic length. Fluid flows at both micro- and nanoscale experience low Reynolds numbers even at high fluid flow velocities, which reduces the Navier-Stokes equations to the Stokes equation [57]:

$$-\nabla p + \mu \nabla^2 \vec{V} = 0 \tag{5}$$

Mixing and other transport phenomena at the small scales are dominated by diffusion. A traditional example of this is the existence of co-laminar flows in microchannels [59]. Assuming constant diffusivity, the conservation of individual species is dictated by the convection-diffusion equation [57]:

$$\frac{\partial c_i}{\partial t} + \vec{V} \cdot \nabla c_i = D_i \nabla^2 c_i \tag{6}$$

where c_i is the species concentration and D_i is the diffusivity of i^{th} the species. As particles with smaller hydrodynamic diameters will diffuse more rapidly than larger particles, the advection-to-diffusion ratio is of interest in the mass transport analysis in micro- and nanofluidic flows. These quantities may be related by the Peclet (*Pe*) dimensionless number which may be expressed as [58]:

$$Pe = \frac{Ul}{D} \tag{7}$$

Pressure-driven flow is simple to apply and is the most common approach to transport fluids. However, it presents some challenges in integrated microfluidic/nanofluidic systems. In microfluidic systems, the required pressure gradients are very high and pressure driven flow is only practical over small channel lengths (up to a few hundreds of nanometers). In the context of an array of nanoholes, pressure driven flow may be applied to drive fluid over an array of nanoholes in a microfluidic channel (flow-over) or potentially through the nanoholes as schematically shown in Figure 1.1.

In this thesis work, the particular nanohole array structure, as shown in Figure 1.1, is of particular interest. Background on the unique fluid mechanics of this structure is summarized below.

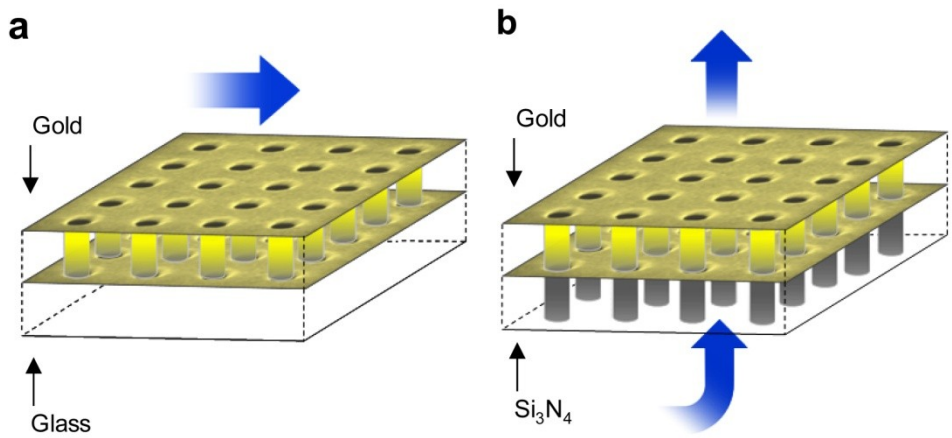

Figure 1.1 Schematic representation of the two different flow configurations of the sensing platform: a) flow-over and b) flow-through.

The pressure difference of a very small Reynolds number flow through a circular opening in a membrane with width or length, l, much greater than its thickness, t (i.e. $l >> t$)is proportional to the volume flow rate [60]. However for a membrane with finite thickness and an array of holes, two correction factors are required in addition to frictional losses: the influence of the flow of adjacent nanoholes and the additional pressure drop occurring right before the entrance of the nanohole (significant at higher laminar flow rates) [61, 62]. The resulting equation is as follows:

$$\Delta p = Q\left(\frac{3\mu}{r^3}\right)\left(1+\frac{0.85t}{r}\right)\left(1-0.34\chi^{\frac{3}{2}}\right)+Q^2\left(\frac{\rho}{4\pi^2 r^4}\right) \tag{22}$$

where p is the pressure, Q is the flow rate; μ is the fluid viscosity; r the nanohole radius; t is the membrane thickness; χ is the membrane perforated fraction; and ρ is the fluid density.

The maximum allowed pressure of the substrate before failure can be calculated using the following equation adapted from Rijn et al. [63]:

$$\Delta p_{\max} = 0.514 \cdot K \cdot \left(\frac{t}{l}\right) \cdot \sigma_m \cdot \sqrt{\frac{\sigma_m}{\mathrm{E}}} \tag{23}$$

where K is the non-perforated fraction of the membrane; l is the characteristic length of the membrane width or length, σ_m is the yield stress of the membrane; and E is the Young's modulus of the material.

In microscale flows, surface forces are dominant compared to inertial forces [64]. Surface tension, a measurement of the cohesive energy at an interface, results from the preferential attraction of molecules to one side of the interface. The capillary pressure due to surface tension at an interface is defined by the Young-Laplace equation as:

$$\Delta p = \frac{2\sigma}{r_m}\cos\theta \tag{8}$$

Where Δp is the pressure across the interface, σ is the surface tension, r_m is the mean radius of curvature of the meniscus and θ is the liquid/gas interface contact angle at the solid. For laminar flows, the penetration length of a fluid driven by capillary force can be described by the Washburn equation [65, 66] as follows:

$$L^2 = \frac{\sigma r_H t}{2\mu}\cos\theta \tag{9}$$

where L is the liquid penetration length, σ is the surface tension t is the time, and r_H is the hydrodynamic radius of the microchannel.

As an alternative to pressure-driven flow, electrokinetic phenomena have been employed to generate microfluidic flows in a wide range of applications [67-72]. When a solid surface is brought in contact with a polar medium, the interface acquires a net surface charge with a preferential distribution of ions. This phenomenon causes two

localized layers of neutralizing counterions in the vicinity of the solid which is known as the Electric Double Layer (EDL). The first layer on the EDL is formed by immobile counterions in contact with the solid which is known as the compact layer. The second layer is formed by a mix of coions and counterions known as the diffuse layer, where the concentration of counterions predominates. A schematic representation of the EDL is shown in Figure 1.2. In the earliest models, the EDL was treated as a capacitor with ions absorbed onto the surface of the solid. Later, Gouy and Chapman provided a more complex model by introducing a diffuse layer where the ionic concentration and, therefore, the electric potential decrease exponentially away from the solid surface [57]. The latest model of the EDL is the Gouy-Chapman-Stern model in which an intermediate layer with a linear electric potential distribution is introduced between the inner (IHP) and the outer (OHP) Helmholtz planes. The potential at the slipping plane in the EDL is usually referred to as the zeta potential (ζ).

The distribution of charged species in the vicinity of a charged surface is a balance between electro-migration, convection and diffusion and can be expressed by Fick's law as follows:

$$j^* = -\nu z F c \nabla \phi - D \nabla c + c\vec{u} \tag{10}$$

where j^* is the molar flux, ν is the ion mobility, z is the valence charge, F is Faraday's constant, c is the species concentration and $\vec{u}$ the velocity. Diffusivity is described by the Nerst-Einstein equation:

$$D = RT\nu = kN_A T\nu \tag{11}$$

where R is the universal gas constant, T is the temperature, k is the Boltzmann's constant and N_A is Avogadro's number.

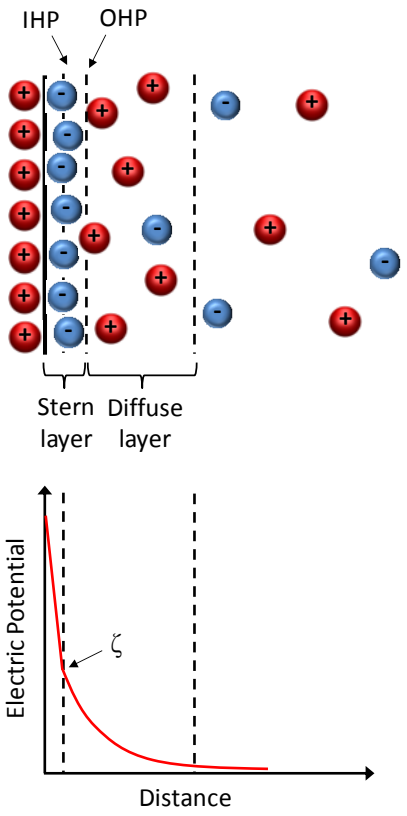

Figure 1.2 Schematic representation of the structure of the Electric Double Layer. The inner (IHP) and outer (OHP) Helmholtz planes are indicated.

The ionic distribution within the diffuse layer of the EDL can be expressed by the Boltzmann distribution:

$$c_{\pm} = c_0 \exp\left(\frac{\pm ze\phi}{kT}\right) \tag{12}$$

where c_0 is the bulk electrolyte concentration, e is the elementary charge and ϕ is the electrostatic potential. The ionic distribution and the electric potential are related by the Poisson's equation:

$$\nabla^2\phi = -\frac{\rho_E}{\varepsilon} = -\frac{F}{\varepsilon}\sum_{i=1}^{N} z_i c_i \tag{13}$$

where ρ_E is the electric charge density, ε is the permittivity of the solution and z_i and c_i are the valence and concentration of the i^{th} species respectively. Equations 12 and 13 can be combined to produce the Poisson-Boltzmann equation which describes the variation of the electrostatic potential with the ionic distribution:

$$\frac{d^2\phi}{dx^2} = -\frac{F}{\varepsilon}\sum_{i=1}^{N} z_i c_i \left(\frac{z_i e\phi(x)}{kT}\right) \tag{14}$$

which, for symmetric electrolytes can be reduced to:

$$\frac{d^2\phi}{dx^2} = \frac{2zFc_0}{\varepsilon}\sinh\left(\frac{zF\phi(x)}{RT}\right) \tag{15}$$

Assuming the surface potential is small, equation 15 results in the Debye-Hückel approximation [57]:

$$\frac{d^2\phi}{dx^2} = \frac{\phi}{\lambda_D^2} \tag{16}$$

where λ_D^2 is the Debye length defined as:

$$\lambda = \sqrt{\frac{\varepsilon RT}{2F^2 z^2 c}} \tag{17}$$

which is the ionic screening length from the solid-liquid interface, typically on the order of nanometers.

Electroosmosis results from viscous drag caused by the attraction of ions in the diffuse layer under an applied voltage along the length of a microchannel containing fluid was first reported by Reuss in 1809 [73]. The magnitude of the resulting electroosmotic flow (EOF) depends, among other variables, on the zeta potential, which is the electrical potential at the slipping plane between the compact and the diffuse layers in the EDL.

The electric body force per unit volume, expressed in terms of the electric charge density and the external electric, E, as $f = \rho_E E$, can be included into the momentum equation which, neglecting pressure gradients and gravitational and inertial effects, reduces to:

$$\mu \nabla^2 u = -\rho_E E \tag{18}$$

Assuming a small diffuse layer thickness, equation 18 can be reduced to a one-dimensional form:

$$\mu \frac{\partial^2 u}{\partial y^2} = \varepsilon \frac{\partial^2 \phi}{\partial y^2} E_x \tag{19}$$

where x is the axis along the solid-liquid interface and y is the axis normal to the solid surface, typically the wall of a microchannel. The above equation can be integrated twice, using $\partial u / \partial y = \partial \phi / \partial y = 0$ when $y \to \infty$ for the first integration, and $u(0) = 0$ and $\phi(0) = \zeta$ (zeta potential) and $u(\infty) = U$ and $\phi(\infty) = 0$ for the second integration, resulting in the average electroosmotic velocity equation:

$$U_{EO} = -\frac{\varepsilon \zeta E_x}{\mu} = \mu_{EO} E_x \tag{20}$$

known as the Helmhotlz-Smoluchowski equation, where μ_{EO} is referred to as the electroosmotic mobility.

The motion of an electrically charged molecule due to an externally applied electric field is known as electrophoresis. Similarly to electroosmosis, an average electrophoretic velocity expression can be obtained:

$$U_{EP} = vzFE_x = \mu_{EP} E_x \tag{21}$$

where μ_{EP} is the electrophoretic mobility of the associated ionic species.

Of particular interest in the work presented in this thesis is the integration of nanohole array based sensing into a microfluidic format. As mentioned in section 1.1, two operation modes, related to fluid transport, are considered. In the first mode, hereafter referred to as flow-over, the fluid containing the sample analyte is transported over the sensor. In the second, the flow-through mode, nanohole arrays represent arrays of nanochannels on the order of 100 to 300 nm in diameter. Both formats are schematically shown in Figure 1.1. In addition to the traditional electrokinetic phenomena, recent theoretical studies report the effects of induced-charged electrokinetics in ideally polarizable materials [74-77]. The surface of the nanoholes in contact with an electrolyte may develop an induced-charged electric double (ICEDL) layer under an applied electric potential. The ICEDL may in turn result in induced charge electroosmotic (ICEO) flow. The development of the IDCL can be conceived as a first-order energy storage system, in analogy to a resistor-capacitor (RC) electric circuit, in which the product RC provides the characteristic charging timescale τ [59, 74].

In the case of the ICDL in the nanoholes, this timescale has an order of magnitude of $\sim \lambda_D l_n / D$, where λ_D is the Debye length, l_n is the depth of a nanohole and D is the ionic diffusivity [74, 78]. The development of the ICDL results in two counter-rotating symmetric induced-charge electroosmotic (ICEO) flows above the bipolar surface. Within the nanohole region, the net velocity resulting from the ICEO flows is null. The slip velocity generated by the ICEO flows, at the anodic region of the metallic nanohole, may counteract the bulk flow with a magnitude of $\sim \varepsilon E_0^2 l_n / \eta$ [74]. The physics of ICEO in nanostructures is rich and rapidly developing.

1.2.2 Surface Plasmon Resonance Sensing

Surface plasmons are quasiparticles commonly described as oscillating electromagnetic waves occurring at the interface of a metal and a dielectric. The electromagnetic waves arise by means of the coupling of the electromagnetic field to electron plasma oscillations of the conductor. The two relevant varieties of surface plasmons for sensing are propagating surface plasmon polaritons (SPPs) and localized surface plasmons (LSPs) [79]. A SPP is classically defined as an electromagnetic wave existing at the interface between a metal and a dielectric, which can be alternatively understood as a propagating transverse magnetic (TM) waveguide mode that decays exponentially into the metal and towards the dielectric in a normal direction to the interface. In order to achieve plasmon excitation, a matching condition between the incident light and the surface plasmon wave vectors is required:

$$\vec{k}_{light} = \vec{k}_{SPP} \tag{22}$$

In such matching condition, the momentum of the SPP can be expressed as:

$$k_{SPP} = \frac{\omega}{c}\sqrt{\frac{\varepsilon_d \varepsilon_m}{\varepsilon_d + \varepsilon_m}} \tag{23}$$

where ω and c are the angular frequency and the speed of light respectively, ε_d is the relative permittivity of the dielectric and ε_m is relative permittivity of the metal. To support SPPs at the metal-dielectric interface, the SPP wave-vector must be larger than the dielectric wave-vector, which requires $\mathrm{Re}[\varepsilon_m] < -\mathrm{Re}[\varepsilon_d]$. The consequence of this is that light cannot couple directly as a SPP at the metal film. Several approaches have been used in the past to achieve SPP excitation, including the use of an optical prism through an index matching fluid. In this case, widely known as the Kretschmann configuration of

attenuated total reflection (ATR) and shown in Figure 1.3 [80], a light beam is directed on a glass prism to acquire a particular angle for achieving SPP excitation and can be expressed as:

$$k_{SPP} = k_0 n_p \sin\theta_{SPP} \tag{24}$$

where k_0 is the momentum of light in vacuum, n_p is the refractive index of the prism and θ_{SPP} is the angle required for SPP excitation.

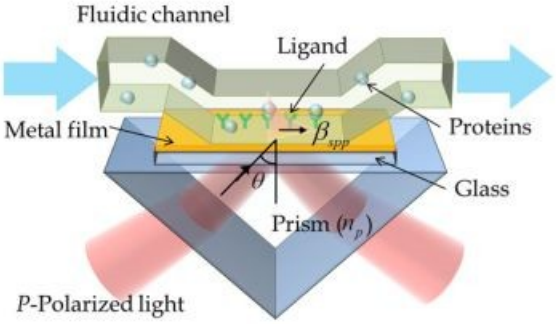

Figure 1.3 Schematic representation of the traditional Kretschemann configuration utilized for biosensing through surface plasmon resonance [80].

Rectangular arrays of subwavelength nanoholes in metal films also support SPPs and exhibit unique optical transmission characteristics at resonant wavelengths [30]. In 1998 Ebbesen and co-workers reported on the extraordinary optical transmission (EOT) through arrays of nanoholes in different metals from the coupling of light to SPPs [29]. In the observations reported by Ebbesen the absolute transmission at resonant wavelengths were significantly higher than the light that impinged on the holes, with orders of magnitude higher than predicted by earlier theory. For this reason, the role of surface plasmon resonance (SPR) on resonant transmission through nanohole arrays has

motivated the use of nanohole arrays as surface-based sensors. Figure 1.4 presents a schematic conception of SPPs and EOT in metallic nanohole arrays.

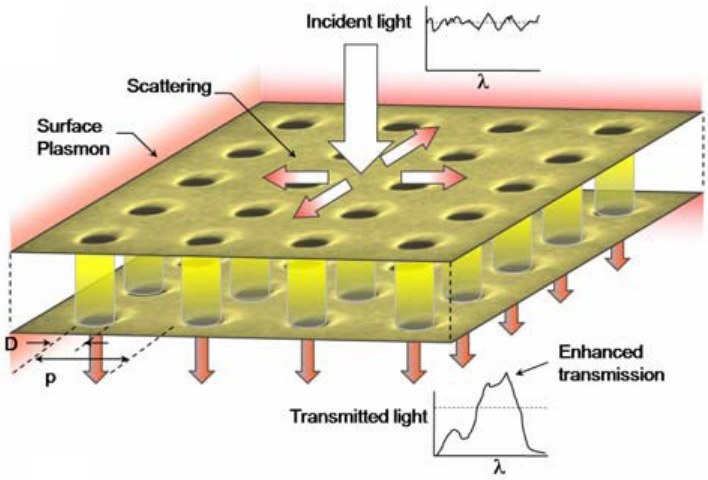

Figure 1.4 Schematic representation of EOT and SPPs in nanohole arrays. The transmission of light is enhanced at specific wavelengths after passing through an array of nanoholes in a metal film.

The requirement for resonance in this type of nanostructure is imposed by the Bragg condition as follows:

$$k_{SPP} = n_{eff}\sqrt{\frac{i^2}{a^2}+\frac{j^2}{b^2}} \tag{25}$$

Where n_{eff} is the effective refractive index, i and j are the whole number resonance orders along the x and y direction, and a and b are periodicities of the holes in the x and the y direction, respectively [81].

The position of the resonant peak in the transmission spectrum is related to the periodicity that, in the case of a square nanohole array, is:

$$\lambda_R = \frac{a_0}{\sqrt{i^2 + j^2}} \sqrt{\frac{\varepsilon_d \varepsilon_m}{\varepsilon_d + \varepsilon_m}} \tag{26}$$

The first demonstration of the nanohole array structure as an SPR-based sensor was presented by Brolo in 2004 [31], and has been followed by many others [82-88].

1.3 Experimental Methods

1.3.1 Nanohole array fabrication

For this thesis, the nanohole arrays for both modes were fabricated using Focused Ion Beam (FIB) lithography. FIB milling or simply as FIB, is a maskless etching technique that utilizes a vacuum chamber, a liquid metal ion source, an ion column, a sample stage with five degrees of freedom, detectors, a gas delivery system and a computer-based control system [89]. The most common source metal ion used in FIB milling is Gallium (Ga), but Au/Si and Au/Si/Be alloys may also be used when lighter mass ions are required. Figure 1.5 presents a simplified schematic representation of a FIB system. A beam of positive ions is produced by the system and focused onto a sample held on place on the sample stage. The beam can be used to either visualize or mill the sample by adjusting the ion current, with milling requiring the highest current. Ions from the focused beam impact the sample, removing material by momentum transfer.

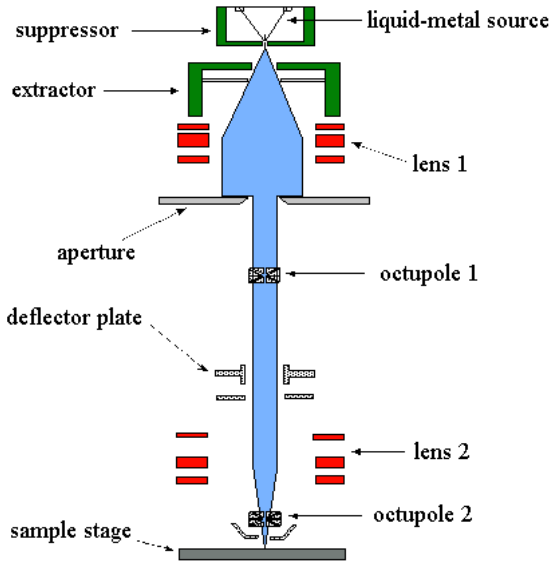

Figure 1.5 Simplified schematic of a focused ion beam (FIB) system.

Two different types of nanohole arrays were employed in this thesis. In both cases, FIB technique was utilized to fabricate the holes. The first type involved dead-ended holes milled on a gold-on-glass substrate. The nanohole arrays used in the experiments reported in the first journal publication related to this thesis were fabricated by members of the project group from the Electrical Engineering Department at University of Victoria. The nanohole arrays used in the rest of this thesis were fabricated by the candidate and are part of the experimental work reported here.

Arrays of through nanoholes were fabricated using 100 nm thick Si_3N_4 free-standing membranes coated with a 100 nm layer of gold via a 5 nm Ti/W adhesion layer. The general milling parameters were as follows: the gallium ion beam was set to 40 keV for milling with a beam current of 30 pA, the typical beam spot size was 10 nm, and the dwell time of the beam at one pixel was 10 µs. The arrays consisted of 30 × 30 nanoholes with periodicities between 450-700 nm. The nanohole arrays were visualized using FIB

and SEM from both sides to assure through-hole fabrication. Figure 1.6 shows a sample image of through-hole nanohole arrays fabricated in this work.

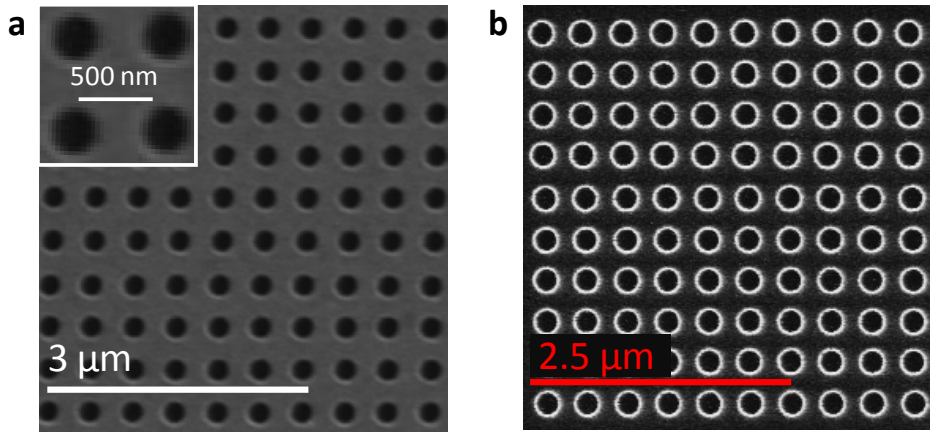

Figure 1.6 Fabricated through nanohole arrays from: a) Au side and b) the Si_3N_4 side.

1.3.2 Photolithography

Photolithography is a common microfabrication technique using light to imprint a pattern from a photomask to a light sensitive photoresist. Positive photoresists become soluble while negative photoresists become insoluble after UV light exposure. The thickness of the photoresist layer is usually a fabrication limiting parameter. The minimum feature size possible by photolithography is dictated by light scattering and diffraction at the edges of the photomask. The size of the affected area due to diffraction depends on the wavelength of the incident light and the thickness of the photoresist layer, which can be estimated by $\delta \approx 3\sqrt{\lambda h_{ph}}$, where δ is the average width of the diffraction zone, λ is the wavelength of the incident light and h_{ph} is the height of the photoresist layer. For narrowly spaced features, a spacing of $>2\delta$ is recommended. Microfabrication using

photolithography techniques is well established and further details, not included in this thesis, can be found elsewhere [90, 91].

1.3.3 Fluorescence Microscopy

Fluorescence microscopy is based on the excitation of a fluorophore by electromagnetic radiation which results in the emission of a photon [92]. Fluorescence can be described in three stages: (i) a photon is absorbed by a fluorophore, increasing its energy to an excited state; (ii) the fluorophore remains in this excited state for a finite period, called the fluorescence lifetime, which typically lasts 1-10 ns; (iii) the fluorophore then liberates a photon returning to its original energy state [93]. Part of the absorbed energy from the photon is dissipated through interactions with other molecules, conformal changes, and energy dissipating vibrations [93]. During this process, the photon is emitted at a lower energy and wavelength according to the following photon energy equation, $E = hc/\lambda$, where h is the Planck's constant, c is the speed of light in vacuum and λ is the wavelength of the associated electromagnetic wave. The wavelength difference between the absorbed and emitted photon has been referred to as the Stokes' shift [93] which is the principle of the fluorescence-based experiments presented in this work.

The experimental setup under which fluorescence microscopy operates is schematically shown in Figure 1.7. A filter cube encloses two perpendicular filters and a dichroic mirror for the selective transmission of specific wavelengths. The filters allow only the specific light at the excitation and emission wavelength range of the fluorescent sample. The excitation filter allows only the transmission of excitation wavelength. The dichroic mirror is transparent to longer wavelengths but reflects shorter wavelengths,

directing the light from the emission filter to the microscope objective and the sample. After Stokes' shift occurs, the light from the sample is transmitted back through the dichroic mirror to the emission filter. A cooled charged-coupled device (CCD) camera is used to visualize and record the fluorescent images.

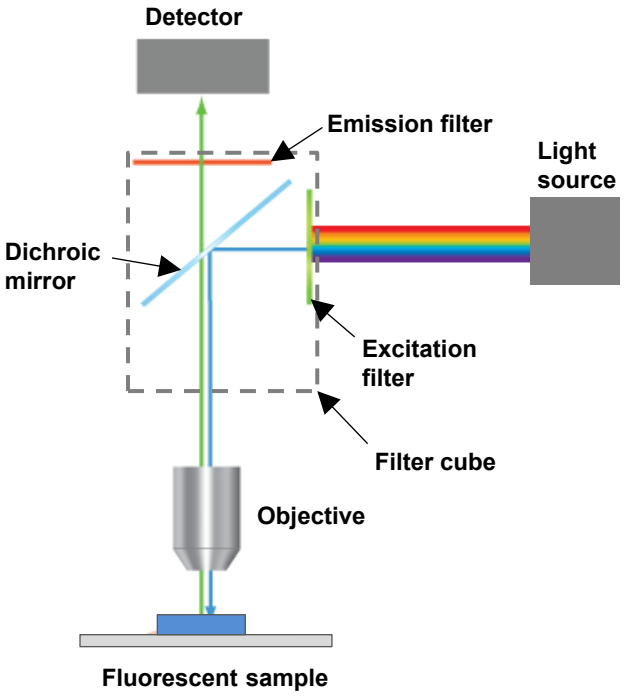

Figure 1.7 Simplified schematic of a fluorescence microscope.

1.3.4 Nanohole Array Based Surface Plasmon Resonance

Nanohole array based sensing is a label-free sensing where analyte detection may be achieved through imaging or by means of SPR spectroscopy. In imaging techniques, the intensity of a single-wavelength light source, transmitted through the nanohole array, is acquired and monitored (e.g. by means of a CCD). The transmitted light intensity changes in response to changes in the refractive index at the metal-dielectric interface. In

SPR spectroscopy, the spectrum of the transmitted light is acquired and sensing is achieved by tracking the peak-shift at the plasmon resonance wavelength (from the light transmission spectrum) in response to changes in the near-surface refractive index. Figure 1.8 shows schematics of the experimental setups and sample results for both modalities. Figure 1.8a shows a schematic representation of the main components of the imaging-based technique used in the experiments presented here. A CCD camera acts as the sensor array. Both a Helium-Neon (He-Ne) laser and LEDs with broad incoherent illumination as well as simple biasing circuitry were used as the light source, and controlled by a PC. A chip assembly enclosed the substrate with the nanohole array sensors and a microfluidic chip was responsible for interfacing the gold surface with selected test solutions. Microfluidic solution delivery was achieved by means of a microscrew syringe pumps or hydrostatic means via 1/16 inch outer diameter Teflon tubing. The CCD camera and the light source were positioned orthogonally with respect to the chip assembly. Light source control and image acquisition were achieved by a separate computer via MATLAB. Sensing is achieved by monitoring the change in intensity of the transmitted light as a response to an event at the metal-dielectric interface. Figure 1.8b shows a schematic representation of the setup used for the SPR spectroscopy technique. The nanohole arrays, as mentioned above, are enclosed into a chip assembly integrating both the optical and the microfluidic components. Different lenses and optical arrangements (e.g. microscope objectives, collimators, etc.) are used for obtaining the proper intensity and illumination coverage at the nanohole array (i.e. obtaining a response with sufficient amplitude and an adequate signal-to-noise ratio). The probe from the spectrometer is positioned orthogonally under the chip assembly in order to read the

transmitted spectrum from the nanohole array. The spectrum shown in Figure 1.8b is a sample spectrum from experiments. Sensing is achieved by tracking the peak-shift from the starting resonant wavelength.

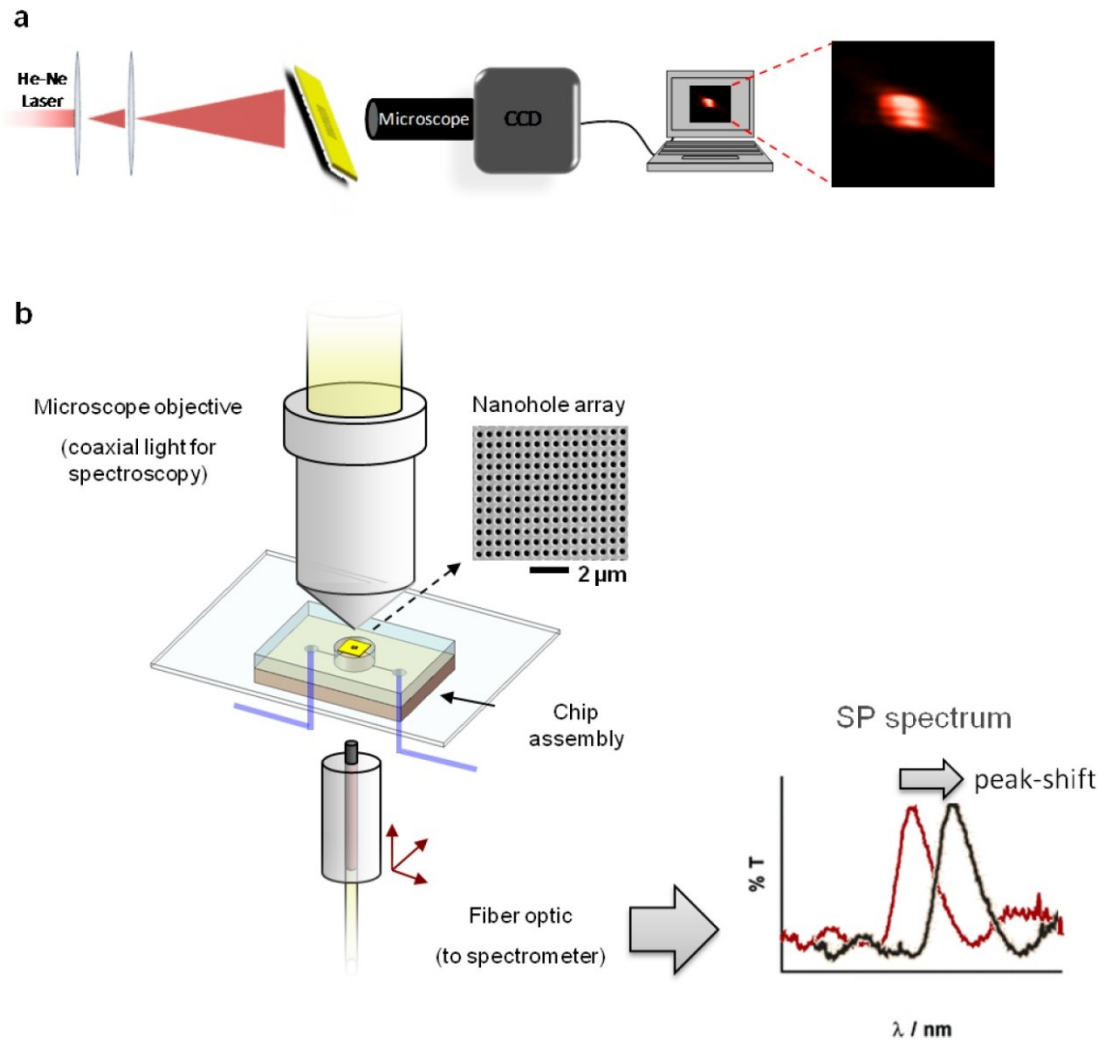

Figure 1.8 Schematics of the experimental setups used for SPR sensing. a) SPR imaging technique. b) SPR spectroscopy.

1.3.5 Mechanical Stability of the Nanohole Arrays Substrate

The flow-through sensing scheme discussed in Section 1.2, which is a fundamental part of this thesis, involved fluidic transport through nanoscale holes. Under flow-through operation, breakage of the substrate containing the nanohole arrays may occur due to fluid transport and associated pressures (i.e. capillary pressure and fluid pressure). Therefore, the mechanical behaviour of the substrate was studied using theoretical, numerical and experimental approaches. Experimentally, the deflection of the substrate, a gold-on-Silicon-Nitride (Si_3N_4) TEM analysis membrane, was studied using the setup shown schematically in Figure 1.9.

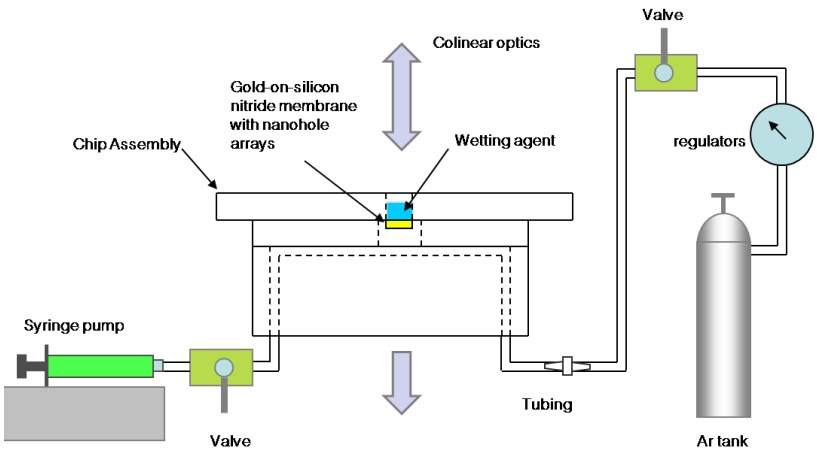

Figure 1.9. Schematic representation of the experimental setup to facilitate flow-through nanohole arrays.

The results from this study, as well as the results from the theoretical calculations and computer simulations are presented in section 2.1.

Chapter 2

Summary of Contributions

This chapter presents a synopsis of the main contributions in this dissertation. The contributions, in full, are included in the six journal articles and manuscripts provided in Appendixes A-F.

2.1 Nanoholes as Nanochannels: Flow-through Plasmonic Sensing

Nanohole array based sensing, compared to common SPR sensing, offers several advantages including smaller foot-print, denser integration, potential for the simultaneous measurement of multiple analytes (multiplexing) and collinear optical detection. Due to these characteristics, nanoholes are suitable for planar integration with microfluidic systems in on-chip formats. In all the sensing platforms involving nanohole arrays reported prior to this work, the fluids containing the analyte of interest were transported over arrays comprised of dead-ended nanoholes (i.e. in a flow-over format) as shown in Figure 1.1a . Thus, from a mass transport viewpoint, these nanostructured sensors failed to harness the potential benefits provided by flow-through operation. Potential benefits include enhanced transport of reactants via the confinement of analytes within the nanoholes (shorter diffusive lengthscales) and solution sieving. Additionally, from the sensing perspective, recent studies revealed the important role of the inner surface of the nanoholes for sensing [33].

The present work involved the development of a new flow-through SPR-sensing scheme in which nanoholes serve as channels. This work was done in collaboration with

members of the departments of Electrical Engineering Department and Chemistry. Specifically, the nanohole array fabrication and part of the flow-over experiments were done by Fatemeh Eftekhari; solution preparation, sensing and biosensing experiments and data analysis were carried out by Jacqueline Ferreira; flow-through validation experiments, sensing, and biosensing experiments, microfluidic design and fabrication, experimental set-up implementation and the bulk of the paper text body was completed by the candidate.

A first stage of this work included the mechanical characterization of the substrate used to fabricate the nanohole arrays: transmission electron microscopy (TEM) analysis Si_3N_4 membranes. The goal of this stage was to determine a range of working fluid pressures that the substrate could tolerate under flow-through operation since the membranes used in this thesis had a large surface-to-thickness ratio (area: 500 μm by 500 μm; thickness: 100 nm) and the material is brittle. Working pressures beyond this limit would compromise the structural integrity of the substrate. The mechanical behaviour of a gold-coated Silicon Nitride membrane was studied using theoretical, numerical and experimental approaches.

The deflection of the membrane and the implications of this deflection for the flow transport across the membrane were studied using computational simulations. The membrane deflection and stress distribution was studied using COMSOL (COMSOL Inc., Burlington, MA) and ANSYS (ANSYS Inc., PA). Operational pressures and flow rates were obtained using theoretical formulations described in Section 1.2.1. CAD models, mesh and material properties of the membrane were generated using COMSOL and ANSYS. Pressures ranging from 0 to 20 psi at the bottom face and fixed supports at the four side faces were used as boundary conditions. Experimentally, a membrane was

deflected using the setup of Figure 1.9 applying constant pressures in the range of 0 to 20 psi. The deflection of the membrane was estimated using in-focus depth of field measurements. The estimation was achieved by focusing a nanohole array at the center of the membrane prior and during deflection, and by recording the distance between these focal planes in the direction normal to the observation plane. The measurement was performed using the microscope software (n = 3). In Figure 2.2, maximum displacements using experimental and computer-based simulations are shown.

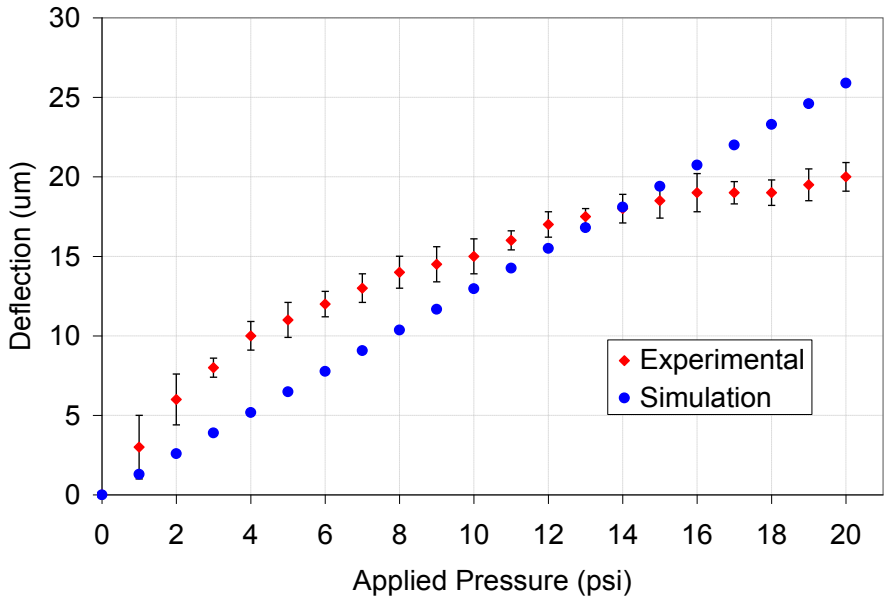

Figure 2.1. Membrane maximum deflection results using experimental and computer-based simulations methods.

Although there is a discrepancy in the trends in Figure 2.2, the magnitudes are similar. From these results, a pressure of 10 psi, corresponding to half of the maximum pressure value before failure obtained from the studies, was selected as working pressure for flow-through experimentation. Figure 2.3a shows simulation results of stress distribution under 10 psi of pressure. The membrane model was fixed at the four sides, in analogy to real

membranes which are fixed to a Si frame. For this pressure, the simulations showed a maximum stress of ~ 400 MPa (at the fixed sides of the nitride) which is lower than the Si_3N_4 maximum flexural strength (~700 MPa [94]), which confirms the chosen pressure value to be adequate for flow-through experimentation. Figure 2.3b shows an actual picture of a membrane under deflection, and 2.3c an image of the deflection simulation. The deflection estimate, using both the computational and the experimental approaches, were found to be in agreement, estimating a deflection on the order of ~15 µm under the applied pressure of 10 psi. The shape of the nanoholes in the deflected membrane was also investigated. The deformation of the holes was found to be negligible using this particular membrane geometry, as shown in Figure 2.3d. However, for smaller membranes, the membrane deformation may induce a change in the nanoholes cylindricity. The potential shape distortion of the nanoholes opens up the possibility of developing a pressure-tunable photonic structure in the future.

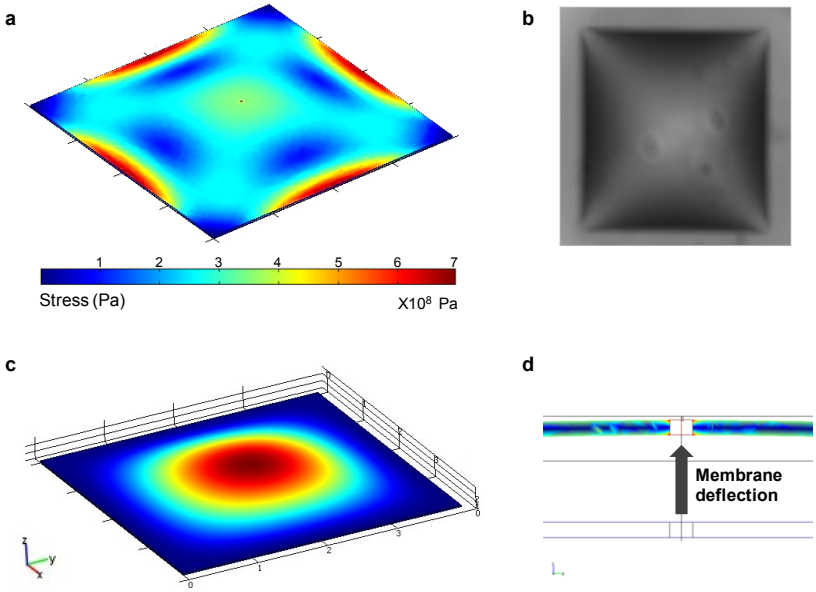

Figure 2.2. a) Stress field results of membrane deflection simulation, b) actual picture of deflected membrane under an applied pressure of 10 psi, c) simulated deflection of the membrane, and d) detail of the deflected membrane at a nanohole.

The second stage of the work presented in this section included the demonstration of both flow-through transport and sensing using nanohole array based SPR sensing in the flow-through format. For these purposes, nanohole arrays with different fabrication parameters and different periodicities were fabricated in an attempt to determine the proper FIB milling parameters. The arrays were 30 by 30 holes with periodicities ranging between 450 and 700 nm. Fluorescent dye was used for flow-through transport assessment. Under an applied pressure of 10 psi, flow-through was achieved in a couple of the arrays [95]. The lack of flow from the other three arrays corresponded to the variation in fabrication parameters (i.e., the milling time used to fabricate those arrays did not allow the formation of through holes).

The efficacy of the flow-through format was tested by detecting surface adsorption events. The formation of a mercaptoundecanoic acid (MUA) monolayer was monitored using the flow-through nanohole array SPR sensing. The MUA adsorption followed first-order kinetics with observable surface adsorption constant (k_{obs}) of 0.426 min^{-1}, which denotes an enhancement compared to the rate in flow-over schemes reported previously [96]. More notably, the results demonstrate label-free surface-based detection with flow-through nanohole arrays. To demonstrate the efficacy of flow-through sensing, this approach was compared to traditional flow-over sensing at similar flow rates. The flow-through experiment indicated a characteristic rate constant of $6.4x10^{-3}$ min^{-1} while the flow-over case was $6.4x10^{-3}$ min^{-1}. With these experiments, the flow-through operation demonstrated a 6-fold improvement in response time compared to the flow-over case. A second sensing experiment was performed in order to test the capability of the platform to sense the sequential multilayer assembly of biomolecules, as required for biosensing

applications. For this purpose, the sequential assembly of a dithiobis(succinimidyl) undecanoate (DSU) monolayer and the cancer biomarker PAX8 specific monoclonal antibody were demonstrated with the flow-through scheme. The observed shifts, on the order of several nanometers, were readily observable with relatively simple infrastructure. These results demonstrate that the flow-through nanohole array based sensors may be employed to detect multiple adsorbed layers, and are thus applicable to typical biosensing schemes.

Full details on this study are provided in Appendix A or [95].

2.2 Flow-Trough vs. Flow-Over: Analysis of Transport and Binding in Nanohole Array Plasmonic Biosensors

Operating in flow-through mode, nanohole arrays have the potential to enable analyte sieving, a capacity that is unique among surface based optofluidic sensors. Analyte sieving refers to the ability of the sensor to increase the capture efficiency of analyte in a fluid. Results of the previous section indicated that flow-through operation enabled a six-fold increase in sensor response rate through enhanced transport of analyte to the active in-hole sensing surface [95]. In order to quantify and characterize the sieving action (or collection efficiency) of flow-through nanohole arrays, a scaling analysis is presented in this work, followed by simulations. The analysis was separated into two cases. The first one considers only mass transport effects. The second one considers the effects of both mass transport and reaction kinetic effects (i.e. both transport to the active surface and surface chemistry).

For mass transport, a useful comparison case is that of a planar SPR sensor and a nanohole array of equivalent active area, given equivalent flow rate of an analyte solution. The collection efficiency of the channel configuration is a function of Peclet number, based on channel height, H, the average velocity, U_{ch}, and diffusivity, $\mathcal{D}$ as $Pe_{ch} = U_{ch} H / \mathcal{D}$ [39]. A nanohole array with equivalent active sensing area, provided with the same volume flow rate, is the system considered for the flow-through sensing format. The active sensing area of a nanohole array is taken here as the inner hole surface [33], and thus the number of nanoholes required for equivalent area may be determined as a function of geometric parameters. As the Peclet number in each cases provides a measure of collection efficiency, the ratio of Peclet numbers, Pe_{ch} / Pe_{hole}, provides a means of comparison and several insights. The results may be summarized as follows: for the channel-based surface sensor to have comparable transport performance as the nanohole, it must be a sensor on the scale of a single nanohole, i.e. a channel with hydraulic diameter on the order of a single nanohole. Such a sensor would not be practical both because the analyte throughput, equivalent to a single nanohole, would be too low, and it is not possible to interrogate such a small area with traditional SPR. Given the same flow rate and active area, the flow-through nanohole array sensor achieves effectively complete (i.e., > 99 %) collection operating at $Pe_{hole} \sim 1$ or below. A corresponding flow-over system with $Pe_{ch} \sim 10^2$ would collect only ~ 2% of analyte.

For the combined mass transport and binding kinetics case, the computational model, validated by experimental data, provides guidelines for performance as a function of binding time constant, analyte diffusivity, and running parameters. For common binding kinetics and analytes, flow-through nanohole arrays offer ~10-fold improvement in

response time, with a maximum of 20-fold improvement for small biomolecules with rapid kinetics.

Full details on this study are provided in Appendix B or [97].

2.3 Optofluidic concentration: Photonic nanostructure as concentrator and sensor

Biomarkers available for sensing in typical applications are usually present in very low concentrations and are costly [42, 98]. Limited concentrations of analytes, particularly at the limit of sensitivity, reduce the reliability of the measurements. Therefore, it is usually necessary to process samples prior to sensing, to concentrate analytes of interest and remove other components [99].

Several analyte concentration strategies have been reported in the past, including field amplified stacking [40, 45], isotachophoresis [40], electrokinetic trapping[20, 46-48], conductivity gradient focusing [49] and temperature gradient focusing [50]. Electrokinetic trapping has achieved the highest level of analyte enrichment. Due to its inherent flexibility, different approaches have been used with this technique. Concentration polarization, for instance, exploits the ionic permselectivity of nanoporous membranes occurring at microfluidic/nanofluidic interfaces under the influence of applied electric fields [47, 51, 53]. Electric field gradient focusing (EFGF) is another recently reported analyte concentration approach that exploits the formation of a steep field gradient in a microchannel containing a buffer and a floating electrode [48, 54, 55]. Under an applied voltage, the floating electrode acts in bipolar mode, nearly eliminating the electric field in its vicinity, resulting in a non-uniform distribution of ionic species

and, consequently, a non-uniform distribution of the electric field along the microchannel. The electric field gradient, in turn, affects the electrokinetic transport of electrically charged species [48] (e.g. buffer ions, tracers and biomarkers). Specifically, for negatively charged molecules, the increased electric field in the vicinity of the floating electrode results in an increased electrophoretic force that eventually balances the counter-acting forces imposed by the bulk flow. The charged molecules become stationary and are locally enriched at some distance from the floating electrode [54, 56].

Periodic arrays of through nanohole in metal films support enhanced transmission at resonant wavelengths and offer significant reductions in time response when employed as optofluidic sensing elements (as detailed in the previous sections). However, the use of nanohole arrays has been limited to applications that exploit their inherent fluidic or sensing optical characteristics. The present work reports the first experimental demonstration in which a flow-through nanohole array acts as a fluidic conduit, an optical sensor and an active electrode for charged analyte concentration. The metallic layer in a flow-through nanohole array based sensor may operate as a floating electrode when applying an external electric potential to the fluid. The charged analyte components then become enriched by EFGF due to the electric field uniformities induced by the nanohole array. However, in order to operate the sensing platform in dual mode (i.e. for analyte concentration and sensing) the biomarker enriched plug is required to reach the active area of the sensor (i.e. the nanoholes). A pressure driven flow serves to shift the position of the enriched plug of analyte into the holes. The novel technique proposed in this work enables fluorescein enrichment of 180-fold in ~ 1 min. Additionally, 100-fold enrichment and simultaneous SPR sensing of bovine serum albumin (BSA) was achieved. This work

places metallic nanostructures in a new class of actuators possessing exceptional functionality due to the variety of transport mechanisms afforded by their unique structure and material make-up.

Full details on this contribution are provided in Appendix C.

2.4 Integrated Nanohole Array Surface Plasmon Resonance Sensing Device using a Dual-Wavelength Source

Common surface plasmon resonance (SPR) technologies used in biomedical applications rely on coupling techniques such as the Kretschmann, grating and waveguide coupling configurations [32, 100, 101]. Assorted metal nanostructures that support surface plasmon excitations include nanoparticles [102] and nanoholes in metal films [81], the latter of which was found to exhibit extraordinary optical transmission (EOT) [29]. EOT resonances specifically depend on the refractive index near the surface, which has motivated the use of nanohole arrays as biosensors [31]. It was recognized early on that the collinear optical geometry of nanohole arrays is convenient for integration, further offering the potential for a high degree of multiplexing within a microfluidic environment [31].

An alternative to wavelength-shift detection in biosensing applications is to monitor the extent of adsorption by measuring the intensity variations from transmitted monochromatic beams [103]. This has the benefit of simplifying the detection scheme (i.e., removing the need for a spectrometer), but reduces the spectral diversity of the detected signal. Consequently, the changes in light intensity used in this approach are often susceptible to spurious effects, such as drift in the sources or detectors and bulk

matrix scattering as well as absorption [79]. In order to eliminate spurious effects associated with a single source at a particular wavelength, a second source at a different wavelength, responding in the opposite manner to the first source may be added. In particular, if the intensity of the first source decreases to indicate a sensing event, this can be isolated from mere absorption or scattering of the light because the intensity of the second source should increase.

This work was done in collaboration with members of the Electrical Engineering Department. Specifically, the nanohole array fabrication and part of the MATLAB code for signal visualization and acquisition were done by Asif I. K. Choudhury; circuitry design, MATLAB coding and part of the experiments were by John Campbell; implementation and redesign of the circuitry, data analysis, manuscript writing and part of the experiments were done by Serge Vincent; and chemical solution preparation, experimental design, data analysis, microfluidic fabrication and implementation, experimental work was completed by the candidate. The final bulk of the paper was also written by the candidate.

This collaborative effort resulted in a hand-held integrated nanohole array-based sensing device with nine sensor elements, which is applicable to multiplexed detection [104]. The device uses a two-color LED sensing scheme which can be used to distinguish between spurious sensing artefacts and the detection signal, as pairs of optical signals can be expected to exhibit complementary behaviour. The result is a sensing system that would be immune to changes, for instance, in ambient light levels as expected in the field. This implementation is a significant step towards the use of SPR sensing technology for point-of-care and field testing applications. The device is based on

nanohole array sensing, where the transmission spectrum of the nanohole array is modified by the local refractive index close to the metal surface. The device is tested through both bulk refractive index sensing and surface adsorption sensing experiments.

Bulk sensing and dynamic surface binding were demonstrated, with a bulk sensitivity of 266 pixel intensity units/RIU, LOD of $6x10^{-4}$ RIU (with potential for improvement by two orders of magnitude), and sequential binding process response for 2 μM streptavidin to biotin. The integrated nature of this apparatus, as well as its relatively low component cost and potential for multiplexing, make it a promising development for future point-of-care diagnostics and field research. Further optimization, by exploiting the full dynamic range of the sensor, can be expected to enable a three-fold improvement in LOD.

Full details of this contribution are provided in Appendix D.

2.5 Quantitative Real-Time Plasmonic Sensing with an Integrated Microfluidic Concentration Gradient Generator

Detection of low concentrations of biomarkers is essential for early detection of disease [105]. Quantitative monitoring of biomolecular interaction is needed for many diagnosis applications and usually critical for those involving protein interactions for biomarker detection [106-108]. In contrast to a qualitative pass/fail test, quantitative sensing provides the detected concentration of the analytes. Biomarker detection also involves different types of protein interactions, including dynamic binding characteristics of the binding event which can be studied using quantitative sensing platforms [106, 109, 110].

The benefits offered by microfluidic-based diagnostic technologies are well documented [111, 112]. Biomarker quantitation based on calibration curves are

extensively used in traditional analytical chemistry [113-115] and have been incorporated into microfluidic platforms in the past [116-118].

As sensing elements, nanohole arrays are most applicable to the detection of adsorbed species, in analogy with conventional SPR sensing, which has motivated their use in biosensing [84, 119]. Integration of nanohole arrays in microfluidic chips has been recently reported in several studies [15, 85, 106], including articles resulting from this thesis work.

In the present work, quantitative label-free detection of an ovarian cancer biomarker is presented using an array of nanohole arrays integrated with a microfluidic concentration gradient generator. This work was done in collaboration with Jacqueline Ferreira from the department of Chemistry. The approach is to generate, in every test, a calibration curve on-chip, using points of known analyte concentration for the quantification of a sample of unknown concentration. The concentration gradient is achieved by step-wise diffusive mixing of two base streams with known analyte concentration. The quantification of biomarker concentration in the sample stream is achieved by SPR imaging via direct transmission on a CCD. The system was first used to detect and quantify the immobilization of antibody (AB) PAX8, revealing a concentration of 15.6 $\mu g\ mL^{-1}$ agreeing within 5% with the known concentration of the test sample. The biosensor was then used in the detection of ovarian cancer antigen (AG) r-PAX8 using the same sensing scheme. For this test, two concentrations of AG were used. Detection was achieved by SPR imaging and the quantification revealed AG concentrations of 3 and 5 $\mu g\ mL^{-1}$, as compared to the known concentrations of 2 and 7 $\mu g\ mL^{-1}$, respectively. The proposed biosensor demonstrated the ability of self-generating

calibration curves on-chip in an integrated microfluidic-SPR based platform, representing a further step towards the development of comprehensive lab-on-chip biomedical diagnostics.

Full details are provided in Appendix E.

2.6 Microfluidic Liquid Actuation through Ground-Directed Electric Discharge

While the previous contributions in this thesis focus on nanohole arrays in microfluidics and associated transport and instrumentation aspects, this last component of the work addresses fluid actuation and control in the microfluidic layer. Some of the main benefits offered by microfluidic-based systems stem from the ability to integrate complex analytical functions and to multiplex multiple operations. Some of these functions require dynamic liquid control, or liquid actuation, at the scale of individual channels. Methods for controlling liquid flows at the microscale include elastomeric switching valves [120], electrokientic control with on-chip electrodes [121], centrifugal systems [122, 123] and electro-wetting in droplet systems [124, 125]. A commonly used material in microfluidics, poly(dimethylsiloxane) (PDMS), is natively hydrophobic but can be rendered hydrophilic by exposure to oxygen plasma [126]. Typically, this method has been used for bonding layers of PDMS chips by exposure of the bonding surfaces to plasma using vacuum plasma ovens or electric discharges from corona devices [127-130].

Electric discharges have been used in the past for flow control of gases in MEMS devices[131]. The actuation of the gas is achieved by ionization of air which generates in turn a gas flow. This phenomenon is known as ionic wind and the devices are usually

referred to as electrostatic fluid accelerators. However, this type of actuation is exclusive to gases.

Localized treatment of microfluidic structures by electric discharges using corona devices has been achieved in the past [128, 130, 132]. These previous works indicate some potential for microfluidic liquid actuation using this approach. The aim of the present work is to provide a new technique for the real-time actuation and control of microfluidic flows via ground-directed electric discharge. The approach is summarized as follows: when an electric discharge is applied, the air in the microchannel is ionized causing a change in the surface energy; the resulting change in the contact angle induces rapid liquid transport through the channel by capillary action. In contrast to established plasma treatment, this method employs a ground electrode that guides the electric field. This approach enables rapid treatment of select microchannels and thus provides a means of real-time fluid actuation as opposed to simply a pretreatment process. For this work, the technique was demonstrated experimentally using different microchannel geometries under different electric discharge conditions. High-speed visualization analysis of discharge-induced liquid flows in straight microchannels indicated on-demand liquid velocities up to 7 cm/s. Two theoretical models were used to fit the experimental data, finding a best fit at a contact angle of 65°. Fluid flow velocities exhibited a linear dependence on microchannel length. The increase in power setting of the device showed a minimal change in the resulting treatment and flow actuation. Longer lengths could be achieved at higher intensities or longer exposure times. Together these results show that sub-second applications of the electric discharge can actuate fluids over length-scales on the order of ~ 1 cm. The average liquid flow velocities were found to increase linearly

with the power intensity, with average flow velocities on the order of ~ 5cm/s. To demonstrate the potential of this technique for integrated lab-on-a-chip applications, application in a serpentine channel structure, for on-demand fluid routing, to initiate a mixing process, and through an on-chip integrated microelectrode were achieved.

Full details on this contribution are provided in Appendix F or [133].

Chapter 3

Conclusions and Future Work

3.1 Conclusions and Contributions

This dissertation was dedicated to the development of a sensing platform with potential for the early detection of disease. The work resulted in the development of optofluidic sensing platforms, based on nanohole array structures. The development mainly focused on experimentation, but also included theoretical scaling analysis and modeling elements. The contributions of this thesis included design, micro- and nanofabrication, multi-scale component integration, experimental testing and verification, and numerical and analytical analyses. The main contributions of this dissertation are next summarized:

(i) An optofluidic flow-through sensor was developed. Through holes from nanohole array based sensors were used, for the first time, as nanochannels to exploit the benefits of analyte confinement. Nanofabrication of through-holes, as well as simulation and experimental studies on the maximum transmembrane pressures under flow-through operation were performed. All the approaches converged to tolerable pressures of up to 20 psi and maximum membrane deflections of ~ 20 μm. Flow-through sensing was achieved by SPR spectroscopy, and demonstrated six-fold improvement in response time in the detection of monolayer formation, compared to the established flow-over sensing format. Finally, the flow-through optofluidic sensing platform was used

for detecting the step-by-step multilayer assembly of cancer biomarker PAX8 as required for biosensing applications.

(ii) The efficacy and limits for applicability of flow-through nanohole array based sensors were studied through a series of theoretical scaling analyses and numerical simulations. Two scenarios were compared: a flow-over sensor embedded in a microchannel and a flow-through nanohole array with equivalent sensing area, where the nanohole array sensing area was taken as the inner-walls of the nanoholes. The analysis was divided into two parts, the study of the mass transport alone, and the combined influence of the mass transport and the reaction kinetics at the surface. The mass transport analysis demonstrated that given equivalent sensing area and flow rate the flow-through nanohole format enables significantly increased flux of analytes to the sensing surface. For the specific case of a 10 nL/min flow rate provided to the system, the analysis revealed a 40-fold enhancement in transport of analyte to the surface. The computational analysis combining mass transport and reaction kinetics, validated by experimental data, provided guidelines for the sensor performance as a function of binding time constant, analyte diffusivity, and running parameters. For common binding kinetics and analytes, flow-through nanohole arrays were found to offer ~10-fold improvement in response time, with a maximum of 20-fold improvement for small biomolecules with rapid kinetics.

(iii) Flow-through nanohole arrays were used as both active electrodes in the fluid and as plasmonic sensor. Previous demonstrations using nanohole array based sensing exploited only the intrinsic optical characteristics of the nanostructures.

Under an applied electric potential, the metallic layer of the nanohole arrays can also act as a floating electrode, almost eliminating the applied electric field in its vicinity. This effect results in a non-uniform distribution of ionic species and, consequently, a non-uniform distribution of the electric field in the surrounding microchannel environment. The electric field gradient affects the electrokinetic transport of electrically charged species. For charged molecules, the increased electric field in the vicinity of the floating electrode results in an increased electrophoretic force that eventually balances the counter-acting forces imposed by the bulk flow at some position along the microchannel. The charged molecules then become stationary and are locally enriched. This approach, in combination with a pressure bias, was used for analyte enrichment and subsequent transport into the nanohole arrays for further sensing. A 180-fold enrichment of fluorescein was achieved in 60 s, applying 50 V and ~ 4 kPa. The approach was also used for the concentration and simultaneous sensing of bovine serum albumin (BSA) via SPR spectroscopy, resulting in 100-fold enrichment of the protein. This work represented the first active utilization of metallic nanohole arrays as an electrode and the first demonstration of a photonic nanostructure achieving both local concentration and sensing of analyte.

(iv) A microfluidic, hand-held, nanohole array-based SPR sensing device with a dual-wavelength light source was presented. The system included nine nanohole arrays as sensors milled on Au-on-glass substrate, embedded into a microfluidic chip assembly as well as readily available commercial

components: an LED light source, driving circuitry, a CCD detector and a computer interface. The dual-wavelength light source was used to increase the spectral diversity of the device, isolating possible parameter variations from the components. The prototype showed bulk sensitivity of 266 pixel intensity units per refractive index unit (RIU) and a limit of detection of 6×10^{-4} RIU. In order to demonstrate the functionality of the system as a surface based sensing system, the sequential binding of a streptavidin-biotin system was demonstrated. Even though nanohole arrays have been applied in many research studies , and their suitability to device integration is well recognized, this work represented the first demonstration of a fully-integrated nanohole array based sensing device.

(v) A nanohole array based sensor was integrated with a microfluidic concentration gradient generator for the detection and quantification of ovarian cancer antibody and antigen. The approach was to generate, in every test, a calibration curve on-chip, using points of known analyte concentration for the quantification of a sample of unknown concentration flowing in parallel. The concentration gradient was achieved by stepped diffusive mixing of two base streams with known analyte concentration. The chip generated six concentration streams which were directed into separate outlet microchannels. The quantification of biomarker concentration in the sample stream was achieved by SPR imaging via direct transmission on a CCD. The intensity variations related to analyte concentration were tracked over time and the determination of sample analyte concentration was achieved by comparison

with the standard curve. The biosensor was first used to detect and quantify the immobilization of antibody PAX8, resulting in a concentration of 15.6 μg/mL, agreeing within 5% with the known concentration of the sample. The biosensor was then used in the detection of ovarian cancer AG r-PAX8 using the same sensing scheme. For this test, two concentrations of AG were used. Detection was achieved by SPR imaging and the quantification revealed AG concentrations of 3 and 5 μg mL^{-1}, as compared to the known concentrations of 2 and 7 μg mL^{-1}, respectively.

(vi) The last contribution in this thesis focused on liquid actuation in the microfluidic layer. A novel microfluidic technique to actuate liquids in microchannels using a ground-directed electric discharge was demonstrated. The technique is based in the wetting conditions changes at the liquid solid interface induced by electric discharges when using polymeric, natively hydrophobic microfluidic chips. This work demonstrated that ground-directed electric discharge enables rapid surface treatment of select microchannels that rendered the surface of the microchannel hydrophilic and provided a means of real-time fluid actuation. The method was characterized through one- and two-dimensional channel flow experiments, and comparison with mathematical models. Instantaneous fluid velocities fit theoretical models at a contact angle of ~ 65°, with average fluid velocities on the order of 5 cm/s. To demonstrate the applicability of this technique to integrated lab-on-chip systems, selective liquid routing and the actuation of a mixing process were demonstrated, as well as the application of the technique using an integrated microelectrode. In

contrast to previous pretreatment methods using electric discharge, this technique enables the direct control, routing and actuation of microfluidic flows in real time.

3.2 Future Work

The potential future work to follow this dissertation may include: the investigation and selection of new substrates for through-hole nanohole array fabrication with improved mechanical properties; the detailed study of the mechanical performance of the nanohole array substrates, including stress, strain and deflection analysis; the detailed study and application of nanostructure shape distortion due to substrate deflection under flow-through operation and its influence on optical response; development of multiplexed versions of the optofluidic sensing platform; further theoretical and experimental studies of electrokinetic phenomena for analyte concentration; system testing in bioassays with clinical samples; and the incorporation of the optofluidic sensor into an lab-on-chip platform with added integrated functions, such as sample filtering preparation.

Specific details on future work suggested for each contribution in this dissertation are provided below:

(i) An array of nanohole arrays integrated with a microfluidic system, functionalized with different types of biomolecules (e.g. antibodies) for the multiplexed detection of several types of analyte in one single test. This may include testing of different antigen-antibody systems as well as other biological species, such as viruses. Also, exploration of new techniques for nanohole array

fabrication is important, towards the development of a more cost-effective and mass-produced system.

(ii) A three-dimensional model accounting for mass transport effects in the space surrounding the nanohole arrays prior to surface binding, and the extended study of the influence of the reaction kinetics of additional antigen-antibody systems.

(iii) Further experimentation, involving a wider range of applied voltages for the concentration of charged species, and different molecules and buffer systems for an in-depth characterization of the electrohydrodynamic concentration phenomenon demonstrated here. Additional development and redesign of several components may lead to a system with reduced footprint and higher concentration efficiency. Most notably, the electrodes may be directly printed in the microfluidic structure; the metallic nanohole array layer could be coated with an additional Pt layer to reduce the risk of hydrolysis; the whole system may integrated over a customized Si-wafer base containing numerous nanohole arrays, which may result in a significant decrease in the overall size of the optofluidic system; and an optical fibre could be integrated into the microfluidic layer for integrated signal detection.

(iv) Incorporation of a thermal control scheme to improve the performance of the system. Signal drift can be an issue for some applications and should be isolated, analyzed and corrected. Additional improvements may include an

improved MATLAB code for pixel acquisition and analysis and additional experiments involving biological species.

(v) Double blinded experiments with several types of biomolecules to extend the characterization of the system. This would require the detailed design of the microfluidic chip, accounting for the diffusivity of the specific analyte in order to correctly generate the required concentration gradient and resulting calibration curves.

(vi) To further increase the characterization of the electric discharge based fluid actuation technique a detailed study of the influence of the power intensity of the electric discharge is required. This characterization may also include computational simulations and theoretical models. Specifically, theoretical studies could result in a modified version of the Young-Laplace equation accounting for the surface energy change at the liquid-solid interface due to the electric discharge treatment, such as the Young-Lippmann equation used to describe electrowetting phenomena. Additionally, the technique could be used in programmable fluidic functions using integrated microelectrodes and means for the controlled application of electric discharges.

Bibliography

1. Chin, C.D., V. Linder, and S.K. Sia, *Lab-on-a-chip devices for global health: Past studies and future opportunities.* Lab on a Chip, 2007. **7**(1): p. 41-57.
2. Yager, P., et al., *Microfluidic diagnostic technologies for global public health.* Nature, 2006. **442**(7101): p. 412-418.
3. Lopez, A., C. Mathers, and M. Ezzati, *Global Burden of Disease and Risk Factors*. 2006: Oxford University Press and the World Bank.
4. Myszka, D.G., et al., *Extending the Range of Rate Constants Available from BIACORE: Interpreting Mass Transport-Influenced Binding Data.* Biophys. J., 1998. **75**(2): p. 583-594.
5. Homola, J., S.S. Yee, and G. Gauglitz, *Surface plasmon resonance sensors: Review.* Sens. Actuat. B, 1999. **54**: p. 3-15.
6. Natarajan, S., et al., *Continuous-flow microfluidic printing of proteins for array-based applications including surface plasmon resonance imaging.* Analytical Biochemistry, 2008. **373**(1): p. 141-146.
7. Erickson, D., et al., *Nanobiosensors: optofluidic, electrical and mechanical approaches to biomolecular detection at the nanoscale.* Microfluidics and Nanofluidics, 2008. **4**: p. 33-52.
8. Lebedev, K., S. Mafé, and P. Stroeve, *Convection, diffusion and reaction in a surface-based biosensor: Modeling of cooperativity and binding site competition on the surface and in the hydrogel.* Journal of Colloid and Interface Science, 2006. **296**(2): p. 527-537.
9. Gold, V., et al., *COMPENDIUM OF CHEMICAL TERMINOLOGY IUPAC INTERNATIONAL UNION OF PURE AND APPLIED CHEMISTRY RECOMMENDATIONS*. Gold, V., K. L. Loening, A. D. Mcnaught and P. Sehmi. Compendium of Chemical Terminology: Iupac. 1987.
10. Haeberle, S. and R. Zengerle, *Microfluidic platforms for lab-on-a-chip applications.* Lab on a Chip, 2007. **7**(9): p. 1094-1110.
11. Brody, J., et al., *Biotechnology at low Reynolds numbers.* Biophys. J., 1996. **71**: p. 3430.
12. Manz, A., N. Graber, and H.M. Widmer, *Miniaturized total chemical analysis systems: A novel concept for chemical sensing.* Sensors and Actuators B: Chemical, 1990. **1**(1): p. 244-248.
13. Beebe, D.J., G.A. Mensing, and G.M. Walker, *PHYSICS AND APPLICATIONS OF MICROFLUIDICS IN BIOLOGY.* Annual Review of Biomedical Engineering, 2002. **4**(1): p. 261-286.
14. Sia, S.K. and L.J. Kricka, *Microfluidics and point-of-care testing.* Lab on a Chip, 2008. **8**(12): p. 1982-1983.
15. Hwang, G.M., et al., *Plasmonic Sensing of Biological Analytes Through Nanoholes.* Ieee Sensors Journal, 2008. **8**(11-12): p. 2074-2079.
16. Yanik, A.A., et al., *An Optofluidic Nanoplasmonic Biosensor for Direct Detection of Live Viruses from Biological Media.* Nano Letters, 2010. **10**(12): p. 4962-4969.
17. Andersson, P., et al., *Parallel nanoliter microfluidic analysis system.* Analytical Chemistry, 2007. **79**(11): p. 4022-4030.

18. Garcia, A.L., et al., *Electrokinetic molecular separation in nanoscale fluidic channels.* Lab on a Chip, 2005. **5**(11): p. 1271-1276.
19. Sheehan, P.E. and L.J. Whitman, *Detection limits for nanoscale biosensors.* Nano Letters, 2005. **5**(4): p. 803-807.
20. Wang, Y.C., A.L. Stevens, and J.Y. Han, *Million-fold preconcentration of proteins and peptides by nanofluidic filter.* Anal. Chem., 2005. **77**(14): p. 4293-4299.
21. Psaltis, D., S.R. Quake, and C. Yang, *Developing optofluidic technology through the fusion of microfluidics and optics.* Nature, 2006. **442**: p. 381-386.
22. Erickson, D., *Special issue on "Optofluidics".* Microfluidics and Nanofluidics, 2008. **4**(1): p. 1-2.
23. Schmidt, H. and A.R. Hawkins, *Optofluidic waveguides: I. Concepts and implementations.* Microfluidics and Nanofluidics, 2008. **4**(1-2): p. 3-16.
24. Hawkins, A.R. and H. Schmidt, *Optofluidic waveguides: II. Fabrication and structures.* Microfluidics and Nanofluidics, 2008. **4**: p. 17-32.
25. Yin, D.L., et al., *Planar optofluidic chip for single particle detection, manipulation, and analysis.* Lab on a Chip, 2007. **7**(9): p. 1171-1175.
26. Blakely, J.T., et al., *Fully-integrated optofluidic trap with linear microsphere array.* 2007 Ieee/Leos International Conference on Optical Mems and Nanophotonics, 2007: p. 67-68.
27. Lin, F.Y.H., et al., *Development of a novel microfluidic immunoassay for the detection of Helicobacter pylori infection.* The Analyst, 2004. **129**(9): p. 823-828.
28. Erickson, D., et al., *Nanobiosensors: optofluidic, electrical and mechanical approaches to biomolecular detection at the nanoscale.* Microfluidics and Nanofluidics, 2007.
29. Ebbesen, T.W., et al., *Extraordinary optical transmission through sub-wavelength hole arrays.* Nature, 1998. **391**(6668): p. 667-669.
30. Genet, C. and T.W. Ebbesen, *Light in tiny holes.* Nature, 2007. **445**(7123): p. 39-46.
31. Brolo, A.G., et al., *Surface plasmon sensor based on the enhanced light transmission through arrays of nanoholes in gold films.* Langmuir, 2004. **20**(12): p. 4813-4815.
32. Homola, J., *Surface plasmon resonance sensors for detection of chemical and biological species.* Chemical Reviews, 2008. **108**(2): p. 462-493.
33. Ferreira, J., et al., *Attomolar Protein Detection Using in-Hole Surface Plasmon Resonance.* J. Am. Chem. Soc., 2009. **131**(2): p. 436-437.
34. Huang, X.J. and Y.K. Choi, *Chemical sensors based on nanostructured materials.* Sensors and Actuators B-Chemical, 2007. **122**(2): p. 659-671.
35. Kim, D.R. and X.L. Zheng, *Numerical Characterization and Optimization of the Microfluidics for Nanowire Biosensors.* Nano Letters, 2008. **8**(10): p. 3233-3237.
36. Zimmermann, M., et al., *Modeling and Optimization of High-Sensitivity, Low-Volume Microfluidic-Based Surface Immunoassays.* Biomedical Microdevices, 2005. **7**(2): p. 99-110.
37. Hu, G., Y. Gao, and D. Li, *Modeling micropatterned antigen-antibody binding kinetics in a microfluidic chip.* Biosensors and Bioelectronics, 2007. **22**(7): p. 1403-1409.

38. Fu, E., et al., *Modeling of a Competitive Microfluidic Heterogeneous Immunoassay: Sensitivity of the Assay Response to Varying System Parameters.* Analytical Chemistry, 2009. **81**(9): p. 3407-3413.
39. Squires, T.M., R.J. Messinger, and S.R. Manalis, *Making it stick: convection, reaction and diffusion in surface-based biosensors.* Nature Biotech., 2008. **26**(4): p. 417-426.
40. Jung, B., R. Bharadwaj, and J.G. Santiago, *On-chip millionfold sample stacking using transient isotachophoresis.* Anal. Chem., 2006. **78**(7): p. 2319-2327.
41. Scarff, B., C. Escobedo, and D. Sinton, *Radial sample preconcentration.* Lab Chip, 2011. **11**(6): p. 1102-1109.
42. Astorga-Wells, J. and H. Swerdlow, *Fluidic preconcentrator device for capillary electrophoresis of proteins.* Analytical Chemistry, 2003. **75**(19): p. 5207-5212.
43. Hortin, G.L. and D. Sviridov, *The dynamic range problem in the analysis of the plasma proteome.* Journal of Proteomics, 2010. **73**(3, Sp. Iss. SI): p. 629-636.
44. Freire, S.L.S. and A.R. Wheeler, *Proteome-on-a-chip: Mirage, or on the horizon?* Lab on a Chip, 2006. **6**(11): p. 1415-1423.
45. Sustarich, J.M., B.D. Storey, and S. Pennathur, *Field-amplified sample stacking and focusing in nanofluidic channels.* Phys. Fluids, 2010. **22**(11).
46. Wang, Y.C. and J.Y. Han, *Pre-binding dynamic range and sensitivity enhancement for immuno-sensors using nanofluidic preconcentrator.* Lab Chip, 2008. **8**(3): p. 392-394.
47. Kim, S.J. and J.Y. Han, *Self-sealed vertical polymeric nanoporous-junctions for high-throughput nanofluidic applications.* Anal. Chem., 2008. **80**(9): p. 3507-3511.
48. Hlushkou, D., et al., *Electric field gradient focusing in microchannels with embedded bipolar electrode.* Lab Chip, 2009. **9**(13): p. 1903-1913.
49. Shackman, J.G. and D. Ross, *Counter-flow gradient electrofocusing.* Electrophoresis, 2007. **28**(4): p. 556-571.
50. Ross, D. and L.E. Locascio, *Microfluidic temperature gradient focusing.* Anal. Chem., 2002. **74**(11): p. 2556-2564.
51. Scarff, B., C. Escobedo, and D. Sinton, *Radial sample preconcentration.* Lab Chip, 2011.
52. Schoch, R.B., J.Y. Han, and P. Renaud, *Transport phenomena in nanofluidics.* Reviews of Modern Physics, 2008. **80**(3): p. 839-883.
53. Plecis, A., et al., *Electropreconcentration with Charge-Selective Nanochannels.* Analytical Chemistry, 2008. **80**(24): p. 9542-9550.
54. Dhopeshwarkar, R., et al., *Electrokinetics in microfluidic channels containing a floating electrode.* J. Am. Chem. Soc., 2008. **130**(32): p. 10480-+.
55. Piruska, A., et al., *Electrokinetically driven fluidic transport in integrated three-dimensional microfluidic devices incorporating gold-coated nanocapillary array membranes.* Lab Chip, 2008. **8**(10): p. 1625-1631.
56. Plecis, A., A. Pallandre, and A.-M. Haghiri-Gosnet, *Ionic and mass transport in micro-nanofluidic devices: a matter of volumic surface charge.* Lab on a Chip, 2011. **11**(5): p. 795-804.
57. Probstein, R.F., *Physicochemical Hydrodynamics*. Second ed. 2003, New Jersey: John Wiley & Sons Inc.

58. White, F.M., *Fluid Mechanics*. Fifth Edition ed. 2003, New York: McGraw-Hill.
59. Squires, T.M. and S.R. Quake, *Microfluidics: Fluid physics at the nanoliter scale.* Reviews of Modern Physics, 2005. **77**(3): p. 977-1026.
60. Sampson, R.A., *On Stokes's Current Function.* Philosophical Transactions of the Royal Society of London. (A.), 1891. **182**: p. 449-518.
61. Dagan, Z., S. Weinbaum, and R. Pfeffer, *THEORY AND EXPERIMENT ON THE 3-DIMENSIONAL MOTION OF A FREELY SUSPENDED SPHERICAL-PARTICLE AT THE ENTRANCE TO A PORE AT LOW REYNOLDS-NUMBER.* Chemical Engineering Science, 1983. **38**(4): p. 583-596.
62. Tong, H.D., et al., *Silicon Nitride Nanosieve Membrane.* Nano Lett., 2004. **4**(2): p. 283-287.
63. van Rijn, C., et al., *Deflection and maximum load of microfiltration membrane sieves made with silicon micromachining.* Microelectromechanical Systems, Journal of, 1997. **6**(1): p. 48-54.
64. Pennathur, S. and J.G. Santiago, *Electrokinetic transport in nanochannels. 1. Theory.* Analytical Chemistry, 2005. **77**(21): p. 6772-6781.
65. Washburn, E.W., *The Dynamics of Capillary Flow.* Physical Review, 1921. **17**(3): p. 273.
66. Hilpert, M., *Effects of dynamic contact angle on liquid infiltration into horizontal capillary tubes: (Semi)-analytical solutions.* Journal of Colloid and Interface Science, 2009. **337**(1): p. 131-137.
67. Ramsey, J.D., et al., *High-Efficiency, Two-Dimensional Separations of Protein Digests on Microfluidic Devices.* Analytical Chemistry, 2003. **75**(15): p. 3758-3764.
68. Samuel K. Sia, G.M.W., *Microfluidic devices fabricated in Poly(dimethylsiloxane) for biological studies.* Electrophoresis, 2003. **24**(21): p. 3563-3576.
69. Lazar, I.M. and B.L. Karger, *Multiple Open-Channel Electroosmotic Pumping System for Microfluidic Sample Handling.* Analytical Chemistry, 2002. **74**(24): p. 6259-6268.
70. Wang, X.Y., et al., *Electroosmotic pumps and their applications in microfluidic systems.* Microfluidics and Nanofluidics, 2009. **6**(2): p. 145-162.
71. Seibel, K., et al., *A programmable planar electroosmotic micropump for lab-on-a-chip applications.* Journal of Micromechanics and Microengineering, 2008. **18**(2).
72. Ma, J.P., L.X. Chen, and Y.F. Guan, *Research on electrokinetic pump techniques.* Progress in Chemistry, 2007. **19**(11): p. 1826-1831.
73. Reuss, F.F., *Charge-induced flow.* Proceedings of the Imperial Society of Naturalists of Moscow, 1809. **3**: p. 327-344.
74. Squires, T.M., *Induced-charge electrokinetics: fundamental challenges and opportunities.* Lab on a Chip, 2009. **9**(17): p. 2477-2483.
75. Bazant, M.Z. and T.M. Squires, *Induced-charge electrokinetic phenomena: Theory and microfluidic applications.* Phys. Rev. Lett., 2004. **92**(6).
76. Squires, T.M. and M.Z. Bazant, *Induced-charge electro-osmosis.* Journal of Fluid Mechanics, 2004. **509**: p. 217-252.

77. Bazant, M.Z. and T.M. Squires, *Induced-charge electrokinetic phenomena.* Current Opinion in Colloid & Interface Science, 2010. **15**(3): p. 203-213.
78. Simonov, I.N. and V.N. Shilov, *Theory of low frequency dielectric-dispersion of a suspension of ideally polarizable spherical-particles.* Colloid Journal of the USSR, 1977. **39**(5): p. 775-780.
79. Gordon, R., et al., *Resonant optical transmission through hole-arrays in metal films: physics and applications.* Laser & Photonics Reviews, 2010. **4**(2): p. 311-335.
80. Roh, S., T. Chung, and B. Lee, *Overview of the Characteristics of Micro- and Nano-Structured Surface Plasmon Resonance Sensors.* Sensors, 2011. **11**(2): p. 1565-1588.
81. Gordon, R., et al., *A New Generation of Sensors Based on Extraordinary Optical Transmission.* Accounts of Chemical Research, 2008. **41**(8): p. 1049-1057.
82. Rodriguez-Fortuno, F.J., et al., *Highly-sensitive chemical detection in the infrared regime using plasmonic gold nanocrosses.* Applied Physics Letters, 2011. **98**(13).
83. Im, H., et al., *Plasmonic Nanoholes in a Multichannel Microarray Format for Parallel Kinetic Assays and Differential Sensing.* Analytical Chemistry, 2009. **81**(8): p. 2854-2859.
84. Sharpe, J.C., et al., *Gold nanohole array substrates as immunobiosensors.* Analytical Chemistry, 2008. **80**(6): p. 2244-2249.
85. Lindquist, N.C., et al., *Sub-micron resolution surface plasmon resonance imaging enabled by nanohole arrays with surrounding Bragg mirrors for enhanced sensitivity and isolation.* Lab on a Chip, 2009. **9**(3): p. 382-387.
86. Lesuffleur, A., et al., *Periodic nanohole arrays with shape-enhanced plasmon resonance as real-time biosensors.* Applied Physics Letters, 2007. **90**(24).
87. Gao, D., et al., *Detection of tumor markers based on extinction spectra of visible light passing through gold nanoholes.* Applied Physics Letters, 2007. **90**(7).
88. DeLeebeeck, A., et al., *On-Chip Surface-Based Detection with Nanohole Arrays.* Anal. Chem., 2007. **79**(11): p. 4094-4100.
89. Giannuzzi, L.A. and F.A. Stevie, *Introduction to Focused Ion Beams: Instrumentation, Theory, Techniques and Practice*. 2005, New York: Springer.
90. Duffy, D., et al., *Rapid prototyping of microfluidic systems in poly (dimethyl siloxane).* Anal. Chem., 1998. **70**: p. 4974.
91. McDonald, J., et al., *Fabrication of microfluidic systems in poly(dimethylsiloxane).* Electrophoresis, 2000. **21**: p. 27.
92. Guilbault, G.G., *Practical Fluorescence: Second Edition*, ed. M. Dekker. 1990, L.A.: New Orleans.
93. Sinton, D., *Microscale flow visualization.* Microfluidics and Nanofluidics, 2004. **1**(1): p. 2-21.
94. Yang, J.F., et al., *Microstructure and mechanical properties of silicon nitride ceramics with controlled porosity.* Journal of the American Ceramic Society, 2002. **85**(6): p. 1512-1516.
95. Eftekhari, F., et al., *Nanoholes As Nanochannels: Flow-through Plasmonic Sensing.* Anal. Chem., 2009. **81**(11): p. 4308-4311.
96. Peterlinz, K.A. and R. Georgiadis, *In situ kinetics of self-assembly by surface plasmon resonance spectroscopy.* Langmuir, 1996. **12**(20): p. 4731-4740.

97. Escobedo, C., et al., *Flow-Through vs Flow-Over: Analysis of Transport and Binding in Nanohole Array Plasmonic Biosensors.* Analytical Chemistry, 2010. **82**(24): p. 10015-10020.
98. Kim, S.J., et al., *Concentration polarization and nonlinear electrokinetic flow near a nanofluidic channel.* Physical Review Letters, 2007. **99**(4): p. 4.
99. Toner, M. and D. Irimia, *BLOOD-ON-A-CHIP.* Annual Review of Biomedical Engineering, 2005. **7**(1): p. 77-103.
100. Kretschmann, E. and H. Raether, *RADIATIVE DECAY OF NON RADIATIVE SURFACE PLASMONS EXCITED BY LIGHT.* Zeitschrift Fur Naturforschung Part a-Astrophysik Physik Und Physikalische Chemie, 1968. **A 23**(12): p. 2135-&.
101. Byun, K.M., *Development of Nanostructured Plasmonic Substrates for Enhanced Optical Biosensing.* Journal of the Optical Society of Korea, 2010. **14**(2): p. 65-76.
102. Liu, G.L., et al., *Optofluidic control using photothermal nanoparticles.* Nature Mater., 2006. **5**: p. 27-32.
103. Lesuffleur, A., et al., *Laser-illuminated nanohole arrays for multiplex plasmonic microarray sensing.* Optics Express, 2008. **16**(1): p. 219-224.
104. Lindquist, N.C., et al., *Sub-micron resolution surface plasmon resonance imaging enabled by nanohole arrays with surrounding Bragg mirrors for enhanced sensitivity and isolation.* Lab on a Chip, 2009. **9**(3): p. 382-387.
105. Xiao, Y. and X. Gao, *Use of IgY antibodies and semiconductor nanocrystal detection in cancer biomarker quantitation.* Biomarkers in Medicine, 2010. **4**(2): p. 227-239.
106. Ji, J., et al., *High-throughput nanohole array based system to monitor multiple binding events in real time.* Analytical Chemistry, 2008. **80**(7): p. 2491-2498.
107. Rao, J., et al., *Using Surface Plasmon Resonance to Study the Binding of Vancomycin and Its Dimer to Self-Assembled Monolayers Presenting d-Ala-d-Ala.* Journal of the American Chemical Society, 1999. **121**(11): p. 2629-2630.
108. Lin, L., et al., *Surface Plasmon Resonance-based Sensors To Identify cis-Regulatory Elements.* Analytical Chemistry, 2004. **76**(22): p. 6555-6559.
109. Hellstrom, I., et al., *The HE4 (WFDC2) Protein Is a Biomarker for Ovarian Carcinoma.* Cancer Res, 2003. **63**(13): p. 3695-3700.
110. Rifai, N. and P.M. Ridker, *High-Sensitivity C-Reactive Protein: A Novel and Promising Marker of Coronary Heart Disease.* Clin Chem, 2001. **47**(3): p. 403-411.
111. Whitesides, G.M., *The origins and the future of microfluidics.* Nature, 2006. **442**(7101): p. 368-373.
112. Fujii, T., *PDMS-based microfluidic devices for biomedical applications.* Microelectronic Engineering, 2002. **61-62**: p. 907-914.
113. Yacoub-George, E., et al., *Automated 10-channel capillary chip immunodetector for biological agents detection.* Biosensors and Bioelectronics, 2007. **22**(7): p. 1368-1375.
114. Huizing, M., et al., *Pharmacokinetics of paclitaxel and metabolites in a randomized comparative study in platinum-pretreated ovarian cancer patients.* Journal of Clinical Oncology, 1993. **11**(11): p. 2127-2135.

115. Kyriakopoulou, L.G., et al., *Prognostic value of quantitatively assessed KLK7 expression in ovarian cancer.* Clinical Biochemistry, 2003. **36**(2): p. 135-143.
116. Yang, W., et al., *Integrated Microfluidic Device for Serum Biomarker Quantitation Using Either Standard Addition or a Calibration Curve.* Analytical Chemistry, 2009. **81**(19): p. 8230-8235.
117. Fan, R., et al., *Integrated barcode chips for rapid, multiplexed analysis of proteins in microliter quantities of blood.* Nature Biotechnology, 2008. **26**(12): p. 1373-1378.
118. Herr, A.E., et al., *Microfluidic immunoassays as rapid saliva-based clinical diagnostics.* Proceedings of the National Academy of Sciences of the United States of America, 2007. **104**(13): p. 5268-5273.
119. Brolo, A.G., et al. *Development of plasmonic substrates for biosensing*. in *Biosensing*. 2008. San Diego, CA, USA: SPIE.
120. Unger, M.A., et al., *Monolithic microfabricated valves and pumps by multilayer soft lithography.* Science, 2000. **288**: p. 113-116.
121. Horiuchi, K. and P. Dutta, *Electrokinetic flow control in microfluidic chips using a field-effect transistor.* Lab on a Chip, 2006. **6**(6): p. 714-723.
122. Kim, J., et al., *Passive flow switching valves on a centrifugal microfluidic platform.* Sensors and Actuators B-Chemical, 2008. **128**(2): p. 613-621.
123. Juncker, D., et al., *Autonomous microfluidic capillary system.* Analytical Chemistry, 2002. **74**(24): p. 6139-6144.
124. Luk, V.N. and A.R. Wheeler, *A Digital Microfluidic Approach to Proteomic Sample Processing.* Analytical Chemistry, 2009. **81**(11): p. 4524-4530.
125. Fair, R.B., *Digital microfluidics: is a true lab-on-a-chip possible?* Microfluidics and Nanofluidics, 2007. **3**(3): p. 245-281.
126. Makamba, H., et al., *Surface modification of poly(dimethylsiloxane) microchannels.* Electrophoresis, 2003. **24**(21): p. 3607-3619.
127. Sun, C., D. Zhang, and L.C. Wadsworth, *Corona treatment of polyolefin films - A review.* Advances in Polymer Technology, 1999. **18**(2): p. 171-180.
128. Zenkiewicz, M., *Oxidation of the filled-polyolefin-film surface layer by corona treatment.* Przemysl Chemiczny, 2005. **84**(10): p. 733-739.
129. Haubert, K., T. Drier, and D. Beebe, *PDMS bonding by means of a portable, low-cost corona system.* Lab on a Chip, 2006. **6**(12): p. 1548-1549.
130. Thorslund, S. and F. Nikolajeff, *Instant oxidation of closed microchannels.* Journal of Micromechanics and Microengineering, 2007. **17**(4): p. N16-N21.
131. Hsu, C.P., et al., *Miniaturization of electrostatic fluid accelerators.* Journal of Microelectromechanical Systems, 2007. **16**(4): p. 809-815.
132. Evju, J.K., et al., *Atmospheric pressure microplasmas for modifying sealed microfluidic devices.* Applied Physics Letters, 2004. **84**(10): p. 1668-1670.
133. Escobedo, C. and D. Sinton, *Microfluidic liquid actuation through ground-directed electric discharge.* Microfluidics and Nanofluidics, 2011: p. 1-10.

Appendix A

Nanoholes as Nanochannels: Flow-through Plasmonic Sensing

Anal. Chem. **2009,** *81,* 4308–4311

Nanoholes As Nanochannels: Flow-through Plasmonic Sensing

Fatemeh Eftekhari,[†] Carlos Escobedo,[‡] Jacqueline Ferreira,[§,||] Xiaobo Duan,[⊥] Emerson M. Girotto,[||] Alexandre G. Brolo,[*,§] Reuven Gordon,[*,†] and David Sinton[*,‡]

Electrical and Computer Engineering, Mechanical Engineering, and Chemistry, University of Victoria, Victoria, British Columbia, Canada, Universidade Estadual de Maringa, Maringa, PR, Brazil, and British Columbia Cancer Agency, Trev & Joyce Deeley Research Centre, Victoria, British Columbia, Canada

We combine nanofluidics and nanoplasmonics for surface-plasmon resonance (SPR) sensing using flow-through nanohole arrays. The role of surface plasmons on resonant transmission motivates the application of nanohole arrays as surface-based biosensors. Research to date, however, has focused on dead-ended holes, and therefore failed to harness the benefits of nanoconfined transport combined with SPR sensing. The flow-through format enables rapid transport of reactants to the active surface inside the nanoholes, with potential for significantly improved time of analysis and biomarker yield through nanohole sieving. We apply the flow-through method to monitor the formation of a monolayer and the immobilization of an ovarian cancer biomarker specific antibody on the sensing surface in real-time. The flow-through method resulted in a 6-fold improvement in response time as compared to the established flow-over method.

Ordered arrays of nanoscale holes in metal films exhibit unique optical transmission characteristics at resonant wavelengths.[1,2] The role of surface plasmon resonance (SPR) on resonant transmission through nanohole arrays has motivated their application as surface-based biosensors.[3] As compared to common SPR sensing, nanohole arrays present many advantages, including a smaller foot-print, lower limits of detection, denser integration, multiplexing, and collinear optical detection.[4−8] These characteristics of nanohole array-based sensors make them particularly well-suited to planar integration with microfluidics in an on-chip format.

Integration of nanohole arrays in microfluidic platforms has evolved rapidly from single-array, single-channel arrangements that facilitate fluid delivery and optical access, to multiplexed arrays of nanohole arrays and service fluidics. A detailed review of recent progress in this area is available elsewhere.[5] The density to which individual nanohole array sensors may be integrated in plane is highlighted in a recent report of 10^7 sensors per square centimeter.[9] There have also been many developments in the supporting instrumentation and device-level integration of nanohole array based sensors.[10] Most notably, for large scale sensor arrays it is more efficient to monitor transmission intensity changes at a set input wavelength[4,6,8] as opposed to detecting peak shifts in broadband transmission spectra. Transmission intensity measurements may be made using commercial cameras or other detector arrays in parallel and real-time.[8] In all of the developments to date, the nanohole array has been employed in a flow-over format,[5] and thus from a transport perspective these nanostructured sensors showed no inherent advantages over microsized surface based sensor technologies.

As a chemical and biological sensor technology, the sensitivity and limit of detection of nanohole array sensors are of central importance. With improved external optics, the sensitivity of nanohole arrays has been demonstrated to be similar to traditional Kreschmann configuration SPR.[11] With respect to limit of detection, we recently compared the sensitivity of a typical nanohole array to that of an otherwise similar array with a silicon oxide layer blocking access to the top surface. The sensitivities of both devices were comparable; however, the in-hole sensing enabled a 5-fold reduction in the sensing area and the detection of proteins in the attomole range.[12] With the benefits of exclusive in-hole sensing established, effective transport of analytes to the in-hole surface presents an opportunity to harness the rapid cross-stream diffusion characteristic of nanofluidic transport. Research to date involving nanohole arrays has focused on dead-ended holes, and therefore failed to harness the potential benefits from rapid

* To whom correspondence should be addressed. E-mail: agbrolo@uvic.ca (A.G.B.), rgordon@uvic.ca (R.G.), dsinton@uvic.ca (D.S.).
† Electrical and Computer Engineering, University of Victoria.
‡ Mechanical Engineering, University of Victoria.
§ Chemistry, University of Victoria.
|| Universidade Estadual de Maringa.
⊥ Trev & Joyce Deeley Research Centre.

(1) Ebbesen, T. W.; Lezec, H. J.; Ghaemi, H. F.; Thio, T.; Wolff, P. A. *Nature* **1998**, *391*, 667–669.
(2) Genet, C.; Ebbesen, T. W. *Nature* **2007**, *445*, 39–46.
(3) Brolo, A. G.; Gordon, R.; Leathem, B.; Kavanagh, K. L. *Langmuir* **2004**, *20*, 4813–4815.
(4) Yang, J. C.; Ji, J.; Hogle, J. M.; Larson, D. N. *Nano Lett* **2008**, *8*, 2718–2724.
(5) Gordon, R.; Sinton, D.; Kavanagh, K. L.; Brolo, A. G. *Acc. Chem. Res.* **2008**, *41*, 1049–1057.
(6) Lesuffleur, A.; Im, H.; Lindquist, N. C.; Lim, K. S.; Oh, S. H. *Opt. Express* **2008**, *16*, 219–224.
(7) Sharpe, J. C.; Mitchell, J. S.; Lin, L.; Sedoglavich, H.; Blaikie, R. J. *Anal. Chem.* **2008**, *80*, 2244–2249.
(8) Ji, J.; O'Connell, J. G.; Carter, D. J. D.; Larson, D. N. *Anal. Chem.* **2008**, *80*, 2491–2498.
(9) Lindquist, N. C.; Lesuffleur, A.; Im, H.; Oh, S.-H. *Lab Chip* **2009**, *9*, 382–387.
(10) Sinton, D.; Gordon, R.; Brolo, A. G. *Microfluid. Nanofluid.* **2008**, *4*, 107–116.
(11) Tetz, K. A.; Pang, L.; Fainman, Y. *Opt. Lett.* **2006**, *31*, 1528–1530.
(12) Ferreira, J.; Santos, M. J. L.; Rahman, M. M.; Brolo, A. G.; Gordon, R.; Sinton, D.; Girotto, E. M. *J. Am. Chem. Soc.* **2009**, *131*, 436–437.

10.1021/ac900221y CCC: $40.75
Published on Web 05/01/2009

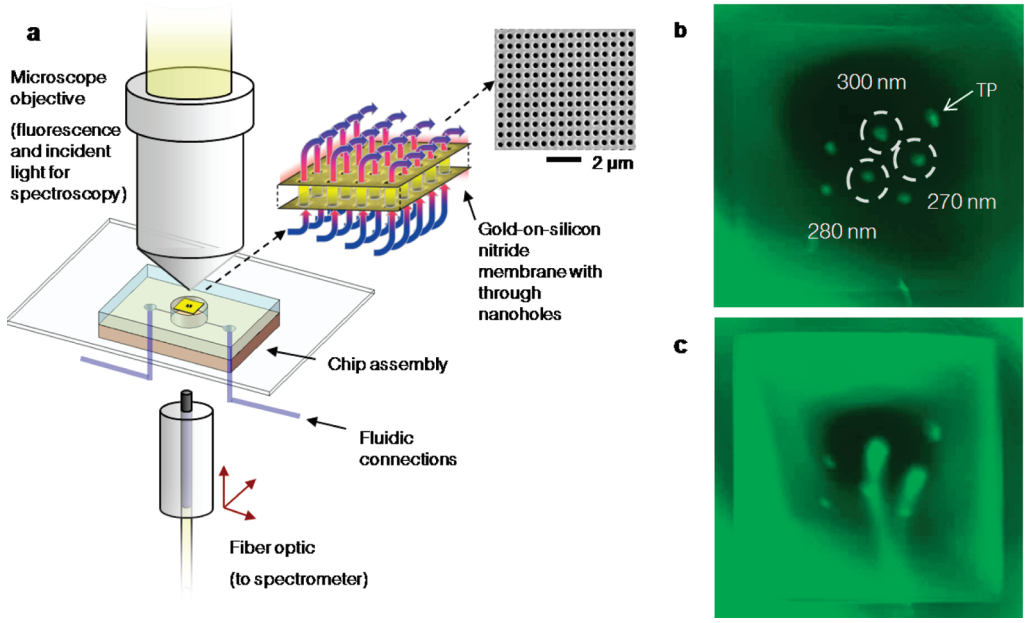

Figure 1. Flow-through nanohole arrays. (a) Schematic of the optical and fluidic test setup employed for both fluorescence tests and transmission spectroscopy. (b) Fluorescence image of the gold film with nanohole arrays, prior to the application of fluid pressure. The location of the arrays is indicated from the emission of the fluorescein solution on the underside. Arrays were 15 × 15 μm^2, with periodicities of 450 nm and hole diameters of 300, 280, 270 nm (as indicated), as well as 260 and 250 nm and the test pattern (TP). (c) Fluorescence image showing a dye buffer solution streaming from the three largest diameter arrays with 70 kPa applied pressure. The extent of the square silicon support frame (500 × 500 μm^2) becomes apparent as the fluid pressure deforms the membrane upward. (See Supporting Information, Movie 1).

diffusion at nanoscales and from solution sieving using nanostructures.[13,14]

In this paper, we demonstrate nanohole arrays with through-holes as flow-through SPR sensing elements. This paper describes the fabrication, microfluidic integration, and the application of flow-through nanohole array based sensors to chemical sensing. The flow-through array sensor introduced in this work combines the benefits of nanohole array based sensing with nanoconfined transport through the combination of nanofluidics and nanoplasmonics.

MATERIALS AND METHODS

Fabrication of the Nanohole Arrays. The circular nanohole arrays were fabricated by focused-ion beam (FIB) milling through a 100 nm thick gold films thermally evaporated on free-standing 100 nm Si_3N_4 with a 5 nm thick chromium adhesion layer. The evaporation was done commercially (EMF, Ithaca, NY). A variety of milling parameters were attempted in an effort to determine appropriate milling parameters for fabricating through-holes. For the arrays that demonstrated through-hole transport, the general milling parameters were as follows: the gallium ion beam was set to 30 keV for milling with a beam current of 50 pA, the typical beam spot size was 10 nm, and the dwell time of the beam at one pixel was 4 ms. The arrays consisted of 30 × 30 nanoholes with periodicities between 450−700 nm. Although several membranes were fabricated, the results from two (varying periodicity and varying hole-diameter) are reported in this work. In addition to SEM imaging, fabricated nanoholes were characterized by energy dispersive X-ray spectroscopy (EDX) and TEM imaging. These techniques were used to confirm the milling process, and specifically the extent of the milling through the silicon nitride. Observed transport and through-hole sensing, however, were the ultimate metrics employed to assess the fabricated sensors.

Fabrication of the Microfluidics and Flow Setup. The gold and silicon nitride film, immobilized on a silicon frame, was integrated into a poly(dimethylsiloxane) (PDMS) chip fabricated by soft-lithographic rapid prototyping.[15] Fluids were provided to the chip through syringe pumps; however, much care was required in the setup and running of the flow-through experiments to facilitate wetting of the nanoholes and avoid spurious pressure forces sufficient to rupture the membrane. Detailed information on the fabrication and assembly of the integrated chip and the experimental setup is provided in the Supporting Information.

Chemicals. Ethanol anhydrous, and 11-mercaptoundecanoic acid (MUA, 95%) were purchased from Sigma-Aldrich. Dithiobis-(succinimidyl undecanoate) (DSU, 92.7%) was purchased from Dojindo Laboratories. Sodium chloride (99%), sodium phosphate dibasic (99%), and potassium chloride (99%) were purchased from ACP, and fluorescein was purchased from Invitrogen. Pared box gene (PAX8) protein was provided by the Antibody Research Unit of the British Columbia Cancer Agency (Canada).

RESULTS AND DISCUSSION

Fabrication and Imaging of Flow-Through Nanohole Transport. Figure 1a shows a schematic of the suspended nanohole array integrated with microfluidics, and the setup for microscopic imaging and fiber-based transmission spectroscopy. Integrated

(13) Chou, I.-H.; Benford, M.; Beier, H. T.; Cote, G. L.; Wang, M.; Jing, M.; Kameoka, J. *Nano Lett.* **2008**, *8*, 1729–1735.
(14) Liang, X. G.; Chou, S. Y. *Nano Lett.* **2008**, *8*, 1472–1476.
(15) Duffy, D. C.; McDonald, J. C.; Schueller, O. J. A.; Whitesides, G. M. *Anal. Chem.* **1998**, *70* (23), 4974–4983.

service microfluidics delivered solutions and facilitated control of the solution pressure on the underside (Si_3N_4 side) of the membrane. Figure 1b shows a microscope image of six arrays of nanoholes, and a test pattern (TP) as lighter regions near the center of the image. Figure 1c shows the flow-through visualization using fluorescein. The dye was injected from the Si_3N_4 side of the template, and the image of the Au side showed pronounced streaming through the largest nanoholes under applied pressure (see Supporting Information, Movie 1). Of the six arrays fabricated with periodicity p = 450 nm, and different milling parameters, three arrays showed flow-through, corresponding to the hole diameters indicated in Figure 1b. The lack of apparent flow through three arrays was attributed to a combination of smaller hole diameter and insufficient dwell times (i.e., the milling time used to fabricate those arrays did not allow the formation of through holes). With the applied pressure of 10 psi (70 kPa), the total flow rate through the three arrays was estimated to be 5 μL/min, which is compatible with existing microfluidic delivery systems.[16] The arrays showed reversible deflection on the order of 30 μm under the applied pressure. The same SPR spectrum was obtained form the arrays before and after extensive flow-through tests, indicating that the nanostructured arrays were not functionally damaged. It is interesting to note that nanoporous Si membranes as thin as 15 nm have been shown to withstand pressure differentials on the order of one atmosphere.[17] Silicon nitride membranes in particular have been demonstrated previously as suitable substrates with which to observe resonant transmission through nanohole arrays.[18]

SPR Sensing Using Flow-Through Delivery of Analyte. Figure 2a shows the optical transmission spectra for the arrays of nanoholes in air (refractive index, n = 1.0008) and in ethanol (n = 1.3587). The spectral shift indicates the sensitivity of the resonant transmission to bulk refractive index.[19,20] In air, the SPR peak is at 575 nm, but in ethanol it shifted to λ = 625 nm (periodicity, p = 500 nm). The SPR is dominated from the exposed gold surface as the response from the gold−silicon nitride interface is expected to be damped by the chromium adhesion layer.[21] A sensitivity of 324 nm RIU^{-1} was found using glucose solutions with fine refractive index gradations between 1.3324 and 1.3568. This sensitivity is similar to previous nanohole SPR.[3,20] We note that flow-through sensing is compatible with recent strategies to increase nanohole SPR sensitivity relative to that of commercial SPR.[11]

The efficacy of flow-through nanohole arrays in the detection of surface adsorption events was tested. The solution containing the testing adsorbate was introduced in the microchamber in contact with the Si_3N_4 surface. In this way the sensor response to adsorption at the active gold surface is observed only after flow-through hole transport. The well-known self-assembly of

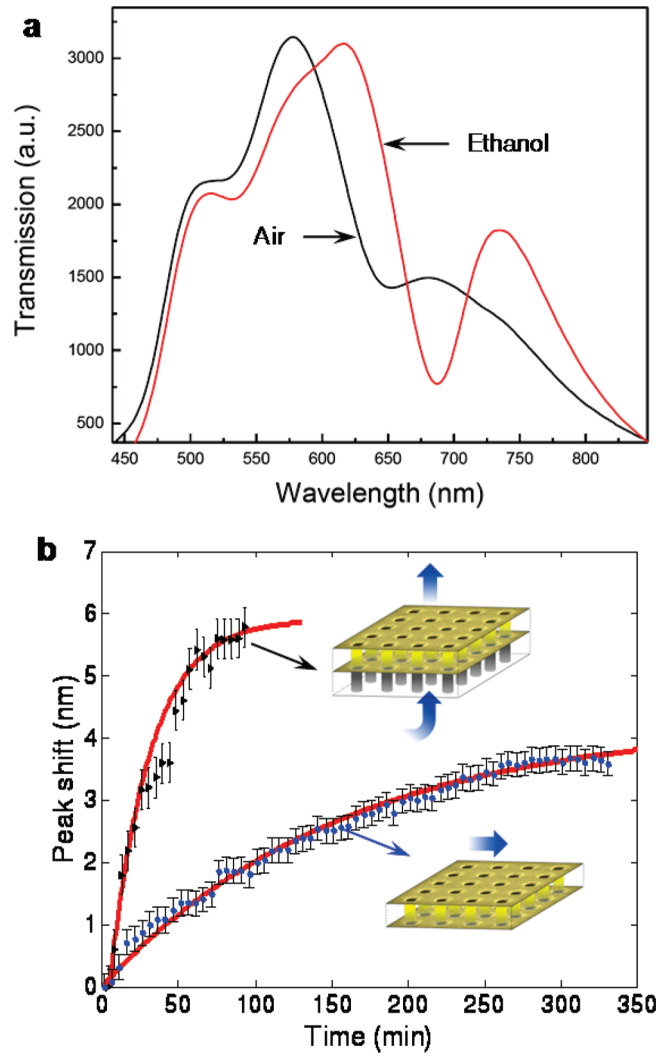

Figure 2. Response of flow-through nanohole arrays to bulk refractive index and surface adsorption: (a) Transmission spectra for air (n = 1.0008) and ethanol (n = 1.3587) in an array of periodicity, p = 500 nm; and (b) comparison of response to surface adsorption achieved with flow-over and flow-through formats as indicated inset. Measured peak shift (625 nm peak) is plotted as a function of time during flow through/over of an ethanol/MUA solution. As indicated in the inset, the flow-through sensor is operated with flow from the nonparticipating silicon nitride side to the active gold surface. The flow-through case results in a characteristic rate constant of k_{abs} = 3.8 × 10^{-2} min^{-1} as compared to k_{abs} = 6.4 × 10^{-3} min^{-1} for the flow-over case.

a monolayer of mercaptoundecanoic acid (MUA) on a gold surface followed.[22] The surface-adsorption was monitored in real-time by the shift in the λ = 625 nm peak as a 500 nM ethanolic solution of MUA streamed through the nanohole arrays from the Si_3N_4 side (p = 500 nm array). This MUA concentration resulted in adsorption time scales that enabled accurate timing of the experiments and negligible peak shift response from the bulk liquid. The real-time spectral red-shift caused by the MUA adsorption is shown in Figure 2b. The SPR peak position approached a steady state value indicating that the self-assembled monolayer approached completion. A similar test was conducted in flow-over format to compare the response

(16) Whitesides, G. M. *Nature* **2006**, *442*, 368–373.
(17) Striemer, C. C.; Gaborski, T. R.; McGrath, J. L.; Fauchet, P. M. *Nature* **2007**, *445*, 749–753.
(18) Grupp, D. E.; Lezec, H. J.; Ebbesen, T. W. *Appl. Phys. Lett.* **2000**, *77*, 1569–1571.
(19) Krishnan, A.; Thio, T.; Kim, T. J.; Lezec, H. J.; Ebbesen, T. W.; Wolff, P. A.; Pendry, J.; Martin-Moreno, L.; Garcia-Vidal, F. J. *Opt. Commun.* **2001**, *200*, 1–7.
(20) De Leebeeck, A.; Kumar, L. K. S.; De Lange, V.; Sinton, D.; Gordon, R.; Brolo, A. G. *Anal. Chem.* **2007**, *79*, 4094–4100.
(21) Genet, C.; van Exter, M. P.; Woerdman, J. P. *Opt. Commun.* **2003**, *225*, 331–336.
(22) Love, J. C.; Estroff, L. A.; Kriebel, J. K.; Nuzzo, R. G.; Whitesides, G. M. *Chem. Rev.* **2005**, *105*, 1103–1169.

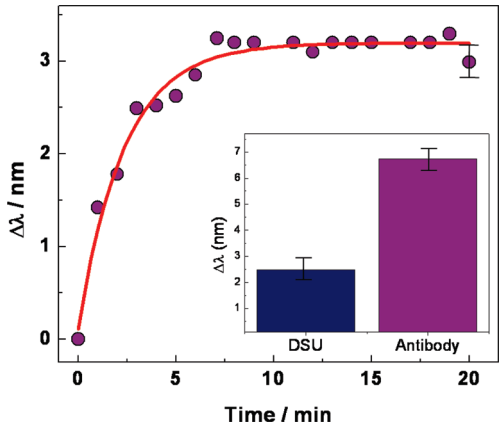

Figure 3. Response of flow-through nanohole arrays to sequential adsorption (periodicity of 450 nm). The wavelength versus time plot shows the peak-shift in response to the antibody (PAX8) adsorption, with a representative error bar on the last data point. Inset is a bar graph showing the peak shift in response to the initial DSU monolayer and the total peak shift in response to the DSU and the antibody.

achieved with flow-through sensing to the established flow-over practice. A channel of 50 μm × 2.5 mm cross-section covered the flow-over nanohole array, and the peak-shift was monitored in response to the ethanolic solution of MUA at a flow rate comparable to the flow-through case (~1 μL/min). The results of the flow-over test are also plotted in Figure 2b. The MUA adsorption was fit to a first-order kinetics curve.[23,24] The flow-through exponential fit indicates a characteristic rate constant of $k_{abs} = 3.8 \times 10^{-2}$ min^{-1} as compared to $k_{abs} = 6.4 \times 10^{-3}$ min^{-1} for the flow-over case. These results indicate a 6-fold improvement in the adsorption kinetics by employing nanoholes as nanochannels as compared to the established flow-over method.

Application to Sensing of Cancer Biomarker-Specific Antibody Binding. The label-free detection of cancer markers by SPR requires the immobilization of the antibody and detection through multiple adsorbed layers.[25] Here, the sequential assembly of a monolayer and the cancer biomarker PAX8 specific monoclonal antibody[26] were demonstrated with the flow-through scheme. The goal was to show that the flow-through approach enables the monitoring of multilayer adsorption. Dithiobis(succinimidyl)undecanoate (DSU) was first immobilized at the gold surface by flowing an ethanolic solution of DSU through the nanohole array (p = 450 nm), followed by a rinse step. A SPR shift of about 2.5 nm confirmed the formation of a monolayer of the adsorbed target. A 3.5 μg mL^{-1} (80 nM, with molecular weight of 43 kDa) aqueous solution of PAX8 protein in phosphate buffer solution was then transported through the nanoholes, and the adsorption kinetics were monitored by the SPR peak shift, as plotted in Figure 3. The sensor response shows a rapid increase over 7 minutes followed by a steady state. The PAX8 adsorption to DSU is non-specific and fits to a first order kinetic model, yielding an observable adsorption rate constant of 0.445 min^{-1}. The final relative SPR shifts corresponding to the DSU and the combined DSU/antibody adsorption are shown inset in Figure 3. The observed shifts, on the order of several nanometers, are readily observable with relatively simple infrastructure. These results demonstrate that the flow-through nanohole array based sensors may be employed to detect multiple adsorbed layers.

CONCLUSION

In summary, we have demonstrated flow-through nanohole array based sensing that combines the benefits of nanofluidics and nanoplasmonics in a single platform. It was shown that nanohole array based sensing may be performed with through nanoholes, or nanochannels, that facilitate enhanced transport of reactants to the active surface. As fluidic elements, the nanohole arrays served to parallelize the resistance and thus fluid handling and control were compatible between the parallel nanochannels and established microfluidic protocols. As optical elements, the nanohole arrays served to detect the adsorption of a monolayer as well as the step-by-step multilayer assembly of biomolecules as required for biosensing applications. A side-by-side comparison with the established flow-over methodology showed a 6-fold improvement in response time using the flow-through approach. Finally, we suggest that the flow-through nanohole arrays as combined plasmonic and fluidic elements exhibit many features that are particularly promising for sensing technologies. These features include a small foot-print, collinear optical detection, co-nanoconfinement of the analyte and the sensing electromagnetic field, enhanced transport through rapid diffusion at nanoscales, and a solution-sieving action for surface based sensing. In addition, the flow-through nanohole array scheme presented here is ideal for in-hole sensing. Exclusive use of the in-hole surface reduces the number of adsorption sites, while providing a large spectral shift, improving the limit of detection into the attomolar range. The flow-through approach greatly enhances transport of analytes to the active area inside the holes. We anticipate that the flow-through nanohole arrays will enable highly integrated, multiplexed, label-free diagnostics for which efficient screening of multiple biomarkers is essential.

ACKNOWLEDGMENT

We gratefully acknowledge funding support for this work from NSERC, CFI, and BCKDF. This collaboration has been facilitated by an NSERC Strategic Projects Grant with the BC Cancer Agency and Micralyne Inc. We thank Paul Wood and Michael Fryer for helpful discussions. We also thank the Government of Canada for the scholarship provided by the Graduate Students' Exchange Program (GSEP) to J.F.

SUPPORTING INFORMATION AVAILABLE

Additional information as noted in the text. This material is available free of charge via the Internet at http://pubs.acs.org.

Received for review January 29, 2009. Accepted April 23, 2009.

AC900221Y

(23) Karpovich, D. S.; Blanchard, G. J. *Langmuir* **1994**, *10*, 3315–3322.
(24) Peterlinz, K. A.; Georgiadis, R. *Langmuir* **1996**, *12*, 4731–4740.
(25) Shumaker-Parry, J. S.; Aebersold, R.; Campbell, C. T. *Anal. Chem.* **2004**, *76*, 2071–2082.
(26) Bowen, N. J.; Logani, S.; Dickerson, E. B.; Kapa, L. B.; Akhtar, M.; Benigno, B. B.; McDonald, J. F. *Gynecol. Oncol.* **2007**, *104*, 331–337.

Appendix B

Flow-Trough vs Flow-Over: Analysis of Transport and Binding in Nanohole Array Plasmonic Biosensors

Anal. Chem. **2010,** *82,* 10015–10020

Flow-Through vs Flow-Over: Analysis of Transport and Binding in Nanohole Array Plasmonic Biosensors

Carlos Escobedo,[†] Alexandre G. Brolo,[‡] Reuven Gordon,[§] and David Sinton*,[†]

Mechanical Engineering, Chemistry, and Electrical and Computer Engineering, University of Victoria, Victoria, BC, Canada

We quantify the efficacy of flow-through nanohole sensing, as compared to the established flow-over format, through scaling analysis and numerical simulation. Nanohole arrays represent a growing niche within surface plasmon resonance-based sensing methods, and employing the nanoholes as nanochannels can enhance transport and analytical response. The additional benefit offered by flow-through operation is, however, a complex function of operating parameters and application-specific binding chemistry. Compared here are flow-over sensors and flow-through nanohole array sensors with equivalent sensing area, where the nanohole array sensing area is taken as the inner-walls of the nanoholes. The footprints of the sensors are similar (e.g., a square 20 μm wide flow-over sensor has an equivalent sensing area as a square 30 μm wide array of 300 nm diameter nanoholes with 450 nm periodicity in a 100 nm thick gold film). Considering transport alone, an analysis here shows that given equivalent sensing area and flow rate the flow-through nanohole format enables greatly increased flux of analytes to the sensing surface (e.g., 40-fold for the case of $Q = 10$ nL/min). Including both transport and binding kinetics, a computational model, validated by experimental data, provides guidelines for performance as a function of binding time constant, analyte diffusivity, and running parameters. For common binding kinetics and analytes, flow-through nanohole arrays offer ~10-fold improvement in response time, with a maximum of 20-fold improvement for small biomolecules with rapid kinetics.

Metallic films with ordered arrays of nanoholes exhibit surface plasmon resonance (SPR) that facilitates enhanced optical transmission through the holes.[1−4] The influence of the near-surface refractive index on the resulting transmission has been employed for sensing applications.[5,6] Nanohole arrays represent a growing niche within SPR-based sensing methods.[7] Specifically, as compared to traditional SPR sensing, nanohole arrays can provide a smaller foot-print, denser integration, increased potential for multiplexing and simplified collinear optical detection in which analyte binding is determined directly from light that is transmitted through the holes.[7−10] Moreover, the sensitivity of nanohole arrays has been reported to be similar to traditional SPR.[11] Ferreira et al.[6] demonstrated that in contrast to traditional SPR, the top gold surface is not necessarily the dominant sensing surface in nanohole arrays. Rather, the molecular binding that occurs on the inner surface of the nanoholes can dominate the sensor response.[6] This finding highlighted the importance of transporting analytes to the interior of nanoholes.

In order to enhance the transport of analyte to the in-hole sensing surface we developed a flow-through nanohole array sensing format.[12] All previous nanohole array sensing involved dead-ended holes and thus relied on cross-stream analyte transport within a microchannel flow as is typical for surface based biosensors. This traditional flow-over format is shown schematically in Figure 1a. In contrast, the flow-through strategy capitalizes on the unique nature of nanohole plasmonic sensing elements in that they are also fundamentally nanochannels.[12] The flow-through strategy is shown in Figure 1b. An array of through-nanoholes serves as nanochannels in parallel and provides an analyte sieving action that is unique among surface-based sensors. Our experimental results demonstrated proof-of-concept flow-through biosensing and a 6-fold improvement in response time compared to the traditional microfluidic flow-over method when applied to monitor a monolayer adsorption process.[12] More recently, Yanik

* To whom correspondence should be addressed. E-mail: dsinton@uvic.ca.
† Mechanical Engineering.
‡ Chemistry.
§ Electrical and Computer Engineering.

(1) Ebbesen, T. W.; Lezec, H. J.; Ghaemi, H. F.; Thio, T.; Wolff, P. A. *Nature* **1998**, *391*, 667–669.
(2) Genet, C.; Ebbesen, T. W. *Nature* **2007**, *445*, 39–46.
(3) Barnes, W. L.; Dereux, A.; Ebbesen, T. W. *Nature* **2003**, *424*, 824–830.
(4) Kwak, E. S.; Henzie, J.; Chang, S. H.; Gray, S. K.; Schatz, G. C.; Odom, T. W. *Nano Lett.* **2005**, *5*, 1963–1967.
(5) Gordon, R.; Sinton, D.; Kavanagh, K. L.; Brolo, A. G. *Acc. Chem. Res.* **2008**, *41*, 1049–1057.
(6) Ferreira, J.; Santos, M, J. L.; Rahman, M. M.; Brolo, A. G.; Gordon, R.; Sinton, D.; Girotto, E. M. *J. Am. Chem. Soc.* **2009**, *131*, 436+.
(7) Sinton, D.; Gordon, R.; Brolo, A. G. *Microfluid. Nanofluid.* **2008**, *4*, 107–116.
(8) DeLeebeeck, A.; Kumar, L. K. S.; deLange, V.; Sinton, D.; Gordon, R.; Brolo, A. G. *Anal. Chem.* **2007**, *79*, 4094–4100.
(9) Brolo, A. G.; Gordon, R.; Leathem, B.; Kavanagh, K. L. *Langmuir* **2004**, *20*, 4813–4815.
(10) Lindquist, N. C.; Lesuffleur, A.; Im, H.; Oh, S. H. *Lab Chip* **2009**, *9*, 382–387.
(11) Tetz, K. A.; Pang, L.; Fainman, Y. *Opt. Lett.* **2006**, *31*, 1528–1530.
(12) Eftekhari, F.; Escobedo, C.; Ferreira, J.; Duan, X.; Girotto, E. M.; Brolo, A. G.; Gordon, R.; Sinton, D. *Anal. Chem.* **2009**, *81*, 4308–4311.

10.1021/ac101654f
Published on Web 11/16/2010

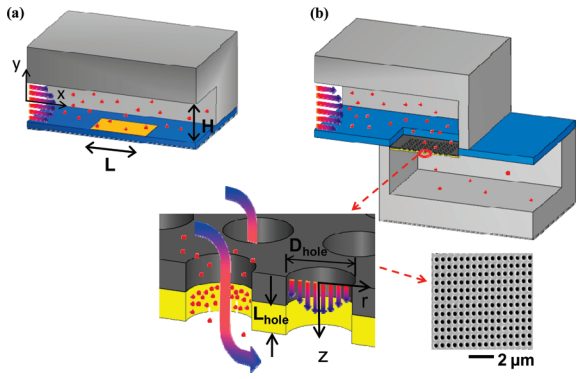

Figure 1. Schematic representation of the two sensing formats considered in this work: (a) a typical flow-over format with a square surface-based sensor within a microfluidic channel, and (b) the flow-through nanohole array format where analyte solution passes from one microchannel to another via an array of nanoholes/nanochannels in parallel.

et al.[13] demonstrated a 14-fold improvement in the mass transport rate of IPA as compared to an otherwise similar flow-over system, and Jonsson et al.[14] presented flow-through plasmonic sensing using a short-range ordered nanoscale pores. These recent isolated results indicate the excitement and promise surrounding flow-through nanohole based plasmonic sensing. Facilitating flow-through sensing is, however, more complicated than flow-over which can be achieved with a single fluidic channel. For a given application the potential benefit offered by flow-through sensing will be a function of operating parameters and binding kinetics of the specific analyte system.

Transport and binding kinetics have been studied extensively for the flow-over format typical of surface based microsensors and nanowires.[15−23] Zimmermann et al.[24] investigated the analyte surface capture using a 2-D model under different input parameters such as flow rate and binding kinetics constants. Hu et al.[17] presented a 2-D flow-over model and demonstrated better performance with electrokinetically driven immunoassays over pressure-driven ones in terms of reaction kinetics. Fu et al.[18] presented a 2-D computational model to identify operating ranges for sensitivity improvement in microfluidic heterogeneous immunoassays. Squires et al.[21] provided an elegant and practical analysis of microfluidic and nanowire surface-based sensors highlighting limiting factors in each case.

The parallel nature and length scales involved in the flow-through sensing is a deviation from the established flow-over format. Recent experimental demonstrations show significant improvements in response for isolated monolayer adsorption and analyte systems.[12−14,17,25,26] The efficacy of this strategy as compared to the established flow-over method has not, however, been quantified as a function of running parameters and binding kinetics, and no guidelines are available to assess applicability as a function of surface chemistry specifics.

In this work, the efficacy of flow-through nanohole sensing, as compared to the established flow-over format, is quantified as a function of operating parameters and surface chemistry through scaling analysis and numerical simulation. Flow-through and flow-over sensors are compared with equivalent sensing area. That is, the planar sensing area of the flow-over sensor is equivalent to the total inner-wall area of the nanoholes in the nanohole array. The footprints of the sensors are similar (e.g., a square 20 μm wide flow-over sensor has an equivalent sensing area as a square 30 μm wide array of 300 nm diameter nanoholes with 450 nm periodicity in a 100 nm thick gold film). The goals of this work are to (1) quantify the advantage offered by flow-through sensing; and (2) serve as a guide to assess the benefit of employing a flow-through scheme for a given sensing application.

BACKGROUND

Model Systems. The two sensing formats considered in this work are shown schematically in Figure 1. A typical flow-over format with a square surface-based sensor within a microfluidic channel is shown in Figure 1a, and the flow-through nanohole array format is shown in Figure 1b. For simplicity, the flow-over sensor geometry was fixed as square with a side length equivalent to the channel width, L, in a microchannel of height, H. The flow-through sensor assumed an array of parallel nanoholes milled through a 100 nm thick silicon nitride membrane with a 100 nm gold coating. The size of the flow-through sensor array was set such that the total inner-wall sensing area was equivalent to the area of the flow-over sensor. In both cases, the analyte was transported by a pressure-driven flow.

Simulations. Fluid flow and mass transport were modeled in both systems using Finite Element Analysis software COMSOL Multiphysics (COMSOL, Sweden) under the assumption of unidirectional 2-D pressure-driven flow, and employing the Stokes flow approximation typical of microfluidic and nanofluidic liquid flows.[27] The flow-over sensor model included a 2D Cartesian domain along the midplane of the microchannel as shown in Figure 1a. The flow-through nanohole array based sensor model is a 2-D axisymmetric domain along a nanohole cross section, as shown in Figure 1b. Details on the computational models used for the simulations can be found in the Supporting Information (SI). In order to validate the computational model, modeling results were compared with experimental results for the flow-through geometry. With respect to characteristic binding response time, the model and the experimental data agreed to within ±5%. Details on the model validation and the computational and experimental results are provided in the SI.

(13) Yanik, A. A.; Huang, M.; Artar, A.; Chang, T. Y.; Altug, H. *Appl. Phys. Lett.* **2010**, *96*.
(14) Jonsson, M. P.; Dahlin, A. B.; Feuz, L.; Petronis, S.; Hook, F. *Anal. Chem.* **2010**, *82*, 2087–2094.
(15) Sheehan, P. E.; Whitman, L. J. *Nano Lett.* **2005**, *5*, 803–807.
(16) Squires, T. M.; Quake, S. R. *Rev. Mod. Phys.* **2005**, *77*, 977–1026.
(17) Hu, G.; Gao, Y.; Li, D. *Biosens. Bioelectron.* **2007**, *22*, 1403–1409.
(18) Fu, E.; Nelson, K. E.; Ramsey, S. A.; Foley, J. O.; Helton, K.; Yager, P. *Anal. Chem.* **2009**, *81*, 3407–3413.
(19) Lebedev, K.; Mafé, S.; Stroeve, P. *J. Colloid Interface Sci.* **2006**, *296*, 527–537.
(20) Parsa, H.; Chin, C. D.; Mongkolwisetwara, P.; Lee, B. W.; Wang, J. J.; Sia, S. K. *Lab Chip* **2008**, *8*, 2062–2070.
(21) Squires, T. M.; Messinger, R. J.; Manalis, S. R. *Nat. Biotechnol.* **2008**, *26*, 417–426.
(22) Feuz, L.; Jonsson, P.; Jonsson, M. P.; Hook, F. *ACS Nano* **2010**, *4*, 2167–2177.
(23) Kim, D. R.; Zheng, X. L. *Nano Lett.* **2008**, *8*, 3233–3237.
(24) Zimmermann, M.; Delamarche, E.; Wolf, M.; Hunziker, P. *Biomed. Microdevices* **2005**, *7*, 99–110.
(25) Anker, J. N.; Hall, W. P.; Lyandres, O.; Shah, N. C.; Zhao, J.; Van Duyne, R. P. *Nat. Mater.* **2008**, *7*, 442–453.
(26) Canpean, V.; Astilean, S. *Lab Chip* **2009**, *9*, 3574–3579.
(27) Jensen, M. J.; Stone, H. A.; Bruus, H. *Phys. Fluids* **2006**, *18*.

Quantification of Transport to the Sensing Surface. Sensing requires transport of analyte to the surface and subsequent binding. The idealized case where the binding kinetics are very rapid and the sensor does not saturate provides a useful comparison of the transport achieved with each sensor format. For this case, analyte molecules are transported to the sensing area at steady state through a combination of convection and diffusion. The total molecular flux input into the system, J_0, is a function of the bulk concentration, c_0, and the total flow rate, Q. (In this work, flux, as indicated by a capital J, corresponds to the flux density integrated over area, and is thus a scalar.) The molecular flux to the sensing surface is the diffusive flux, J_D, which scales with the sensing area, A, diffusivity, $\mathscr{D}$, bulk concentration, c_0, and scales inversely with the thickness of the concentration gradient at the surface, δ[21] (see also the analyte depletion zone discussion in the SI). The total analyte flux to the sensing surface, J_D, was quantified here through integrating the flux density at the sensor surface in the numerical simulations. While nondimensionalization of transport parameters can be insightful (an elegant treatment is provided by Squires et al.[21]), the dimensional form of the molecular flux to the sensor surface J_D, (mol/s) was employed here for clarity in comparing transport between the flow over and flow-through cases. The transport to the sensor can also be represented as a fraction of the total molecular flux into the system, or J_D/J_0.

Quantification of Binding Kinetics. The basis for the parameter employed to quantify, and generalize, binding kinetics is explained here. Considering the case of where transport of analyte to active sites occurs much more rapidly than the binding kinetics (or "perfect transport"), the rate of change of surface concentration $c_S(t)$ of analyte adsorbed at the sensing surface, assuming first-order Langmuir kinetics,[28] is described by

$$\frac{\partial c_S}{\partial t} = k_{on} c_0 (b_0 - c_S) - k_{off} c_S \quad (1)$$

where k_{on} is the adsorption constant, k_{off} is the desorption constant, c_0 is the analyte concentration in the bulk and b_0 is the total surface concentration of active potential binding sites.

Equation 1 yields an analytical expression[17,29−31] for the surface concentration of adsorbed species as follows:

$$c_S(t) = c_S^{Eq}(1 - e^{-t/\tau}),\ c_S^{Eq} = \frac{b_0 c_0 k_{on}}{k_{on} c_0 + k_{off}},$$
$$K_A = k_{on}/k_{off}, \tau = (k_{on} c_0 + k_{off})^{-1} \quad (2)$$

where c_S^{Eq} is the equilibrium surface concentration as defined by the Langmuir adsorption equation, K_A is the affinity constant, and the time scale, τ, characterizes the time required for the sensor to reach the equilibrium concentration.[21] On this basis, τ is used in this work to quantify and compare the binding kinetics of various analyte systems.

RESULTS AND DISCUSSION

The efficacy of flow-through nanohole array based sensing depends on both transport and binding kinetics. The flow-through approach has implications mainly for transport. The scaling analysis below first focuses on the role of transport in isolation, using the assumption of perfect, rapid, reaction kinetics. Physically, this situation corresponds to a sensing surface that absorbs analyte immediately and never saturates. The value in considering this simplified case is that the analyte transport can be quantified in isolation from binding/saturation considerations. Following these transport-only analyses, both transport and binding kinetics are included.

Transport Scaling Analysis. For the flow-over case (Figure 1a) with rapid surface reaction kinetics, the flux of analyte to the sensing surface is a function of Peclet number, the ratio of the total convective flux of molecules to the diffusive flux at the sensing surface. Based on channel height, H, average velocity, U_{ch}, and diffusivity, $\mathscr{D}$, the Peclet number is given by $Pe_{ch} = U_{ch}H/\mathscr{D}$.[21]

The flow-through case (Figure 1b) is a nanohole array with the same sensing area as the flow-over case, and is provided the same solution concentration at the same volume flow rate, Q. The sensing area of a nanohole array is taken as the inner hole surface,[6] and thus the number of nanoholes required for equivalent sensing area to that of a square flow-over sensor is $N = L^2/A_{active}$ where the sensing area for a nanohole of diameter, D, and gold thickness, L_{hole}, is $A_{active} = \pi D L_{hole}$. The resulting number of holes is $N = L^2/\pi D L_{hole}$. For the case of $L = 20$ μm, $L_{hole} = 100$ m and $D = 300$ nm, the number of holes is approximately 4240, which is an array with around 65 by 65 holes. With a periodicity of 450 nm, the array will extend over an area of approximately 30×30 μm. Such a configuration is typical of nanohole array based sensors.[10,32−34] It is noteworthy that for typical flow-through nanohole geometries, the total footprint of the flow-through nanohole array is on the same order of magnitude as the planar flow-over sensor of identical sensing area. The total flow rate is divided between N number of holes, resulting in an in-hole average velocity of $U_{hole} = U_{ch}(H/L)(4L_{hole}/D)$. Since the diameter of the hole and the thickness of the gold are typically similar ($L_{hole} \sim 100$ nm is thick enough to be optically opaque but thin enough to mill through using a focused ion beam[35]) the term $(4L_{hole}/D)$ is a small correction, on the order of unity. Thus for a microchannel of approximately square cross-section ($L \sim H$) the average flow velocity in the flow-over case is approximately equivalent to that inside the nanoholes. The resulting Peclet number in the nanoholes is given by,

$$Pe_{hole} = \frac{U_{hole} D}{\mathscr{D}} = \frac{4 Q L_{hole}}{L^2 \mathscr{D}} \quad (3)$$

With both systems provided the same flow rate, the ratio of Peclet numbers provides a measure for comparing the diffusive

(28) Goodrich, J. A., Kugel, J. F. *Binding and kinetics for molecular biologists;* Cold Spring Harbor Laboratory Press: Cold Spring Harbor, NY, 2007.
(29) Chaiken, I.; Rose, S.; Karlsson, R. *Anal. Biochem.* **1992**, *201*, 197–210.
(30) Myszka, D. G.; He, X.; Dembo, M.; Morton, T. A.; Goldstein, B. *Biophys. J.* **1998**, *75*, 583–594.
(31) Gervais, T.; Jensen, K. F. *Chem. Eng. Sci.* **2006**, *61*, 1102–1121.
(32) Yang, J.-C.; Ji, J.; Hogle, J. M.; Larson, D. N. *Nano Lett.* **2008**, *8*, 2718–2724.
(33) Gordon, R.; Brolo, A. G.; Sinton, D.; Kavanagh, K. L. *Laser Photonics Reviews* **2010**, *4*, 311–335.
(34) Im, H.; Lesuffleur, A.; Lindquist, N. C.; Oh, S.-H. *Anal. Chem.* **2009**, *81*, 2854–2859.
(35) Yue, S. L., Gu, C. Z. *7th IEEE Conference on Nanotechnology*; 2007; Vol. 1−3, pp 632−635.

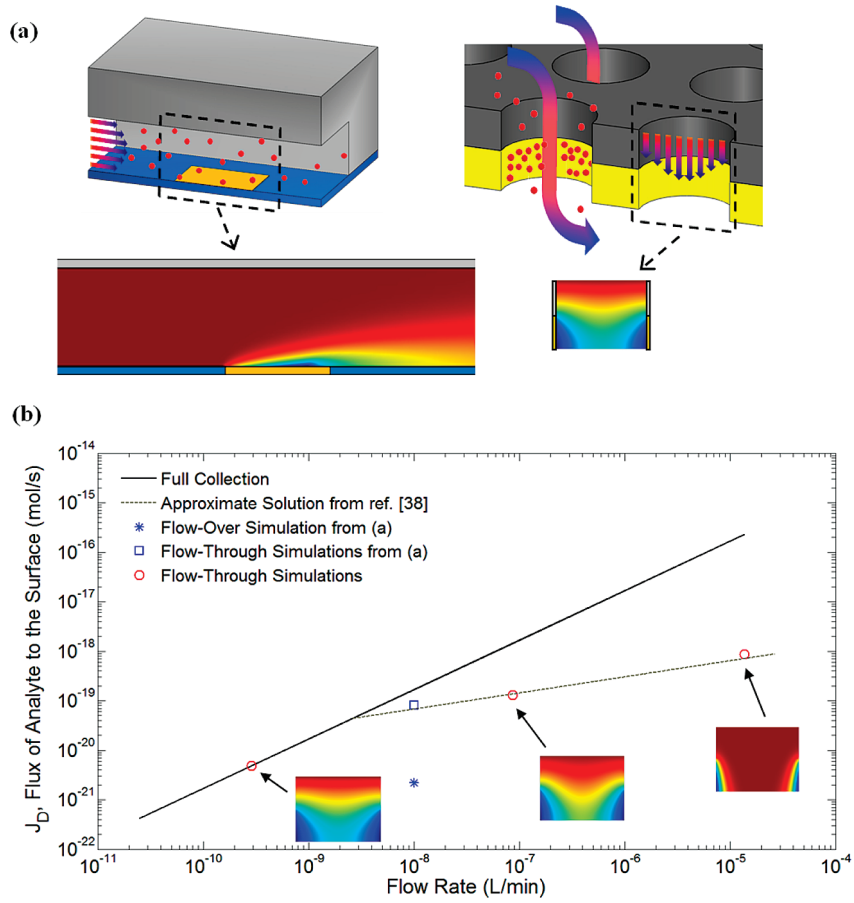

Figure 2. Comparison of transport in flow-over and flow-through sensing formats. (a) Schematic of the flow-over format (left) and flow-through format (right). Simulation results indicate analyte collection in the flow-over sensor ($L = H = 20\ \mu$m), and a flow-through nanohole ($D = 300$ nm, $L_{hole} = 100$ nm) array of equivalent sensing area. Both are provided the same flow rate ($Q = 10$ nL/min), $\mathscr{D} = 1 \times 10^{-10}$m^{2}s^{-1} and the surface concentration was fixed ($c_S(t) = 0$) to consider transport in isolation from binding kinetics. (b) Extension of results shown in (a) plotted as total molecular flux to the sensing surface, J_D, versus flow rate. The continuous line indicates the fundamental limit where all incoming analyte molecules are transported to the sensing surface. The dashed line represents the flux estimated using the solution for mass transfer to a two-dimensional sensor as given by Ackerberg et al.[38] Values corresponding to microchannel and nanohole cases from (a) are plotted, as indicated as in the legend, and sample flow-through flow-through computational results are shown inset.

transport of molecules to the sensing surface in each case as follows,

$$\frac{Pe_{ch}}{Pe_{hole}} = \frac{QL^2\mathscr{D}}{4QL_{hole}L\mathscr{D}} = \frac{L}{4L_{hole}} \tag{4}$$

Flow-over sensors in commercial systems have lengths on the order of $L \sim 40\ \mu$m,[30,36,37] while the depth of flow-through nanoholes, $L_{hole} \sim 100$ nm, is fixed by optical and fabrication considerations. Inputing these geometrical constraints in eq 4 provides a Peclet number ratio of 10^2. In other words, given the same flow rate and sensing area, the Peclet number inside the nanoholes is 2 orders of magnitude less than that in the channel with a typical flow-over sensor operating under otherwise similar conditions. The above scaling analysis suggests that flow-through nanohole array based sensing can provide up to 2 orders of magnitude more diffusive flux of analyte to the sensing surface as compared to a flow-over sensor, given the same sensing area and flow rate. This potential is further quantified in the computational transport analysis below.

Computational Transport Analysis. In order to provide a more detailed analysis of the transport in both sensing platforms, a computational model is employed. As in the scaling analysis above, binding kinetics in this section are assumed to be perfect and the surface concentration is set to $c_S(t) = 0$. This simplification allows the transport characteristics of the two sensing formats to be compared in isolation from surface binding kinetics (finite surface reaction rates and surface saturation are introduced in following section). The flow-over sensor is a square planar surface with $L = 20\ \mu$m. The flow-through sensor is an array of nanoholes with $D = 300$ nm, a gold thickness of $L_{hole} = 100$ nm and 10^3 nanoholes for equivalent sensing area to the flow-over case.

Figure 2a shows the results of the steady state simulations with perfect reaction kinetics for the case where $Q = 10$ nL/min of 1nM solution (with analyte diffusivity, $\mathscr{D} = 1 \times 10^{-10}$m^{2}s^{-1}) was provided to both systems. In the flow-over case, the depletion region is thin compared to the channel width and as a result the majority of target molecules are swept downstream before they can diffuse to the sensing area. In the nanohole flow-through case, the depletion zone extends across the entire

(36) Schuck, P.; Millar, D. B.; Kortt, A. A. *Anal. Biochem.* **1998**, *265*, 79–91.

Table 1. Diffusion Coefficient, Adsorption Constant, Desorption Constant, Affinity Constant Characteristic Binding Time Scale and Surface Concentration at Equilibrium for Analyte Systems 1−4

	analyte system 1	analyte system 2	analyte system 3	analyte system 4
$\mathscr{D}(m^2s^{-1})$	1×10^{-11}	1×10^{-10}	1×10^{-9}	1×10^{-9}
$k_{on}(s^{-1}M^{-1})$	1×10^{4}	2×10^{6}	1×10^{3}	1×10^{2}
$k_{off}(s^{-1})$	1×10^{-4}	2×10^{-3}	1×10^{-8}	1×10^{-7}
$K_A(M^{-1})$	1×10^{8}	1×10^{9}	1×10^{11}	1×10^{9}
τ (s)	1×10^{2}	4×10^{-1}	1×10^{3}	1×10^{4}
$c_S^{Eq}(mol\cdot m^{-2})$	1×10^{-6}	1×10^{8}	1×10^{8}	1×10^{8}

nanohole cross-section as the majority of analytes are transported to the inner-wall sensing surface.

Figure 2b quantifies analyte flux to the surface as function of total flow rate. Due to the mixture of length scales involved, both the flux of analyte to the sensor surface and the flow rate are given in dimensional forms, mol/s and L/min, respectively. The continuous line indicates the limit where all analytes entering the sensing platform (i.e., J_0) are transported to the sensing surface. The dashed line is the flux as estimated using the asymptotic solution for mass transfer for a two-dimensional sensor provided by Ackerberg et al.[38] Several aspects of Figure 2 are noteworthy: (1) As flow rate increases, total flux to the sensing surface increases in accordance with expected results;[38] (2) At low flow rates such as the point shown at $Q = 0.3$ nL/min, essentially all incoming analyte is transported to the sensing surface ($J_D/J_0 > 99\%$); (3) For the specific flow-through/flow-over comparison cases (shown in Figure 1a), the flow-through sensing format provides 40-fold more flux of analyte to the sensing surface (given same flow rate and sensing area).

Computational Transport and Binding Analysis. Finite binding kinetics, in general, have the effect of slowing down sensor response as compared to the idealized cases discussed above. In this context, it is informative to determine the kinetic conditions under which the flow-through nanohole array strategy is beneficial, and the conditions under which it provides negligible benefit. Toward this end, binding kinetics was included in the model for both the flow-over and flow-through cases. In order to characterize the kinetic binding systems in a way that is as general and widely applicable as possible, the characteristic binding time scale τ from eq 2 is employed.

The response times of the flow-over and flow-through sensing formats for four different analyte systems with binding kinetics and surface concentration saturation at equilibrium are summarized in Table 1. Analyte System 1 represents the binding of a relatively large, slow molecule with favorable binding kinetics, such as bovine serum albumin[39] (BSA). Analyte System 2 is an antibody−antigen system modeled after the common cancer biomarker CA125.[40] Analyte Systems 3 and 4 represent a generic small molecule bioassay with "on" kinetics that are fast and slow, respectively. Diffusion of the analyte to the surface will play a major role in cases 1 and 2, but the adsorption kinetics will be more important in cases 3 and 4. The binding kinetic time

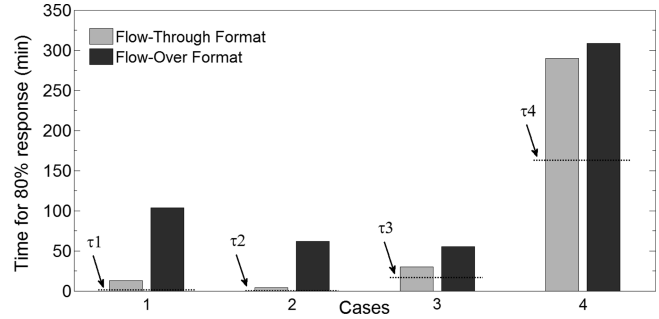

Figure 3. Comparison of flow-over and flow-through sensing formats for four analyte systems. Time for 80% of the equilibrium analyte concentration to be adsorbed to the surface is plotted for both sensing formats. The sensors had equivalent sensing area with geometries as employed in Figure 2, and both systems were provided 10 nL/min. The flow-through format provides significant gains for Analyte Systems 1 and 2, however, only a modest benefit was achieved in Systems 3 and 4. Particularly in Analyte System 4, the benefit of flow-through transport is obscured by the long characteristic time binding time. Characteristic binding time scale for each case is shown as a dashed line as indicated.

constant, τ, is calculated for each system in Table 1, and this value represents a minimum time scale (or maximum rate) for sensor response based on perfect transport. In this sense, τ imposes a speed limit that can be attained, but not exceeded, with improved transport schemes.

Figure 3 shows the response from each analyte system when implemented in flow-over and flow-through sensing formats. The sensors had equivalent sensing area with geometries as applied in Figure 2, and both systems were provided 10 nL/min and $c_0 = 10^{-9}$M. The response time was taken as the time for the sensor to have 80% of the equilibrium analyte concentration adsorbed to the surface. For system 1, the flow-through nanohole response time was approximately equivalent to the binding time scale, τ, indicating that the flow-through system approximates the perfect transport limit. For the flow-over case the sensor response was approximately eight times slower. The flow-through strategy also provided much faster response when applied to the Analyte System 2 (CA125 cancer biomarker). For Analyte System 3, however, the benefit of the flow-through nanohole approach was less significant. This was due to a combination of the smaller molecular size (increasing the diffusive transport rate in both systems) and the much slower (i.e., rate limiting) binding kinetics as indicated by the large characteristic τ value. Analyte System 4 represents a further extreme, where binding kinetics limit the process entirely. Although the flow-through strategy provided a faster response, the time savings are not significant as compared to the long characteristic binding time ($\tau = 10^3$s.) These cases illustrate a spectrum of sensor responses for four analyte systems, and while the flow-through format provides significant gains for Analyte System 1 and 2, only a modest benefit was achieved in Systems 3 and 4.

Figure 4 provides sensor time response as a function of the characteristic binding time scale, τ, spanning 5 orders of magnitude. In these simulations, the adsorption constant was varied as $10^2 \le k_{on} \ge 10^7$ $M^{-1}s^{-1}$, keeping constant values of k_{off}, $c_0 = 10^{-6}$ M and $Q = 2$ μL/min. The desorption kinetic constant, k_{off}, was fixed at a constant and sufficiently low value (10^{-5} s^{-1}) to

(37) Natarajan, S.; Katsamba, P. S.; Miles, A.; Eckman, J.; Papalia, G. A.; Rich, R. L.; Gale, B. K.; Myszka, D. G. *Anal. Biochem.* **2008**, *373*, 141–146.
(38) Ackerberg, R. C.; Patel, R. D.; Gupta, S. K. *J. Fluid Mech.* **1978**, *86*, 49–65.
(39) Meechai, N.; Jamieson, A. M.; Blackwell, J. *J. Colloid Interface Sci.* **1999**, *218*, 167–175.
(40) Xie, C.; Dong, C.; Ren, J. *Talanta* **2009**, *79*, 971–974.

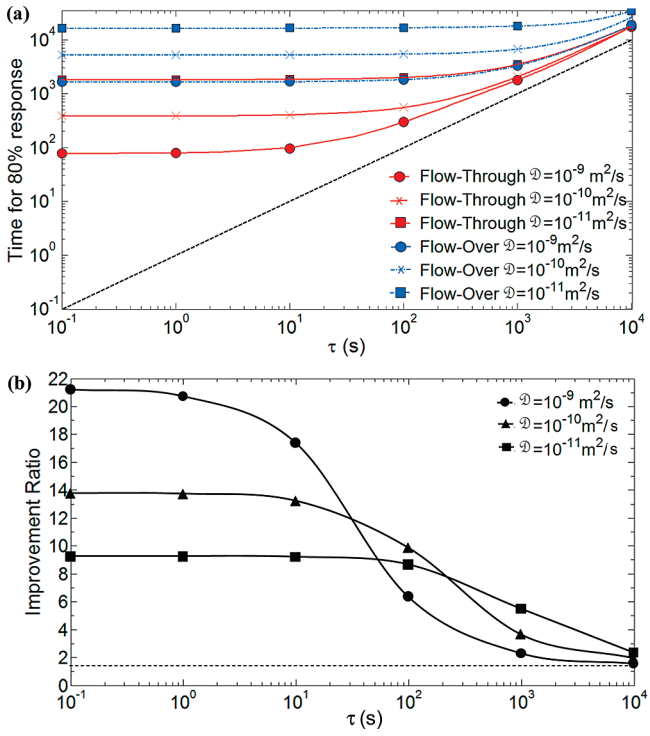

Figure 4. Response time improvement of the flow-through sensing format as a function of characteristic binding time scale, τ. The results shown in (a) were obtained from simulations using the COMSOL model described in the text, and varying k_{on} from 10^2 to 10^7 $M^{-1}s^{-1}$ for three different molecule sizes. In all cases, c_0 is higher than $1/K_A$ to ensure saturation of the sensing surface. The flow-through format provides maximum benefit at $\tau \leq 10^2$ s. As τ increases, all the response curves approach the limit $t = \tau$. In (b), the results from (a) are shown as a flow-through-to-flow-over response time improvement factor. The highest benefit, around 20-fold, is achieved for rapidly diffusing analyte and smaller τ values; and between 10- to 20-fold for values representing typical biosensing applications.[40,42,43]

ensure the process was dictated by the "on" kinetics (this is representative of many bioassays, having k_{on} values in the range of 10^3 to 10^5 $M^{-1}s^{-1}$ and k_{off} values $\sim 10^{-5}$).[39−41] In order to include the effect of the analyte size, the simulations were performed considering three different analyte diffusivities, 10^{-11}, 10^{-10}, and 10^{-9} m^2/s, spanning the range of cases in Table 1. As shown in Figure 4a, the flow-through nanohole system provides maximum benefit at low τ values corresponding to fast reaction kinetics. As τ increases, binding kinetics become dominant and all response curves asymptotically approach the limit $t = \tau$.

Figure 4b provides a measure of the improvement achieved by employing the flow-through format. Specifically, the results are plotted in terms of an improvement factor, defined as the ratio of flow-over format to flow-through format response times. As shown, a benefit of 20-fold was achieved for small (rapidly diffusing) analytes with relatively fast binding kinetics ($\tau < 1$ s). As the binding time scale increases, the benefit decreases. These results indicate that a significant benefit (i.e., 2-fold improvement in response time) is achieved even for cases with binding time constants up to 10^3s. Many biosensor applications employ analytes with binding time constants in the range of 1−10^2 s.[17,39,42,43] In that range, flow-through nanohole array sensors can provide ~10- to 20-fold improvement in response. It is interesting to note that although the highest improvement ratios are achieved with small analytes (high diffusivity) with fast reaction kinetics, the benefits are eroded rapidly as the binding kinetics slow down. In contrast, larger analytes (low diffusivity) maintain significant benefits with slower binding kinetics, for example, $\mathscr{D} = 10^{-11}m^2/s$ maintains 5-fold improvement up to $\tau = 10^3$ s.

CONCLUSIONS

In this work, the analyte transport and time response of flow-through nanohole arrays was quantified and compared with that of a traditional flow-over sensor in a microchannel. The transport scaling analysis indicated that the flow-through sensor exhibits a Peclet number, Pe, 10^2-fold less than the flow-over format for the same given flow rate. For the case of rapid surface kinetics, the computational results indicated that, the flux of analyte molecules to the sensing surface of a flow-through nanohole array was much higher than the flow-over sensor (40-fold higher in the case of $Q = 10$ nL/min).

Finite binding kinetics, in general, have the effect of slowing down sensor response as compared to the purely transport limited case. Binding kinetics were included in the model, and the system response times were compared as a function of binding time constant and diffusion coefficient. A 20-fold faster time response, was achieved for the flow-through case with small (rapidly diffusing) analytes with relatively fast reaction kinetics. In the range applicable to most biosensing applications ($\tau = 1 - 10^3$s), and analytes with typical diffusion coefficients ($\mathscr{D} = 10^{-11}$ to 10^{-9} m^2/s), flow-through nanohole arrays offer ~10-fold benefit in terms of time response over established flow-over sensors formats.

ACKNOWLEDGMENT

We gratefully acknowledge the financial support of the Natural Sciences and Engineering Research Council of Canada, NSERC, through a scholarship to CE and research grant in partnership with the BC Cancer Agency Trev and Joyce Deeley Antibody Research Unit and Micralyne Inc. Funding from the Canada Research Chairs Program, the Canada Foundation for Innovation, and the British Columbia Knowledge Development Fund are also gratefully acknowledged.

SUPPORTING INFORMATION AVAILABLE

Additional information and figures. This material is available free of charge via the Internet at http://pubs.acs.org.

Received for review June 23, 2010. Accepted November 2, 2010.

AC101654F

(41) Sahu, A.; Soulika, A. M.; Morikis, D.; Spruce, L.; Moore, W. T.; Lambris, J. D. *J. Immunol.* **2000**, *165*, 2491–2499.

(42) Laffly, E.; Pelat, T.; Cédrone, F.; Blésa, S.; Bedouelle, H.; Thullier, P. *J. Mol. Biol.* **2008**, *378*, 1094–1103.

(43) Zhang, X. Y.; Young, M. A.; Lyandres, O.; Van Duyne, R. P. *J. Am. Chem. Soc.* **2005**, *127*, 4484–4489.

Appendix C

Optofluidic concentration: Photonic nanostructure as concentrator and sensor

Optofluidic concentration: Plasmonic nanostructure as concentrator and sensor

Carlos Escobedo[1], Alexandre G. Brolo[3], Reuven Gordon[2] and David Sinton[4,*]

[1] Department of Mechanical Engineering, University of Victoria, P.O. Box 3055, Victoria, BC, V8W 3P6, BC, Canada
[2] Department of Electrical and Computer Engineering, University of Victoria, P.O. Box 3055, Victoria, BC, V8W 3P6 Canada
[3] Department of Chemistry, University of Victoria, P.O. Box 3065, Victoria, BC, V8W 3V6, Canada
[4] Mechanical and Industrial Engineering, University of Toronto, 5 King's College Rd., Toronto, ON, M5S 3G8, Canada

*e-mail: sinton@mie.utoronto.ca

The early diagnosis of many diseases, such as cancers, requires rapid response from low analyte concentrations. The integration of fluidics and optics, as in flow-through nanohole arrays, has enabled increased transport of analytes to sensing surfaces. However, the limits of detection are fundamentally limited by local analyte concentration. Here, we employ the nanostructure geometry and the conducting nature of the film to actively concentrate analyte within the sensor. Analyte concentration is achieved through local electrohydrodynamics resulting from the applied field and pressure bias. We achieve 180-fold fluorescein enrichment and 100-fold enrichment and simultaneous sensing of a protein in less than 1 minute. This work presents the first demonstration of active concentration of analyte within a sensing nanostructure. This work presents opportunities for an order of magnitude increase in speed, and two orders of magnitude improvement in limit of detection for applications such early detection of cancers.

The marriage of fluidics and optics, or optofluidics, has enabled new functionality in several areas including analytical chemistry, biotechnology, and energy[1-4]. While arrays of nanoholes in metal films have been used for surface plasmon based sensing for several years[5], incorporating the nanoholes as fluidic nanochannels has resulted in improved sensor response[6]. The key benefit in that optofluidic approach is improved transport, and several studies have confirmed and extended the concept[7-11].

Despite the benefits of improved analyte transport and established optical sensitivity, applicability of optofluidic sensing systems is limited in many applications by low target analyte concentrations[12,13]. Specifically for the early detection of many diseases, such as ovarian cancer, biomarker concentrations remain low until late stages[14]. Current methods to concentrate analyte prior to sensing include field amplified stacking[15], isotachophoresis[16], electrokinetic trapping[17,18], conductivity gradient focusing[19], temperature gradient focusing[20] and field gradient focusing (FGF)[21]. FGF may be achieved in a microchannel using a floating internal electrode[22]; thus, there is an opportunity to apply this approach with metallic flow-through nanohole arrays. In traditional FGF, concentration results from a steep field gradient in a microchannel containing a buffer and a floating electrode[23,24]. The electrode disturbs the potential field, and the balance of local electrokinetic transport and bulk flow results in the local collection of charged species (e.g. buffer ions and charged analytes)[22]. The net concentration increase results from a combination of FGF, diffusion, bulk fluid transport, and secondary influences of induced-charge electrokinetics[25,26] (details provided in the Supplementary Information).

Here we present the first demonstration of a plasmonic nanostructure being used to locally concentrate analyte prior to sensing. The flow-through nanohole array sensor operates as a floating electrode when an electric potential is applied to the fluid. A combination of FGF and bulk pressure-driven flow bias concentrates analyte at the active sensing surface. This represents a straightforward experimental approach that enables the use of the plasmonic structure as both analyte concentrator and sensor.

Fig. 1 summarizes the optofluidic concentration approach. An array of through nanoholes is integrated within a microfluidic system. The fluid is a typical buffer with many small ions and larger electrically charged analytes (here, negatively charged). Concentrations are initially uniform throughout the system. The application of an electric field results in a bulk electroosmotic flow towards the cathode, and electrophoretic motion of cations and anions toward the cathode and anode, respectively. Small buffer anions have high electrophoretic velocities sufficient to counter the bulk flow everywhere except inside the metallic portion of each nanohole where the electric field strength is locally reduced ($t = t_{0+}$ in Fig. 1). This effect results in a local depletion of buffer anions, which grows towards the anode as the local conductivity reduces and the local electric field magnitude increases, typical of FGF[22]. The timescale for this buffer ion response is ~ 1 ms (details provided in the Supplementary Information). Larger charged analytes respond to the increased field and concentrate near the boundary of the depleted region ($t = t_1$ in Fig. 1). With the addition of a pressure bias ($t = t_2$ in Fig. 1) the position of the concentrated analyte plug is shifted down to the nanohole array surface and into the holes where it can be sensed at greatly elevated concentrations as compared to the initial sample.

We used arrays of 300-nm diameter through-holes with 450-nm periodicity fabricated in 100-nm-thick Si_3N_4 membranes coated with a 100-nm Au film (Methods). The arrays were integrated within a microfluidic system containing 1:1 (v:v) methanol/10 mM Tris-HCl solution (pH 8.1) seeded with model analyte, and electrodes (details of the set up provided in the Supplementary Information). The experiments included two model analytes: fluorescein, for quantifying the concentration effect, and bovine serum albumin (BSA) for concurrent analyte concentration and sensing.

Fig. 2 shows optofluidic concentration experimental results. For quantifying the concentration effect, a substrate with flow-through nanohole arrays was visualized from the Au side, as shown in Fig. 2a. Initially, the dilute tracer solution concentration (100 nM) was uniform throughout the whole system ($t = t_0$ in Fig. 2a). At $t = t_1 = 15$ s, a potential of 50 V is applied externally, and the concentration increases steadily as fresh analyte is transported to the arrays by the bulk pressure driven flow (4 kPa). As time progresses the charged dye is locally concentrated on the anodic side (visualized) surrounding the nanohole arrays and a depleted region is developed near the arrays (a movie of the experiment is available in the Supplementary Information). As shown in Figure 2c, the local enrichment process showed an approximately linearly increasing trend over time, reaching a concentration factor of ~ 180-fold in 60 s. This collection rate corresponds to the incoming flow rate of dye, indicating that the bulk of the model analyte is being concentrated on the gold, active sensing side.

The previous experimental setup was reoriented in order to visualize the process from the downstream cathodic compartment of the cell, as illustrated in Fig. 2d. A sequence of processed fluorescence images of the experiment is shown in Fig. 2e. With the application of the electric field, significant fluorescence in the nanoholes appears ($t = t_1 = 60$ s). Over the subsequent 60 s, ($t = t_2 = 120$ s), the local intensity at the arrays continues to increase. The four bright spots surrounding each nanohole are reflections from the silicon frame that supports the membrane and are simply artefacts from imaging the backside of the assembly. The surface plots corresponding to each image in Fig. 2e show the evolution of the local fluorescence signal collected from each nanohole array. The increasing localized signal and lack of fluorescein transport into the lower layer[6] indicate (1) the analyte concentration effect on the gold side and (2) the presence of concentrated analyte inside the nanoholes which absorb and emit in response to direct excitation from below. The plot in Fig. 2f shows the local fluorescence intensity as a function of time. An integration area of 30 x 30 pixels was selected over each array, and excluded the four reflection artefacts. Due to the intense confinement of the analyte within the holes, and further complexities of fluorescence imaging within and through the nanoholes, it is not possible to directly obtain concentration factors from this backside imaging configuration. However, several aspects of the plot in Fig. 2e are notable: (1) the signal increase occurs primarily after 40s, which corresponds approximately to the t_2 to t_3 period in Fig. 2e where the local concentration at the arrays increases significantly; (2) after 40 s, the observed intensity shows a linear increasing trend; (3) the rate of normalized intensity increase is on the same order as that observed in the gold-side chamber. Importantly, these collective results demonstrate active analyte concentration using a flow-through plasmonic nanostructure, a first for optofluidics.

The model sensing experiment involved electrohydrodynamic concentration and subsequent non-specific detection of BSA (with isoelectric point of 4.7 at room temperature[27]). Sensing was achieved by tracking the peak-shift of the light transmission spectrum at the resonant wavelength[5] (Methods). This experiment was designed to quantify and contrast the rate of biomolecular binding with and without the active concentration method developed here. Fig. 3a shows a schematic representation of BSA binding to the active surface of the nanohole arrays. The plot in Fig. 3b shows the experimental results using the analyte concentration scheme, at an applied electric potential of 50 V. The data for the control case (no field applied) is shown in Fig. 3b for the first 300 s and Fig. 3c for the subsequent 1500 s, followed by a final rising step at t=1600 s. The peak-shift indicates the binding of BSA to DSU on the sensing surface of the optofluidic nanostructure as time progresses. The peak-shift change over time shows the typical surface binding characteristic shape, reaching saturation of the sensing surface after ~ 120 s for the concentration experiment (with field) in Fig. 3a. The small blue-shift on the order of 1 nm after the rinse step confirms the formation of a BSA-DSU layer on the surface of the sensor. The magnitude of the peak-shift for the control case, shown in Fig. 3c, is small (~ 1.5 nm) and the time for reaching equilibrium is long (in the order of ~ 1000 s), in contrast to the shift obtained in the concentration scheme (shown in Fig. 3b). In combination, these results demonstrate that the concentration scheme developed here enabled a 10-fold decrease in binding time, and a 5-fold increase in peak shift. These differences correlate to the expected concentration-dependence of the binding kinetics[28]. In other words, the faster saturation and increased magnitude in peak-shift obtained with the analyte concentration scheme is consistent with the locally increased analyte concentration in the fluid resulting from the optofluidic concentration method.

To contextualize the sensing demonstration, we developed a computational model including transport and reaction kinetics but excluding the active concentration effect (further details in Supplementary Information). The binding of the model analyte, BSA, to DSU is non-specific and is described by simple first-order reaction kinetics[29]. The predicted response of the sensor (resonance peak-shift) was determined from the amount of analyte bound to the active surface in the simulations. In order to compare rates, the responses were normalized to the equilibrium value for the maximum concentration (10 μM). As shown in Fig. 3d, adsorption rates increase with increased concentration, as expected. As the response corresponds to the amount of analyte bound to the sensing surface, the response is smaller for the low concentrations, in agreement with the experimental results. The saturation time (vertical dashed line) for the experimental results with active concentration agrees most closely to the 10 μM bulk analyte concentration response curve (a concentration 100-fold that of the initial concentration). These results indicate that the optofluidic concentration scheme developed here enabled sensing of an analyte with response corresponding to a bulk concentration 100-fold greater than the solution employed.

We demonstrated active analyte concentration and sensing using a flow-through plasmonic nanostructure. Metallic flow-through nanohole arrays served as both floating electrodes and nanochannels that, under an externally applied voltage and a hydrostatic pressure bias, enabled the local concentration of analytes. We also demonstrate the concurrent use of the flow-through optofluidic nanostructure to concentrate a protein and to sense its binding to a functionalized Au nanohole surface. The results from this biosensing experiment, in combination with computational simulations, revealed analyte concentration of ~ 100-fold, compared to the control case with no concentrating effect. Collectively, these results demonstrate active analyte

concentration using a flow-through plasmonic nanostructure, a first for optofluidics. These results indicate that an order of magnitude increase in speed and two orders of magnitude improvement in limit of detection are feasible for applications such early detection of cancers.

Methods

Experimental system. A SEM image of a sample nanohole array is shown in Supplementary Fig. S1 (further details on the fabrication are provided in the Supplementary Information). A schematic of the experimental set-up is shown in Supplementary Fig. S2. The substrate for nanohole array fabrication consisted of single-window and multi-window free-standing TEM analysis Si_3N_4 membranes (Norcada, Edmonton, AB) with a thermally evaporated 100-nm-thick Au layer on a 5 nm thick Ti/W adhesion. The nanohole arrays were fabricated using focused-ion-beam (FIB). All the microfluidics were fabricated in poly(dimethylsiloxane) (PDMS) (Dow Corning, Midland, MI) using conventional soft-lithography. Device fabrication details are provided in the Supplementary Information. The integrated optofluidic system consisted of the Si_3N_4 membrane containing the nanohole arrays, a glass slide and the microfluidics as shown in Supplementary Fig. S1. Fluids were provided via PEEK tubing (Upchurch Scientific, Oak Harbor, WA). Pure Pt wire (Alfa Aesar, Ward Hill, MA) was used as electrodes. The power source was a Spellman SL30 (Spellman, Hauppauge, NY) and the applied voltage was controlled via LabVIEW (LabVIEW, Austin, TX). For the experiment presented in Fig. 2 an inverted epi-fluorescent microscope (DMI 6000B, Leica, NJ) and a CCD camera (Orca AG, Hamamatsu, NJ) with x10/0.3 NA and x20/0.4 NA objectives were used. For the experiments presented in Fig. 3, a miniature Ocean Optics USB2000 fiber-optic spectrometer (Ocean Optics, Dunedin, FL) for transmission spectra acquisition was used. For plasmon excitation, light from a halogen lamp was focused onto the nanohole arrays through a x20/0.4 NA objective.

Fluorescein concentration experiment. The optofluidic system was filled with 1:1 (v:v) methanol/10 mM Tris-HCl solution (pH 8.1) seeded with fluorescein (100 nM) prior to the experiment. Fluorescein enrichment quantification was achieved via image analysis and comparison against solutions with known fluorescein concentration (details provided in the Supplementary Information). The images in Fig. 2b were 16-bit in dynamic range and 138 by 522 pixels. Images acquired during the experiment presented in Fig. 2e were16-bit and 670 by 642 pixels. The images were processed using ImageJ software (open source, National Institutes of Health) and then imported into MATLAB (Mathworks, Natick, MA) for normalization and quantification.

BSA concentration and sensing experiment. Prior to the experiment, a DSU self-assembled monolayer (SAM) was immobilized onto the surface of the nanohole arrays and the system was rinsed and filled with 1:1 (v:v) methanol/10 mM Tris-HCl solution. Before applying the electric potential, the entire system was filled with a buffer solution containing 100 nM BSA. The time gap between solution replacement and voltage application was 30 s. Light transmission spectra were obtained using a miniature spectrometer (Ocean Optics, Dunedin, FL) and acquired using commercial software for processing. SPR transmission spectra were acquired every 10 seconds for 170 s. Finally, the system was rinsed with buffer in order to quantify the sensor response to adsorbed analyte, as separate from the bulk fluid. Spectra processing and peak-shift analysis were achieved using Ocean Optics spectral suite and MATLAB (MathWorks, Natick, MA) software.

References

1 Psaltis, D., Quake, S. R. & Yang, C. H. Developing optofluidic technology through the fusion of microfluidics and optics. *Nature* **442**, 381-386 (2006).
2 Shahi, S. Optofluidics: Air-tuned dye laser fits on a chip. *Nature Photon.* **4**, 269-269 (2010).
3 Cuennet, J. G., Vasdekis, A. E., De Sio, L. & PsaltisD. Optofluidic modulator based on peristaltic nematogen microflows. *Nature Photon.* **5**, 234-238 (2011).
4 Erickson, D., Sinton, D. & Psaltis, D. Optofluidics for Energy Applications. *Nature Photon.*, accepted (2011).
5 Anker, J. N. *et al.* Biosensing with plasmonic nanosensors. *Nature Mater.* **7**, 442-453 (2008).
6 Eftekhari, F. *et al.* Nanoholes As Nanochannels: Flow-through Plasmonic Sensing. *Anal. Chem.* **81**, 4308-4311 (2009).
7 Yanik, A. A. *et al.* An Optofluidic Nanoplasmonic Biosensor for Direct Detection of Live Viruses from Biological Media. *Nano Lett.* **10**, 4962-4969 (2010).
8 Ferreira, J. *et al.* Attomolar Protein Detection Using in-Hole Surface Plasmon Resonance. *J. Am. Chem. Soc.* **131**, 436-437 (2009).
9 Zhang, D. Y., Men, L. Q. & Chen, Q. Y. Microfabrication and Applications of Opto-Microfluidic Sensors. *Sensors* **11**, 5360-5382 (2011).
10 Guo, Y. B. *et al.* Optofluidic Fabry-Perot cavity biosensor with integrated flow-through micro-/nanochannels. *Appl. Phys. Lett.* **98** (2011).
11 Nanohole array show promise for simple detection of Ebola and Marburg viruses. *Nanomedicine* **6**, 12-12 (2011).
12 Wang, Y. C. & Han, J. Y. Pre-binding dynamic range and sensitivity enhancement for immuno-sensors using nanofluidic preconcentrator. *Lab Chip* **8**, 392-394 (2008).
13 Sinton, D., Gordon, R. & Brolo, A. G. Nanohole arrays in metal films as optofluidic elements: progress and potential. *Microfluid. Nanofluid.* **4**, 107-116 (2008).
14 Buchen, L. MISSING THE MARK. *Nature* **471**, 428-432 (2011).
15 Sustarich, J. M., Storey, B. D. & Pennathur, S. Field-amplified sample stacking and focusing in nanofluidic channels. *Phys. Fluids* **22** (2010).
16 Jung, B., Bharadwaj, R. & Santiago, J. G. On-chip millionfold sample stacking using transient isotachophoresis. *Anal. Chem.* **78**, 2319-2327 (2006).
17 Wang, Y. C., Stevens, A. L. & Han, J. Y. Million-fold preconcentration of proteins and peptides by nanofluidic filter. *Anal. Chem.* **77**, 4293-4299 (2005).
18 Kim, S. J. & Han, J. Y. Self-sealed vertical polymeric nanoporous-junctions for high-throughput nanofluidic applications. *Anal. Chem.* **80**, 3507-3511 (2008).
19 Shackman, J. G. & Ross, D. Counter-flow gradient electrofocusing. *Electrophoresis* **28**, 556-571 (2007).
20 Ross, D. & Locascio, L. E. Microfluidic temperature gradient focusing. *Anal. Chem.* **74**, 2556-2564 (2002).
21 Koegler, W. S. & Ivory, C. F. Field gradient focusing: A novel method for protein separation. *Biotechnol. Prog.* **12**, 822-836 (1996).
22 Hlushkou, D. *et al.* Electric field gradient focusing in microchannels with embedded bipolar electrode. *Lab Chip* **9**, 1903-1913 (2009).
23 Dhopeshwarkar, R. *et al.* Electrokinetics in microfluidic channels containing a floating electrode. *J. Am. Chem. Soc.* **130**, 10480-+ (2008).

24 Piruska, A. *et al.* Electrokinetically driven fluidic transport in integrated three-dimensional microfluidic devices incorporating gold-coated nanocapillary array membranes. *Lab Chip* **8**, 1625-1631 (2008).
25 Bazant, M. Z. & Squires, T. M. Induced-charge electrokinetic phenomena: Theory and microfluidic applications. *Phys. Rev. Lett.* **92** (2004).
26 Gamayunov, N. I., Mantrov, G. I. & Murtsovkin, V. A. Study of flows induced in the vicinity of conducting particles by an external electric-field. *Colloid J. USSR* **54**, 20-23 (1992).
27 Böhme, U. & Scheler, U. Effective charge of bovine serum albumin determined by electrophoresis NMR. *Chem. Phys. Lett.* **435**, 342-345 (2007).
28 Squires, T. M., Messinger, R. J. & Manalis, S. R. Making it stick: convection, reaction and diffusion in surface-based biosensors. *Nature Biotech.* **26**, 417-426 (2008).
29 Gervais, T. & Jensen, K. F. Mass transport and surface reactions in microfluidic systems. *Chem. Eng. Sci.* **61**, 1102-1121 (2006).

Acknowledgements

The authors gratefully acknowledge the financial support to the Natural Sciences and Engineering Research Council of Canada, NSERC, through a scholarship to CE and research grant in partnership with the BC Cancer Agency Trev and Joyce Deeley Antibody Research Unit and Micralyne Inc. Funding from the Canada Research Chairs Program, the Canada Foundation for Innovation, and the British Columbia Knowledge Development Fund are also gratefully acknowledged.

Contributions

C.E. was the primary researcher on this project, developing and building the set-up, carrying out all experiments, simulations and analysis. DS and CE proposed the overall project. A.B. and R.G. provided essential contributions and guidance throughout the project. All authors discussed the results and assisted in the preparation of the manuscript.

Competing financial interests

The authors declare no competing financial interests.

Figures

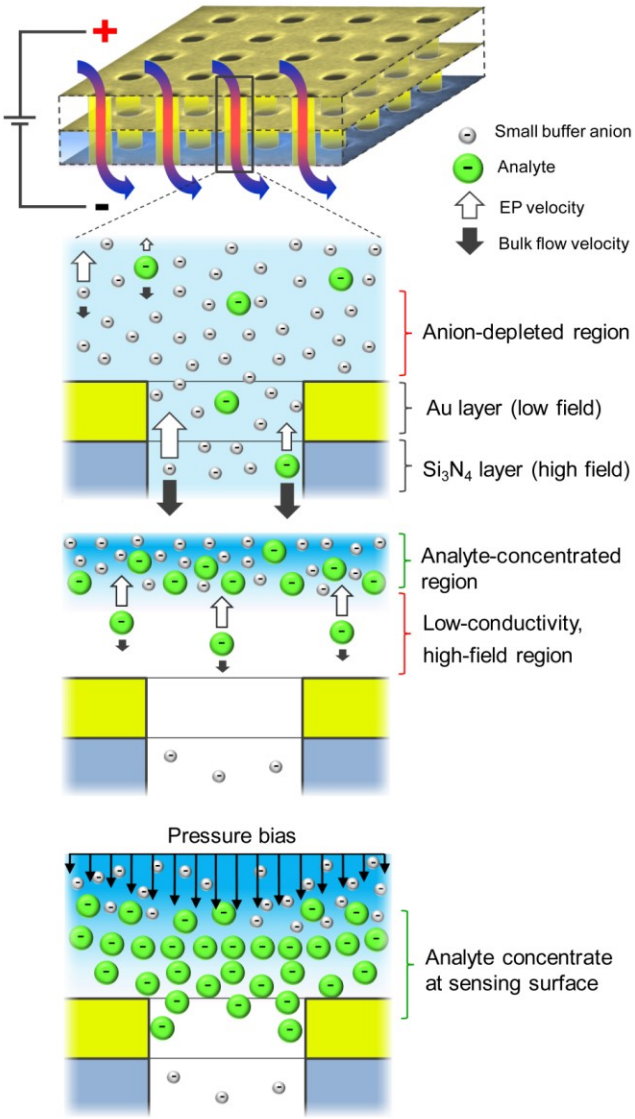

Figure 1 Optofluidic concentration approach. A through nanohole array is embedded in a microfluidic environment containing analyte in buffer (not to scale). Concentrations are initially uniform throughout the entire system. **a**, Under an applied electric field, all electrically charged species in the fluid experience electrokinetic forces. Electroosmotic and pressure-driven flow result in a net bulk flow towards the cathode. Small buffer anions from the background solution are transported in opposite direction to the bulk flow, which results in an anion-depleted region next to the Au layer of the nanohole array. The nearly-null electric field inside the gold region of the nanoholes results in a nearly zero-electrokinetic

transport zone, where species are only transported by the bulk flow. **b**, In absence of a pressure-driven bias from the anode side, larger charged analytes respond to the increased field and concentrate near the boundary of the depleted region. **c**, With the addition of a pressure bias, the concentrated analyte plug is shifted down to the nanohole array and into the holes where it can be sensed at greatly elevated concentrations as compared to the initial sample.

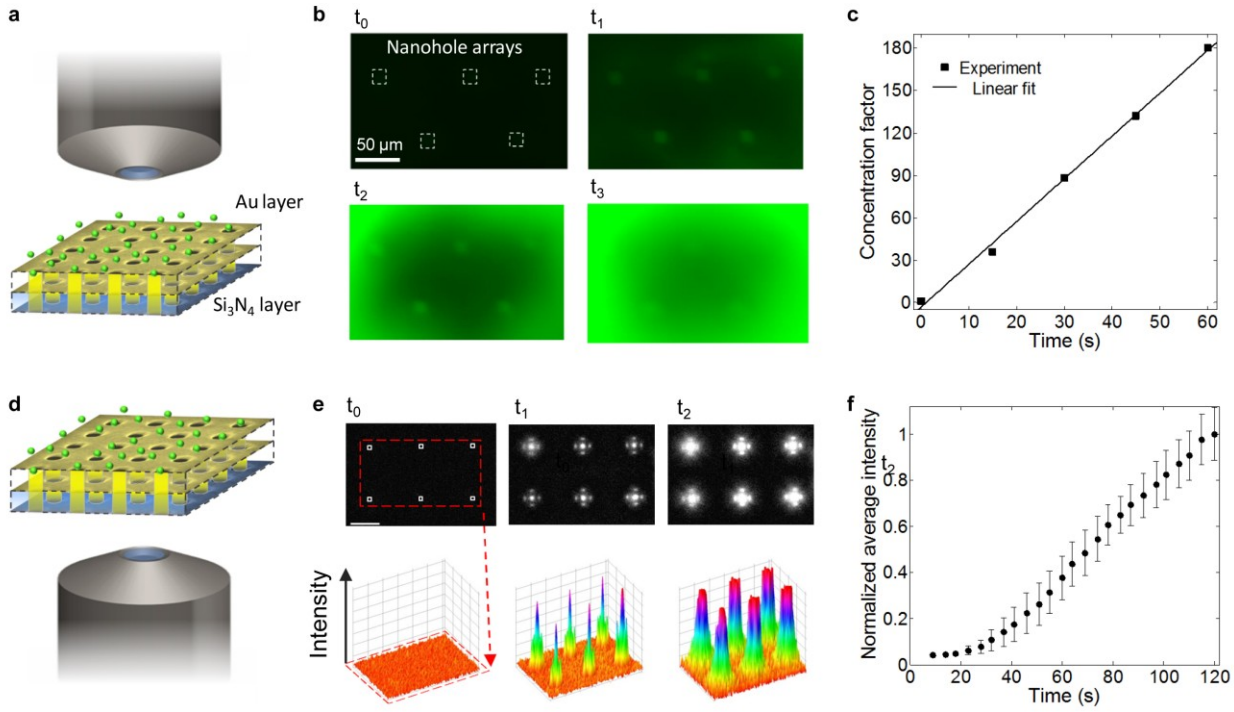

Figure 2 Optofluidic concentration of fluorescein. a, Simplified illustration of the visualization configuration during the fluorescein concentration experiment. **b** Image sequence during the fluorescein concentration process under an electric potential of 50 V and a hydrostatic pressure of 4 kPa (4 images at 15 s intervals) in a single-window gold-on-silicon membrane with five nanohole arrays. **c**, Peak concentration enhancement plot over time measured in the top-left array. **d** Simplified illustration of the configuration for the observation of the concentration process from the Si_3N_4 side. The substrate consisted of 6 gold-on-silicon-nitride membranes with a nanohole array in each window. The initial fluorescein concentration, array geometries and applied voltage and pressure were the same as those in Fig. 2b. **e** Image sequence showing the progress of fluorescein concentration at the Au side of the

nanohole arrays. The image at $t = t_0$ shows the system before the application of the voltage. At $t = t_1 = 60$ s, significant fluorescence in the nanoholes emerges. Over the subsequent 60 s, the local intensity at the arrays continues to increase. Surface plots corresponding to each image show the evolution of the local fluorescence signal collected from each nanohole array. **f** Plot of the local fluorescence intensity as a function of time. An integration area of 30 x 30 pixels was selected over each array, and excluded the four reflection artefacts from the silicon window. The vertical bars indicate the standard deviation.

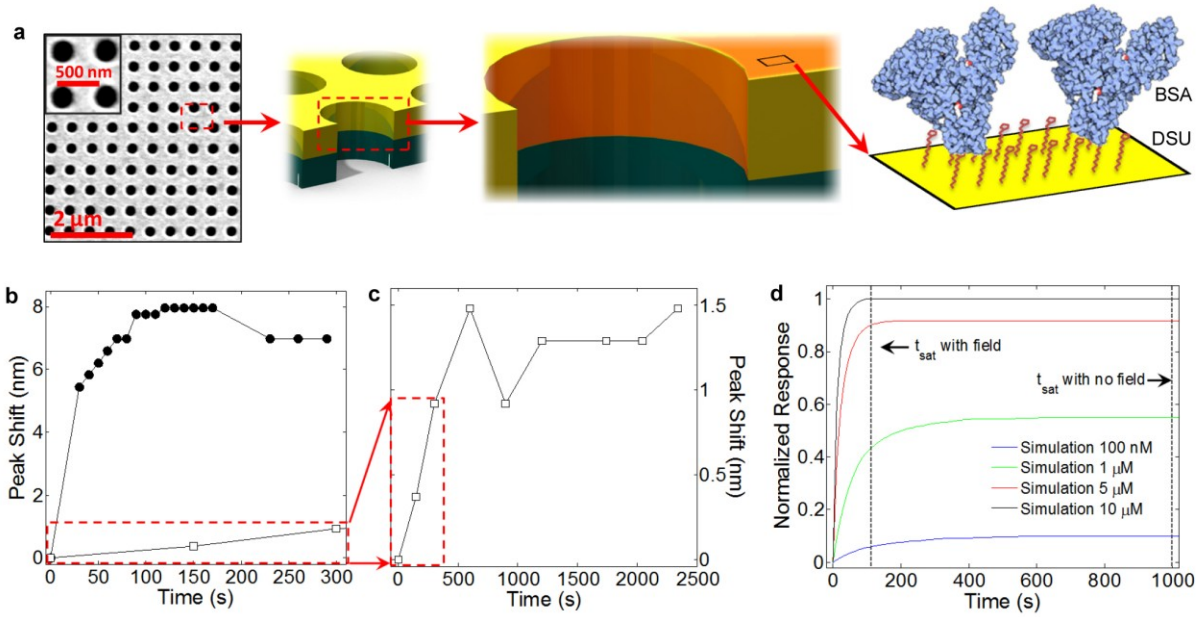

Figure 3 SPR sensing. **a**, Illustration of BSA binding on the functionalized active surface of the optofluidic sensor. **b**, Resonance peak-shift monitoring of BSA binding to DSU under both concentration (50 V, 4 kPa) and control conditions (no applied field). Using the concentration format (applied field), the peak-shift reached a plateau after ~120 s. The plot for the control experiment (no applied field) shows a slower binding rate, without reaching saturation within the time range shown in this figure. **c**, Resonance peak-shift monitoring of BSA binding to DSU under control conditions (no applied field). The time required to reach equilibrium was 10-fold compared to the concentration scheme, and the magnitude of the shift was 5-fold smaller in magnitude. **d**, Simulated detection of non-specific BSA binding to DSU. A computational model was used to simulate the response time of the sensor at different BSA concentrations. The saturation times, t_{sat}, from both the concentration and control experiments are shown

as vertical dashed lines. The saturation time with concentration agrees most closely to the 10 μM bulk analyte simulation curve. This indicates that the optofluidic concentration scheme developed here enabled sensing of an analyte with response corresponding to a bulk concentration 100-fold increased concentration.

Supplementary Information

Optofluidic concentration: Plasmonic nanostructure as concentrator and sensor

Carlos Escobedo[1], Alexandre G. Brolo[3], Reuven Gordon[2] and David Sinton[4]*

[1] Mechanical Engineering, University of Victoria, Victoria, BC, Canada
[2] Electrical and Computer Engineering, University of Victoria, Victoria, BC, Canada
[3] Chemistry, University of Victoria, Victoria, BC, Canada
[4] Department of Mechanical and Industrial Engineering, University of Toronto, 5 King's College Rd., Toronto, ON, M5S 3G8, Canada

*e-mail: sinton@mie.utoronto.ca

Flow-Through Nanohole Array Fabrication

Square arrays of circular nanoholes were fabricated using focused-ion beam (FIB) lithography. Single-window and multi-window free-standing Si_3N_4 membranes (Norcada, Edmonton, AB) with a thermally evaporated 100 nm thick Au layer on a 5 nm thick Ti/W adhesion layer were used as substrate. The energy and current milling beam parameters were 30 keV and 50 pA respectively. The typical beam spot size was ~ 10 nm and the dwell time was set to 2 ms. The milled arrays consisted of 15 × 15 holes with 260 nm in diameter and a periodicity of 450 nm. The nanohole arrays were inspected using SEM imaging from both sides after the fabrication process as shown in Fig. S1. The fastest nanohole array milling rate achieved during the fabrication of the sensors used for the work presented here was 40 minutes for individually milled nanoholes and 12 minutes for arrays milled using a mask. This fabrication procedure does not require intermediate fabrication steps, such as polymer deposition or chemical etching, which may result in increased fabrication times.

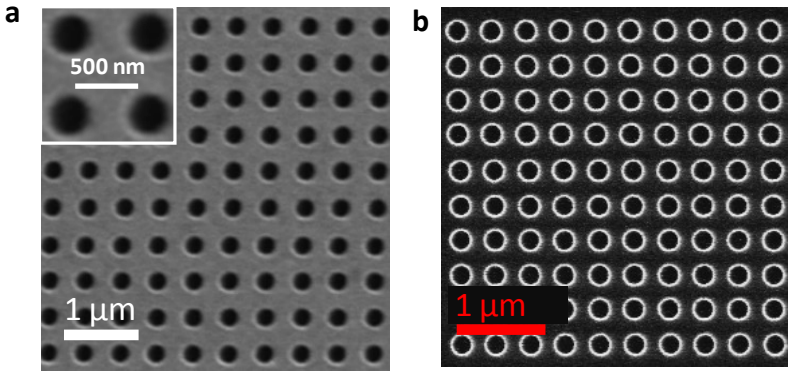

Figure S1 Nanohole arrays fabricated in a Au-on-Si_3N_4. a, Picture from the Si_3N_4 side and **b**, picture from the Au side.

Experimental set-up fabrication and integration

Two identical microfluidic chips and a spacer were fabricated in poly(dimethylsiloxane) (PDMS) using conventional soft-lithography[1]. The chip consisted of a single channel with 250 µm by 70 µm cross sectional area and 10 mm in length. The channel had a 1-mm-diameter central chamber. The spacer consisted of a flat PDMS layer of ~ 1 mm in thickness with a central opening of ~ 5 mm in diameter. A hole was milled through a commercial glass slide with a rotary tool using solid carbide milling cutter. The gold-on-nitride substrate containing the nanohole array was aligned and fixed onto the glass slide using NOA 68 optical adhesive (Norland, Cranbury, NJ). The PDMS layers were then bonded to the glass slide containing the nanohole arrays substrate via oxygen plasma. Pure Pt wires (Alfa Aesar, Ward Hill, MA) embedded in the PDMS chip served as electrodes. The electric potential was applied via a Spellman SL30 high voltage power supply (Spellman, Hauppauge, NY) with LabVIEW and a NI-USB-6212 data acquisition system (National Instruments, Austin, TX). The potential was applied to platinum wire electrodes inserted into the top and bottom microfluidic layers.

Fluids were provided to the chip by hydrostatic means by external reservoirs connected to the microfluidic chip via PEEK tubing (Upchurch Scientific, Oak Harbor, WA). The outlet of top microfluidic chip and the inlet of the bottom microfluidic chip were blocked under flow-through operation using low-pressure PEEK shut-off valves (Upchurch Scientific, Oak Harbor, WA). Fig. S2 shows a schematic representation of the experimental setup and the chip assembly and

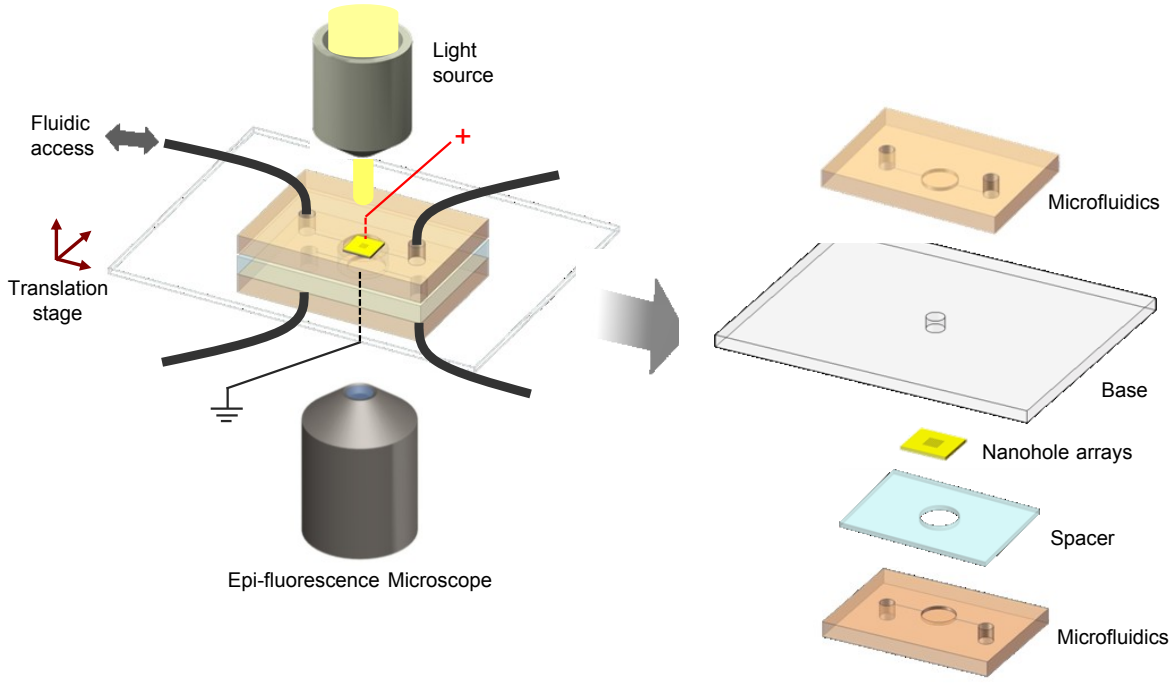

Figure S2 Schematic of the experimental set up used in the fluorescein optofluidic concentration experiments. The optofluidic system consisted of PDMS microfluidic components and a free-standing Au-on-Si_3N_4 membrane milled with the nanohole arrays fixed on a glass slide with a central opening. For fluorescence imaging experiments, the assembled optofluidic system was placed on the stage of an inverted epi-fluorescence microscope and a CCD camera was used for image acquisition. The optofluidic concentration process was visualized from both sides of the nanohole array in two different experiments.

Chemicals and solutions preparation

Trizma base (Sigma-Aldrich), hydrochloric acid (HCl) (Fisher Scientific), ethanol anhydrous (Sigma-Aldrich) and deionized water from a Milli-Q Gradient system (Millipore, Billerica, MA) were used for ethanol/buffer solution preparation. Alexa Fluor 488 dye was purchased from Invitrogen, dithiobis(succinimidyl undecanoate) (DSU, 92.7%) from Dojindo Laboratories and bovine serum albumin (BSA) from Sigma-Aldrich. A pH5 Acorn series pH meter (Oakton Instruments, Vernon Hills, IL) were used for measuring the conductivity and the pH. The buffer had a pH of 8.1.

Fluorescein concentration quantification experiment

Imaging was achieved using an inverted epi-fluorescent microscope (DMI 6000B, Leica, NJ) with $\times 10/0.3$ NA and $\times 20/0.4$ NA objectives, and CCD camera (Orca-AG, Hamamatsu, NJ). The acquired images were 738 by 522 pixels and were saved in several formats for visualization and processing, including RGB and 16-bit dynamic range. For concentration quantification, all the images were 16-bit. The images were processed using ImageJ and then imported into Matlab (Mathworks, Natick, MA) for quantification. Maximum concentration factors were achieved by comparison of the intensity of the enriched plug in the vicinity of the nanohole arrays against the intensities of standard concentrations. This methodology has been used by several groups for analyte enrichment assessment in microfluidics[2-4]. Fig. S3a shows a schematic of the microfluidic chip used for acquiring the standard fluorescence intensities. Fig. S3b shows fluorescence pictures taken at the center portion of the microchannels of the chip. The standard fluorescein concentrations used in the analysis were 100 nM, 1 μM, 10 μM. The images were acquired at 510 ms of exposure and a gain of 83.

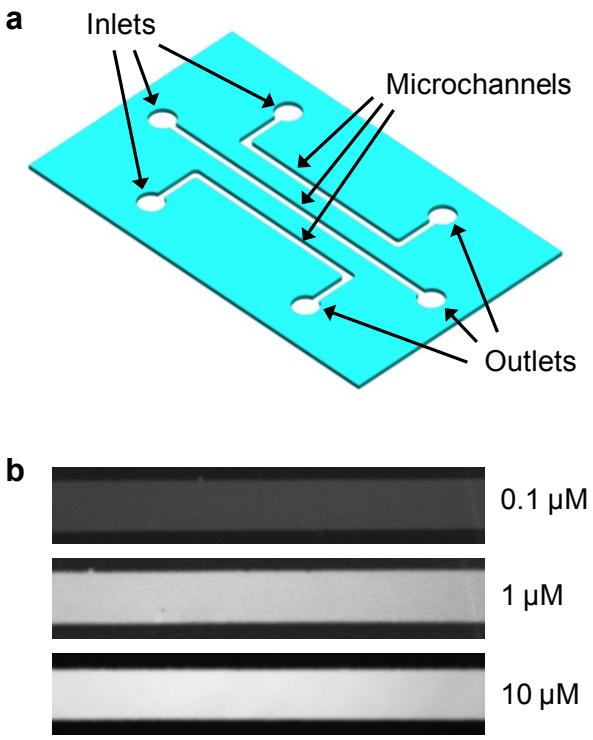

Figure S3 Fluorescence standard curve. a) Schematic representation of the microfluidic chip used for fluorescence standard intensities quantification. b) Fluorescence picture of the center portion of the channels at different fluorescein concentrations.

The quantification of the fluorescein concentration factors in the concept validation experiment was achieved by comparison against solutions of known fluorescein concentration as shown in Fig. S4.

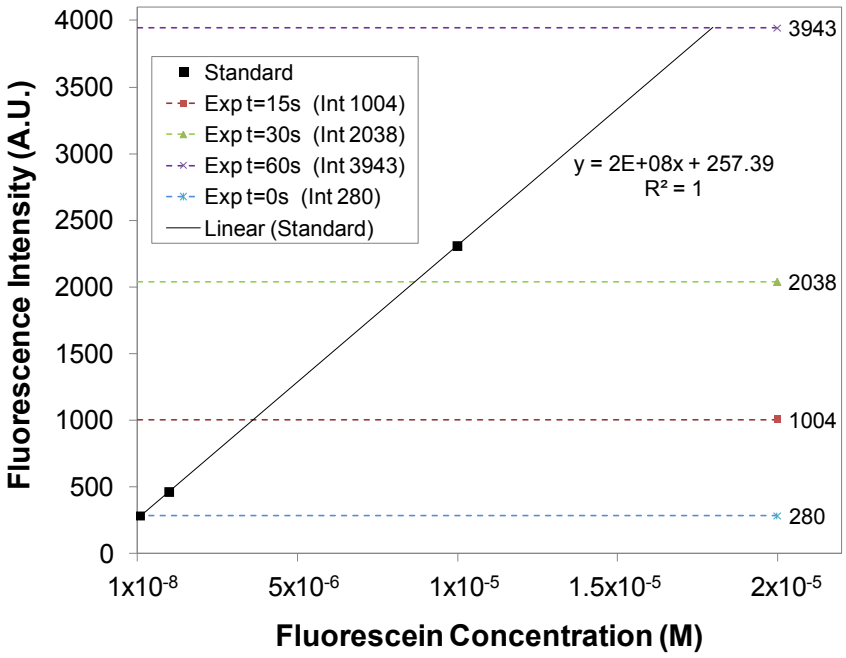

Figure S4 Plot of fluorescence intensity in the concentration calibration experiment. Fluorescein concentration was quantified by comparing the actual intensity from experimental images with intensities of known concentrations at same experimental conditions.

The videos (provided in the additional Supplementary Information) were generated using RGB images from the same experimental image sequence as that used for fluorescein concentration quantification.

Sensing experiment

Fig. S5 shows a schematic representation of the experimental set-up used in the sensing experiment. A custom-built halogen lamp with power control was used as light source at normal incidence. The light was focused onto a nanohole array through a $\times 20/0.4$ NA microscope

objective (Leica, NJ). Transmitted light spectra were acquired using a miniature USB2000 fiber-optic spectrometer (Ocean Optics, Dunedin, FL).

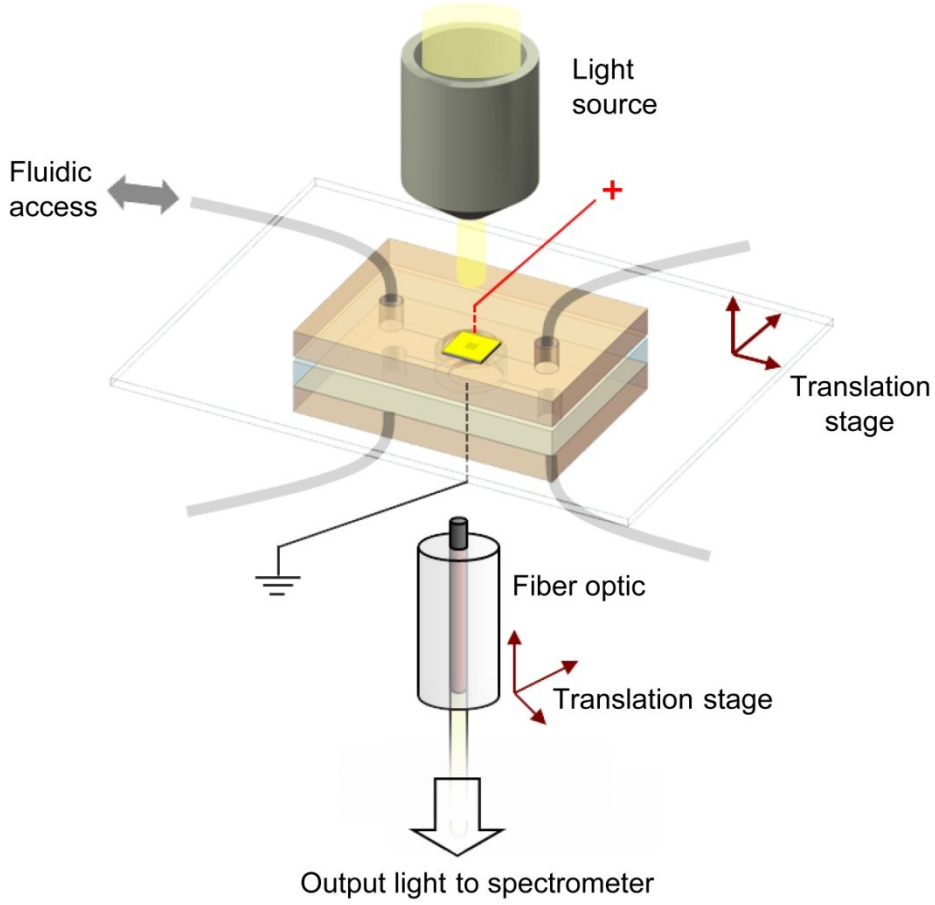

Figure S5 Schematic of the experimental set-up used to monitor BSA binding on a DSU SAM.

For spectra acquisition, the integration time was set to 100 ms and a spectral average of 10 was used. The transmission spectra were saved as text and resonance peak-shift quantification was achieved using a Matlab code. Fig. S6 shows the peaks of the processed spectra with normalized transmission intensity at 0 s, 40 s and 110 s of the sensing experiment.

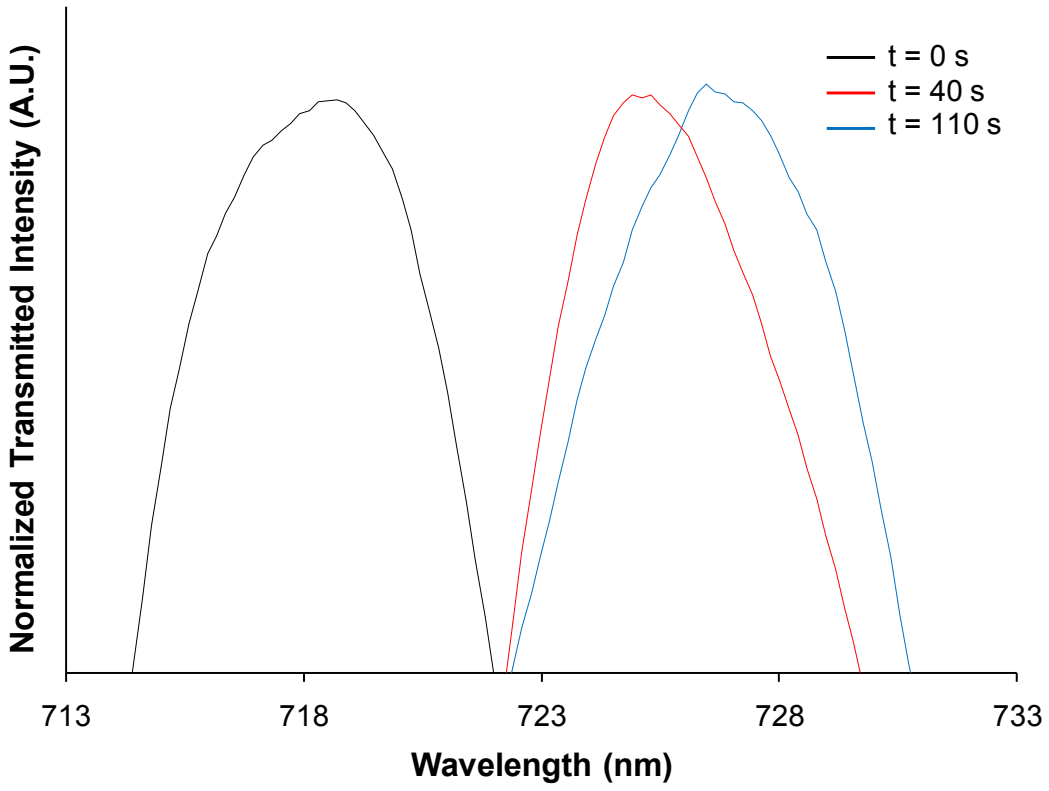

Figure S6 Processed normalized spectra peaks from the sensing experiments.

BSA binding kinetics simulations

The model, shown in Fig. S7a, involves a two-dimensional unidirectional pressure-driven flow through a single nanohole with reactive sidewalls which corresponded to the active sensing area of the nanoholes. The nanohole had 300 nm in diameter and 200 nm in depth which represented the 100-nm-thick layers of Au and Si_3N_4. The mesh of the model was refined at the walls as shown in Fig. S7b.

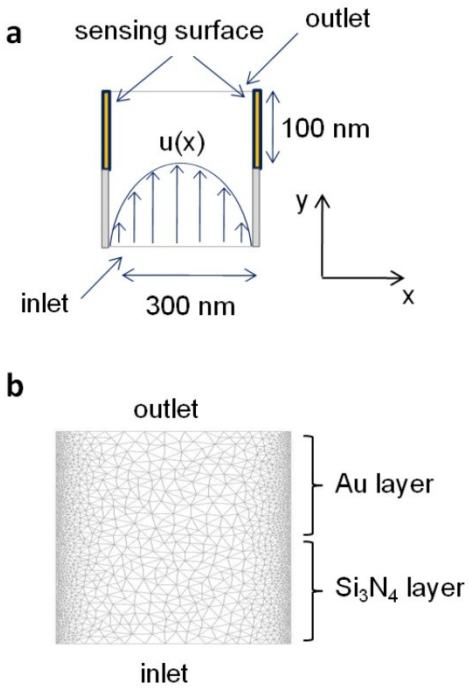

Figure S7 a) Model used in the simulations. b) Detail of the mesh used for the simulations.

The rate of species adsorption at the Au layer is given by the established first-order kinetics Langmuir kinetics[5] which can be described by the following expression:

$$\frac{\partial c_S}{\partial t} = D_S \nabla^2 c_S + k_{on} c_0 (b - c_S) - k_{off} c_S \qquad \text{S1}$$

where D_S is the diffusion coefficient of antigen-antibody complexes at the surface, c_0 is the bulk concentration, k_{on} is the adsorption constant, k_{off} is the desorption constant and b is the total surface concentration of active potential binding sites. The surface concentration of adsorbed species is:

$$c_S = \frac{b c_0 k_{off}}{k_{on} c_0 + k_{off}} \left(1 - e^{-(c_0 k_{on} + k_{off})t}\right) \qquad \text{S2}$$

and the surface concentration of adsorbed species at equilibrium is:

$$c_S^{eq} = \frac{bc_0 k_{off}}{k_{on} c_0 + k_{off}} \quad \text{S3}$$

and the time scale required for the sensor to equilibrate at this concentration is:

$$\tau = (c_0 k_{on} + k_{off})^{-1} \quad \text{S4}$$

which, in terms of nanohole array based sensing, is the time required to achieve the maximum signal change (i.e. peak-shift) from the transmission spectrum [7].

The advection and diffusion of species in the bulk is dictated by:

$$\frac{\partial c}{\partial t} = D\nabla^2 c - \vec{u} \cdot \nabla c \quad \text{S5}$$

The boundary conditions used in the model are summarized in Table S1.

Table S1

Inlet	$c = c_0$
Outlet	$n \cdot (cu - D\nabla c) = n \cdot cu$
Au layer	$n \cdot (cu - D_s \nabla c_s) = -k_{on} c(\theta_0 - c_s) + k_{off} c_s$
Si_3N_4 layer	$n \cdot (cu - D\nabla c) = 0$

Additional Induced Charge Double Layer Effect

The concentration effect is enabled by small ion electrophoretic migration that scales with the axial component of applied field, E, as $\mu_{EP}E$, where μ_{EP} is the electrophoretic mobility, and which is inversely proportional to ion diffusivity, D.[6] The initial ion-depleted region over the

gold layer of the nanoholes develops over an axial length l in a time scale ~ $\mu_{EP}E/l$. For typical small anions with $D \sim 10^{-9}$ m^2/s, under an initial electrical field strength on the order of 10^3 V/m, an anion-depleted region of 1 μm develops in ~ 1 ms. Thus the initial depletion layer is formed effectively instantaneously in the context of typical sensing applications, and the subsequent collection of analyte occurs on a timescale dependent on the incoming flow.

A floating electrode in an electrolyte-filled channel with an applied electric field presents an array of interconnected phenomena. In addition to the electric field gradient focusing effect that is dominant in this work, other effects are also present. Specifically, due to the conductive nature of the inner surface of the nanoholes, an induced charge double layer (ICDL) is formed when an electric potential is applied to the system[7]. The metallic surface of the nanoholes acts in bipolar mode, and thus one part of the surface experiences the accumulation of cations while anions cover the rest. The development of the IDCL can be conceived as a first-order energy storage system, in analogy to a resistor-capacitor electric circuit, in which the product RC provides the characteristic charging timescale τ[7,8]. In the case of the ICDL in the nanoholes, this timescale has an order of magnitude of ~ $\lambda_D l_n/D$, where λ_D is the Debye length, l_n is the length depth of a nanohole and D is the ionic diffusivity [7,9]. For the conditions utilized in the experiments reported here, λ_D is ~ 10 nm and D is in the order of 10^{-9} m^2/s, resulting in a characteristic time in the order of 1 μs. This means that the ICDL develops instantaneously compared to the transport events relevant to this work (in the order of seconds). The development of the ICDL results in two counter-rotating symmetric induced-charge electroosmotic (ICEO) flows above the metallic surface. The slip velocity generated by the ICEO flows may counteract the bulk flow at the entrance of the metallic region of the nanohole with a magnitude of $\sim \varepsilon E_0^2 l_n / \eta$ [7] which, for the conditions of this experiment, corresponds to ~ 5% of

the bulk EOF. In summary, while the ICEO effect is present as described above, the effect is relatively small relative to the other transport mechanisms described in the main text.

References

1 Duffy, D., McDonald, J., Schueller, O. & Whitesides, G. Rapid prototyping of microfluidic systems in poly (dimethyl siloxane). *Anal. Chem.* **70**, 4974 (1998).

2 Wang, Y. C., Stevens, A. L. & Han, J. Y. Million-fold preconcentration of proteins and peptides by nanofluidic filter. *Anal. Chem.* **77**, 4293-4299 (2005).

3 Kim, S. J. & Han, J. Y. Self-sealed vertical polymeric nanoporous-junctions for high-throughput nanofluidic applications. *Anal. Chem.* **80**, 3507-3511 (2008).

4 Jung, B., Bharadwaj, R. & Santiago, J. G. On-chip millionfold sample stacking using transient isotachophoresis. *Anal. Chem.* **78**, 2319-2327 (2006).

5 Goodrich, J. A. & Kugel, J. F. (Cold Spring Harbor Laboratory Press, N.Y., 2007).

6 Probstein, R. F. *Physicochemical Hydrodynamics*. Second edn, 399 (John Wiley & Sons Inc., 2003).

7 Squires, T. M. Induced-charge electrokinetics: fundamental challenges and opportunities. *Lab on a Chip* **9**, 2477-2483 (2009).

8 Squires, T. M. & Quake, S. R. Microfluidics: Fluid physics at the nanoliter scale. *Rev. Mod. Phys.* **77**, 977-1026 (2005).

9 Simonov, I. N. & Shilov, V. N. Theory of low frequency dielectric-dispersion of a suspension of ideally polarizable spherical-particles. *Colloid Journal of the USSR* **39**, 775-780 (1977).

Appendix D

Integrated Nanohole Array Surface Plasmon Resonance Sensing Device using a Dual-Wavelength Source

Submitted to Journal of Micromechanics and Microengineering

Integrated Nanohole Array Surface Plasmon Resonance Sensing Device using a Dual-Wavelength Source

C Escobedo[1], S Vincent[2], A I K Choudhury[2], J Campbell[2], A G Brolo[3], D Sinton[1*] and R Gordon[2*]

[1]Department of Mechanical Engineering, University of Victoria, V8W 3P6, Victoria, BC, Canada
[2]Department of Electrical and Computer Engineering, University of Victoria, P.O. Box 3055, V8P 5C2, Victoria, BC, Canada
[3]Department of Chemistry, University of Victoria, V8W 3V6, Victoria, BC, Canada

[*] E-mail: dsinton@uvic.ca, gordon@uvic.ca

Abstract
In this paper, we demonstrate a compact integrated nanohole array-based surface plasmon resonance sensing device. The unit includes a LED light source, driving circuitry, CCD detector, microfluidic network, and computer interface, all assembled from readily available commercial components. A dual-wavelength LED scheme was implemented to increase spectral diversity and isolate intensity variations to be expected in the field. The prototype shows bulk sensitivity of 266 pixel intensity units/RIU and a limit of detection of 6 x 10^{-4} RIU. Surface binding tests were performed, demonstrating functionality as a surface based sensing system. This work is particularly relevant for low-cost point-of-care applications, especially those involving multiple tests and field studies. While nanohole arrays have been applied to many sensing applications, and their suitability to device integration is well established, this is the first demonstration of a fully-integrated nanohole array based sensing device.

1. Introduction

Common surface plasmon resonance (SPR) technologies currently used in biomedical applications rely on different coupling techniques including the Kretschmann configuration, and grating and waveguide couplers [1-3]. Specifically, the Kretschmann arrangement offers a high sensitivity, with a bulk detection limit on the order of 10^{-7} refractive index units or RIU [2, 3]. Assorted metal nanostructures that support surface plasmon excitations include nanoparticles [4] and nanoholes in metal films [5], the latter of which was found to exhibit extraordinary optical transmission (EOT) [6]. EOT resonances specifically depend on the refractive index near the surface, which has motivated the use of nanohole arrays as biosensors [8]. It was recognized early on that the collinear optical geometry of nanohole arrays is convenient for integration, further offering the potential for a high degree of multiplexing within a microfluidic environment [7]. The on-chip implementation of nanohole arrays involved a gold-on-glass substrate with arrays of nanoholes and a polydimethylsiloxane (PDMS) microfluidic layer reversibly bonded to the top [9]. The first nanohole array based sensing demonstrations achieved smaller output sensitivities compared to the aforementioned Kretschmann configuration [10], and presently continue to be lower than the best Kretschmann sensors. Several approaches have been proposed in order to improve nanohole array based SPR sensitivity, including devising analytical methodologies that increase the response to binding events

at the surface [11-15]. An example of this is the application of sandwich assays in SPR [16]. Furthermore, the fabrication of nanoholes generally involves nanofabrication methods; therefore introducing complexity and cost with respect to the Kretschmann SPR which requires a single thin metal film. However, these complexities have been reduced by advances in top-down methods (e.g., optical lithography [17, 18] and nanoimprint lithography [19]) and bottom-up methods (e.g., nanosphere lithography [20] and colloidal templating techniques [18, 21]). It has been shown that surface sensing from nanohole arrays produces up to 1192 nm/RIU shift in the extraordinary optical transmission peak [3, 5, 7, 19-24].

An alternative to wavelength-shift detection in biosensing applications is to monitor the extent of adsorption by measuring the intensity variations from transmitted monochromatic beams [28]. This has the benefit of simplifying the detection scheme (i.e., removing the need for a spectrometer), but reduces the spectral diversity of the detected signal. Consequently, the changes in light intensity used in this approach are often susceptible to spurious effects, such as drift in the sources or detectors and bulk matrix scattering as well as absorption [29]. In order to eliminate spurious effects associated with a single source at a particular wavelength, a second source at a different wavelength, responding in the opposite manner to the first source may be added. In particular, if the intensity of the first source decreases to indicate a sensing event, this can be isolated from mere absorption or scattering of the light because the intensity of the second source should increase.

In this work, we demonstrate a hand-held integrated nanohole array-based sensing device with nine sensor elements, which is applicable to multiplexed detection [30]. This implementation is a significant step towards the use of SPR sensing technology for point-of-care and field testing applications. The device is based on nanohole array sensing, where the transmission spectrum of the nanohole array is modified by the local refractive index close to the metal surface. The device is tested through both bulk refractive index sensing and surface adsorption sensing experiments.

2. Experimental

2.1. Overview of the Integrated Sensing Platform

Figure 1 shows an image of the prototype device used in the experiments and schematic detailing the main components. A Videology 20K135USB board camera (generic industrial OEM CCD camera) with 1/4 inch format 720 × 480 pixel IL CCD and 8-bit ADC acted as the sensor array. LEDs with broad incoherent illumination as well as simple biasing circuitry were used as the light source. The LED was controlled by a driver circuit which in turn were controlled via MATLAB (Mathworks, MA). A chip assembly enclosed the substrate with the nanohole array sensors and a microfluidic chip responsible for interfacing the gold surface with selected test solutions. Microfluidic solution delivery was achieved by means of a microscrew syringe pump (Harvard Apparatus, MA) via 1/16 inch outer diameter tubing (IDEX Health & Science LLC, Oak Harbor, WA). The chip assembly was clamped together using a customized metal frame with front and back openings for optical access and was mounted on a three-degrees-of-freedom positioning stage. Both the CCD camera and the circuitry containing the LEDs were positioned orthogonally with respect of the chip assembly as shown in Figure 1b. The CCD camera was configured to image the arrays directly by adjusting the lens provided. The light source control as well as the image acquisition were achieved by a separate computer via MATLAB. In order to partition the image into regions relevant to the individual nanohole arrays, nine 5x5 pixel grids were formed based on the location of the top left pixel of each array's image. Signal responses for all 9 nanohole arrays were simultaneously displayed in real-time, as an averaged pixel intensity (calculated through sampling 25 geometric points, whose result was temporally sampled at a rate of approximately 12 Hz) was displayed for both the red and green LEDs. The integrated sampling period was 10 s per LED wavelength. A metal

housing (not illustrated) was utilized to reduce electromagnetic interference and effect of external light signals. Details of the fabrication and assembly of the individual components of the device are provided next.

2.2. Nanofabrication of Sub-Wavelength Hole Arrays

The nanohole arrays were fabricated and imaged using a FEI dual-beam Strata 235 focused ion beam and a conventional scanning electron microscope. Device parameters such as the energy to which the gallium ions were accelerated, beam spot size, and the beam current were respectively set to 30 keV, 7.14 μm, and 115 pA. A 3x3 array of sub-wavelength holes was milled into the 100-nm thick gold film on glass substrate (with a 1 nm chromium adhesion layer) commercially available from EMF. The array period was varied along the columns to be 420, 430, and 450 nm and the hole-diameter was varied along the rows to be 225, 250, and 275 nm.

2.3. Microfluidic Chip Assembly

A polydimethylsiloxane (PDMS) chip was fabricated using a replica molding technique reported elsewhere [31 32]. Using CAD software, a mask with a straight, 2-cm long microchannel measuring 200 μm in width and 70 μm in height was generated. A master of the microfluidic channel was fabricated by spin-coating SU-8 100 photoresist (MicroChem Corp., Newton, MA) onto a clean 7.62-cm silicon wafer (Silicon Quest International Inc., Santa Clara, CA), placing the mask over the coated wafer and exposing them to ultraviolet light for 84 seconds. The exposed wafer was post-baked for 10 min at 368 K and subsequently developed using SU-8 developer (MicroChem Corp., Newton, MA.) Next, the master was hard baked at 338 K for 3 min and at 368 K for 22 min. A degassed, 13:1 mixture of Sylgard 184 elastomer (Dow Corning Corp., Midland, MI) and its curing agent was molded over the master. Upon baking the materials at 363 K for 25 min, the replica was removed from the mold. Holes for connecting Polyetheretherketone (PEEK) tubing (Upchurch Scientific, Oak Harbor, WA) were then punched at the microchannel ends for fluid entry. The microfluidic chip was finally aligned and sandwiched with the gold nanohole array substrate, all of which were encased by a 2.54-cm square metal frame with a large central opening for optical access.

3. Results and discussion

3.1. Two-Color Sensing

An initial microfluidic test was conducted to assess changes in refractive index using different solutions. One specific innovation of this device was the use of a dual-color LED. Figure 2a shows white light transmission through the nanohole arrays and LED spectra acquired using established SPR spectroscopy techniques [3, 7] prior to the microfluidic experiment. As shown in Figure 2a, the LED wavelengths were chosen such that one of them (green) increased its output intensity as the refractive index increased, and the other (red) decreased its output intensity. Thus, the LED's spectral maxima lies to the left and right of a nanohole array transmission peak (for a periodicity of 420 nm and diameter of 225 nm). Figure 2b shows the response of the nanohole arrays to the timed introduction of water and glucose solution at a flowrate on the order of ~ 1 μl/min. A fast and repeatable sensor response to the change in refractive index in both red and green lines was found. From 0 to 20 min at the start of the experiment before the glucose is introduced, both the red and green line signals showed detectable, and repeatable, drift which was attributed to thermal effects. For that reason, a drift correction procedure was applied according to

well established methods [36]. Additionally, two aspects are noteworthy: (1) the magnitude of the signal change in response to the introduction of solutions with different indexes of refraction is significantly higher than the drift, and (2) automated calibration before and after testing, as performed with commercial SPR units, would mitigate the influence of the drift on the measurement. The transmission coefficient was permitted to reach a steady-state value before reintroducing a liquid into the channel. The LED was toggled to temporally separate the green and red signals for detection on the CCD sensor. Compared to other works that used biaxial arrays [37] and multiple arrays of different periodicity [7, 9, 30], the two-color scheme benefits from allowing for uniform and uniaxial array fabrication, which is more amenable to low-cost fabrication methods.

3.2. Bulk Sensitivity Test

To determine the bulk sensitivity of the device, we prepared five test solutions of incremental concentrations (10%, 15%, 20%, 25%, and 30%) of C_2H_5OH in H_2O. These solutions were then injected into the device in series. The combination of nanohole array and LED wavelength generating the largest shift in pixel intensity was found to be 250-nm diameter holes with 430-nm hole-pitch and red LED. Figure 3a shows the step-waveform with the introduction of each subsequent solution of higher refractive index on this sensor (only red LED output is shown in this case). As shown, the system responded to each step change in refractive index. Perturbations in the signal in between solutions are attributed to the effect of solution mixing. Figure 3b plots the pixel intensity as a function of the bulk refractive index. From this figure, a sensitivity of 266 pixel intensity units/RIU was calculated. The dependent and independent variables are linearly related, with a squared Pearson's correlation coefficient of 0.989. The limit of detection (defined by signal-to-noise ratio of 3) was found to be 6×10^{-4} RIU. The applied statistical techniques are similar to the methods from a previous report by Hwang et. al. [38].

3.3. Dynamic Surface Binding Test

To demonstrate the sensor's ability to detect surface binding events, similar to processes used in quantitative biosensing, an analyte-receptor binding process was monitored [38, 39]. The biotin-streptavidin complex, with a dissociation constant on the order of $\sim 10^{-14}$ M, was selected for the experiment given that it could reliably alter the surface refractive index [40]. Prior to the binding test, the nanohole array was plasma-cleaned for 15 min., sonicated in methanol for 5 min. and immersed in a 5.18 mM cysteamine solution in water for 72 h to assemble a monolayer [9]. Upon completion of incubation, it was then removed, gently rinsed with isopropyl alcohol as well as with purified water, and immersed in a 17.6 mM NHS-biotin solution in dimethyl sulfoxide (DMSO) for an additional 4 h. Following installation of the nanostructure into the chip assembly, preliminary volumes of pH 7 phosphate buffered saline (PBS) were flushed through the microchannels for a settling period of 20 min.

The experiment consisted of an initial 10 min PBS flush period followed by the subsequent introduction of the rest of the solutions. The signal was continuously acquired in order to assess the dynamic binding events at the nanohole arrays, as shown in Figure 4. At 10 min, a 2 μM streptavidin solution in PBS was added. A gradual increase and decrease in transmission was observed for the red and the green source, respectively. At the 60 min mark, the sensor indicated that the surface concentration was saturated, and the system was flushed with PBS. The signal-to-noise ratio (SNR) of the curve was calculated by comparing it to the resultant signal from subtracting green and red LED output intensities as shown in Figure 4b. This was performed to establish that the SNR would increase, as the value rose from 11.4 (given $SNR_{Ori.} = Signal_{Ori.}/Noise_{Ori.} = 0.570/0.0501 = 11.4$) for the original binding curve to 17.2 (given $SNR_{Sub.} = Signal_{Sub.}/Noise_{Sub.} = 0.875/0.0510 = 17.2$) for the subtraction curve. As expected, the signal trend attained after the PBS flush was constant. This is related to the high affinity constant of the biotin-

streptavidin system [46] in which the dissociation time is long (in the order of hours). It is also important to note that the long time for reaching saturation in this experiment might be due to the adsorption of the streptavidin to the inner tubing walls of the particular configuration used here, which may result in lower concentrations reaching the sensor at early times of the experiment. Another factor that may play a role in the longer saturation time is the efficiency of the analyte collection at the sensing surface. The cross-stream diffusion to advection times in the frame of analyte collection efficiency discussed in recent studies [35, 42]. Most importantly, these results demonstrate that the integrated device enables the detection of surface binding. The device is also compatible with established methods to increase the transport of reactants to the nanohole array sensing surface, such as the flow-through nanohole array approach that we have shown to greatly increase the sensor response rate [34, 35]

4. Conclusions and Outlook

In summary, we have developed an integrated, compact, nanohole array-based SPR sensing device. The device uses a two-color LED sensing scheme which can be used to distinguish between spurious sensing artifacts and the detection signal, as pairs of optical signals can be expected to exhibit complementary behaviour. The result is a sensing system that would be immune to changes, for instance, in ambient light levels as expected in the field. Bulk sensing and dynamic surface binding were demonstrated, with a bulk sensitivity of 266 pixel intensity units/RIU, LOD of 6×10^{-4} RIU (with potential for improvement by two orders of magnitude), and sequential binding process response for 2 μM streptavidin to biotin. The integrated nature of this apparatus, as well as its relatively low component cost and potential for multiplexing, make it a promising development for future point-of-care diagnostics and field research. Further optimization, by exploiting the full dynamic range of the sensor, can be expected to enable a three-fold improvement in LOD. Other improvements would come at the expense of increased complexity and cost, for example, by improving nanostructures which may exclude the use of broad-area, low cost lithographic fabrication of arrays. Importantly, this device is compatible with the flow-through nanohole array approach that has been shown to greatly increase sensor response rate and is specific to nanohole-based methods. In contrast, we do not believe that significant sensitivity enhancements can be achieved by increasing the number of nanoholes because the arrays already contain over 1100 nanoholes, which is well beyond the typical saturation in the spectral response of 300 nanoholes. Based on these factors, similar sensitivities to those reported recently for nanohole arrays [43], which lay in the order of 10^{-6} RIU, are anticipated with this configuration. The results presented here indicate that it is feasible to exploit the various advantages of nanohole array based sensing in a compact field-portable device.

Acknowledgements

CE would like to thank Chiara Valsecchi and Ryan Abel for their assistance and valuable discussions. This work was supported by the Canada Research Chairs program as well as the Natural Sciences and Engineering Research Council (NSERC) through a scholarship to CE, a research award to SV, Discovery Grants and Strategic Network for Bioplasmonic Systems (Biopsys).

References

[1] E. Kretschmann, H. Raether, "Radiative decay of non radiative surface plasmons excited by light," *Z. Naturforsch. A*, vol. 23, pp. 2135-2136, 1968.

[2] K. M. Byun, "Development of Nanostructured Plasmonic Substrates for Enhanced Optical Biosensing," *J. Opt. Soc. Korea*, vol. 14, no. 2, pp. 65-76, Jun. 2010.

[3] J. Homola "Surface plasmon resonance sensors for detection of chemical and biological species," *Chem. Rev.*, vol. 108, no. 2, pp. 462-493, Jan. 2008.

[4] G. L. Liu, J. Kim, Y. Lu and P. Lee, "Optofluidic control using photothermal nanoparticles," *Nat. Mater.*, vol. 5, no. 1, pp. 27-32, Jan. 2006.

[5] R. Gordon, D. Sinton, K. L. Kavanagh, and A. G. Brolo, "A new generation of sensors based on extraordinary optical transmission," *Acc. Chem. Res.*, vol. 41, no. 8, pp. 1049-1057, Jul. 2008.

[6] T. W. Ebbesen, H. J. Lezec, H. F. Ghaemi, T. Thio, and P. A. Wolff, "Extraordinary optical transmission through sub-wavelength hole arrays," *Nature*, vol. 391, pp. 667-669, Feb. 1998.

[7] A. G. Brolo, R. Gordon, B. Leathem, and K. L. Kavanagh, "Surface plasmon sensor based on the enhanced light transmission through arrays of nanoholes in gold films," *Langmuir*, vol. 20, no. 12, pp. 4813-4815, May 2004.

[8] A. G. Brolo, J. Ferreira, M. J. L. Santos, C. Escobedo, D. Sinton, E. M. Girotto, F. Eftekhari and R. Gordon, "Development of plasmonic substrates for biosensing," *Proc. SPIE*, DOI: 10.1117/12.793798, Sep. 2008.

[9] A. De Leebeeck, L. K. S. Kumar, V. de Lange, D. Sinton, R. Gordon, and A. G. Brolo, "On-chip surface-based detection with nanohole arrays", *Anal. Chem., vol. 79*, no. 11, pp. 4094–4100, Apr. 2007.

[10] L. S. Jung, C. T. Campbell, T. M. Chinowsky, M. N. Mar and S. S. Yee, "Quantitative Interpretation of the Response of Surface Plasmon Resonance Sensors to Adsorbed Films," *Langmuir*, vol. 14, no. 19, pp. 5636-5648, Aug. 1998.

[11] K. A. Tetz, L. Pang and Y. Fainman, "High-resolution surface plasmon resonance sensor based on linewidth-optimized nanohole array transmittance," *Opt. Lett.*, vol. 31, no. 10, pp. 1528-1530, May 2006.

[12] P. R. H. Stark, A. E. Halleck and D. N. Larson, "Short order nanohole arrays in metals for highly sensitive probing of local indices of refraction as the basis for a highly multiplexed biosensor technology," *Methods*, vol. 37, no. 1, pp. 37-47, Sep. 2005.

[13] K. A Tetz, R. Rokitski, M. Nezhad and Y. Fainman, "Excitation and direct imaging of surface plasmon polariton modes in a two-dimensional grating," *Appl. Phys. Lett.*, vol. 86, art. no. 111110, Mar. 2005.

[14] A. Lesuffleur, H. Im, N. C. Lindquist and S-H. Oh, "Periodic nanohole arrays with shape-enhanced plasmon resonance as real-time biosensors," *Appl. Phys. Lett.*, vol. 90, art. no. 243110, Jun. 2007.

[15] E. Altewischer, C. Genet, M. P. van Exter, J. P. Woerdman, P. F. A. Alkemade, A. Van Zuuk and E. W. J. M. van der Drift, "Polarization tomography of metallic nanohole arrays," *Opt. Lett.*, vol. 30, no. 1, pp. 90-92, Jan. 2005.

[16] J. Homola, *Surface Plasmon Resonance Based Sensors.* Springer, Berlin, 2006.

[17] J. W. Menezes, J. Ferreira, M. J. L. Santos, L. Cescato, and A. G. Brolo, "Large-Area Fabrication of Periodic Arrays of Nanoholes in Metal Films and Their Application in Biosensing and Plasmonic-Enhanced Photovoltaics," *Adv. Funct. Mater.*, vol. 20, no. 22, pp. 3918-3924, Nov. 2010.

[18] L. Pang, W. Nakagawa, and Y. Fainman, "Fabrication of two-dimensional photonic crystals with controlled defects by use of multiple exposures and direct-write," *Appl. Opt.*, vol. 42, no. 27, pp. 5450-5456, Sep. 2003.

[19] S. Y. Chou, P. R. Krauss, and P. J. Renstrom, "Imprint of sub-25 nm vias and trenches in polymers," *Appl. Phys. Lett.*, vol. 67, no. 21, pp. 3114-3116, Nov. 1995.

[20] C. L. Haynes and R. P. Van Duyne, "Nanosphere Lithography: A Versatile Nanofabrication Tool for Studies of Size-Dependent Nanoparticle Optics," *J. Phys. Chem. B.*, vol. 105, no. 24, pp. 5599-5611, May 2001.

[21] C-H. Sun, W-L. Min, and P. Jiang, "Templated fabrication of sub-100 nm periodic nanostructures," *Chem. Commun.*, pp. 3163-3165, Jul. 2008.

[22] Y. Liu and S. Blair, "Fluorescence enhancement from an array of subwavelength metal apertures," *Opt. Lett.*, vol. 28, no. 7, pp. 507-509, Apr. 2003.

[23] M. A. Cooper, "Label-free screening of bio-molecular interactions," *Anal. Bioanal. Chem.*, vol. 377, no. 5, pp. 834-842, Aug. 2003.

[24] Y. Li, J. Pan, P Zhan, S. Zhu, N. Ming,, Z. Wang, W. Han, X. Jiang, and J. Zi, "Surface plasmon coupling enhanced dielectric environment sensitivity in a quasi-three-dimensional metallic nanohole array," *Opt. Express*, vol. 18, no. 4, pp. 3546-3555, Feb. 2010.

[25] L. S. Jung, C. T. Campbell, T. M. Chinowsky, M. N. Mar, and S. Yee, "Quantitative Interpretation of the Response of Surface Plasmon Resonance Sensors to Adsorbed Films," *Langmuir*, vol. 14, no. 19, pp. 5636-5648, Aug. 1998.

[26] A. Krishnan, T. Thio, T. J. Kim, H. J. Lezec, T. W. Ebbessen, P. A. Wolff, J. Pendry, L. Martin-Moreno, and F. J. Garcia-Vidal, "Evanescently coupled resonance in surface plasmon enhanced transmission," *Opt. Commun.*, vol. 200, no. 1, pp. 1-7, Dec. 2001.

[27] I. T. Kim and K. D. Kihm, "Label-free visualization of microfluidic mixture concentration fields using a surface plasmon resonance (spr) reflectance imaging," *Exp. Fluids*, vol. 41, no. 6, pp. 905-916, Oct. 2006.

[28] A. Lesuffleur, H. Im, N. C. Lindquist, K. S. Lim and S-H. Oh, "Laser-illuminated nanohole arrays for multiplex plasmonic microarray sensing," *Opt. Express.*, vol. 16, no. 1, pp. 219-224, Jan. 2008.

[29] R. Gordon, A. G. Brolo, D. Sinton and K. L. Kavanagh, "Resonant optical transmission through hole-arrays in metal films: physics and applications," *Laser & Photon. Rev.*, vol. 4, no. 2, pp. 311-335, Feb. 2010.

[30] N. C. Lindquist, A. Lesuffleur, H. Im, and S-H. Oh, "Sub-micron resolution surface plasmon resonance imaging enabled by nanohole arrays with surrounding Bragg mirrors for enhanced sensitivity and isolation," *Lab Chip*, vol. 9, no. 3, pp. 382-387, Feb. 2009.

[31] D. C. Duffy, J. C. McDonald, J. A. Schueller, and G. M. Whitesides, "Rapid Prototyping of Microfluidic Systems in Poly(dimethylsiloxane)," *Anal. Chem.*, vol. 70, no. 23, pp. 4974-4984, Oct. 1998.

[32] J. C. McDonald, D. C. Duffy, J. R. Anderson, D. T. Chiu, H. Wu, O. J. A. Schueller, and G. M. Whitesides, "Fabrication of Microfluidics Systems in Poly(dimethylsiloxane)," *Electrophoresis*, vol. 21, no. 1, pp. 27-40, Jan. 2000.

[33] Y. Liu, J. Bishop, L. Williams, S. Blair, and J. Herron, "Biosensing based upon molecular confinement in metallic nanocavity arrays," *Nanotechnology*, vol. 15, no. 9, pp. 1368-1374, Aug. 2004.

[34] F. Eftekhari, C. Escobedo, J. Ferreira, X. Duan, E. M. Girotto, A. G. Brolo, R. Gordon, and D. Sinton, "Nanoholes as nanochannels: flow-through plasmonic sensing," *Anal. Chem.*, vol. 81, no. 11, pp. 4308-4311, May 2009.

[35] C. Escobedo, A. G. Brolo, R. Gordon, and D. Sinton, "Flow-Through vs. Flow-Over: Analysis of Transport and Binding in Nanohole Array Plasmonic Biosensors," *Anal. Chem.*, DOI: 10.1021/ac101654f, Nov. 2010.

[36] M. L. Salit adn G. C. Turk, "A drift correction procedure," *Anal. Chem.*, vol. 70, pp. 3184-3190.

[37] F. Eftekhari, R. Gordon , J. Ferreira , A. G. Brolo ,and D. Sinton, "Polarization-dependent sensing of a self-assembled monolayer using biaxial nanohole arrays," *Appl. Phys. Lett.,* vol. 92, art. no. 253103, Jun. 2008.

[38] G. M. Hwang, L. Pang, E. H. Mullen, and Y. Fainman, "Plasmonic Sensing of Biological Analytes Through Nanoholes*," IEEE Sens. J.*, vol. 8, no. 12, pp. 2074-2079, Dec. 2008.

[39] V. H. Pérez-Luna, M. J. O'Brien, K. A. Opperman, P. D. Hampton, G. P. López, L. A. Klumb, and P. S. Stayton, "Molecular Recogni*tion betwee*n Genetically Engineered Streptavidin and Surface-Bound Biotin," *J. Am. Chem. Soc*., vol. 121, no. 27, pp. 6469-6478, Jun. 1999.
[40] M. Srisa-Art, E.C. Dyson, A. J. deMello, and J. B. Edel, "Monitoring of Real-Time Streptavidin-Biotin Binding Kinetics *Using Droplet Mi*crofluidics," *Anal. Chem.*, vol. 80, no. 18, pp. 7063-7067, Aug. 2008.
[41] T. M. Squires, R. J. Messinger, and S.R. Manalis, "Making it stick: convection, reaction and diffusion in surface-based biosensors," *Nat. Biotechnol.*, vol. 26, no. 4, pp. 417-426, Apr. 2008.
[42] J. Ferreira, M. J. L. Santos, M. M. Rahman, A. G. Brolo, R. Gordon, D. Sinton and E. M. Girotto, "Attomolar Protein Detection Using in-Hole Surface Plasmon Resonance," *J. Am. Chem. Soc., vol. 131, no. 2, pp.* 436-437, Dec. 2008.
[43] K. Lee, S. Wu and P. Wei, "Intensity sensitivity of gold nanostructures and its application for high-throughput biosensing," Opt. Express **17,** 23104-23113 (2009).

Figures

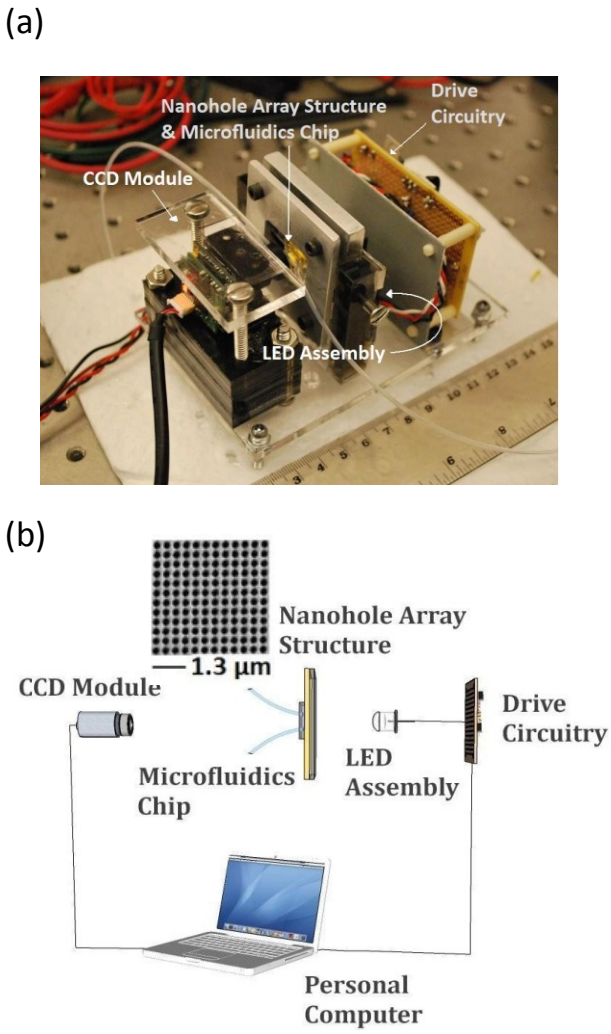

Figure 1. (a) Photograph of the SPR sensing device, with labels indicating components. (b) Schematic of the SPR imaging device, encompassing a standard experimental configuration for measuring light transmission through 9 arrays of sub-wavelength holes. An SEM image of the nanohole array of 420-nm periodicity and 275-nm hole-diameter is shown. .

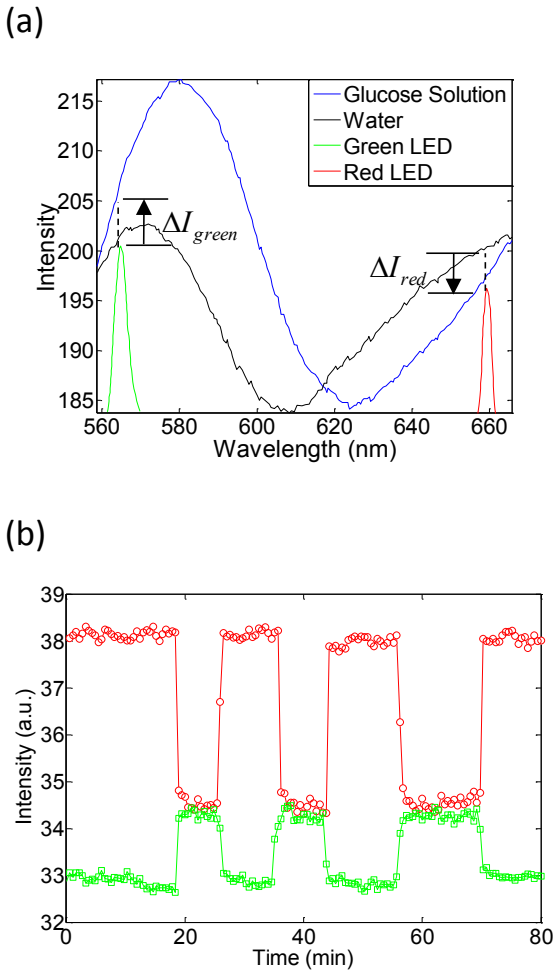

Figure 2. (a) Superimposed nanohole array and LED spectrums. (b) Proof-of-concept profile for alternating bulk refractive indices, n_w = 1.3333 and n_γ = 1.3624. Local minima for the output response of the red LED coupled with the maxima for that of the green relate to the event where the external dielectric has transitioned to the higher refractive index glucose solution.

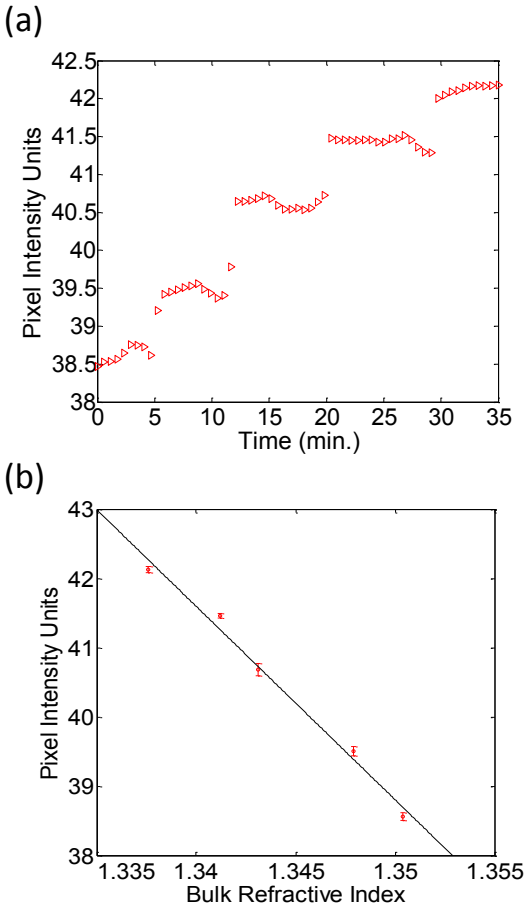

Figure 3. (a) Pixel intensity waveform for the array of 250-nm hole-size and 430-nm hole-pitch obtained through perturbing ethanol-water solution molarities. A moving average filter was applied to each step, where the fixed subset size was equal to 3 and zero-padded samples were discarded. (b) Line of best fit for a series of mean pixel intensities and bulk refractive index points, where the error bars represent the standard deviations for sample measurements.

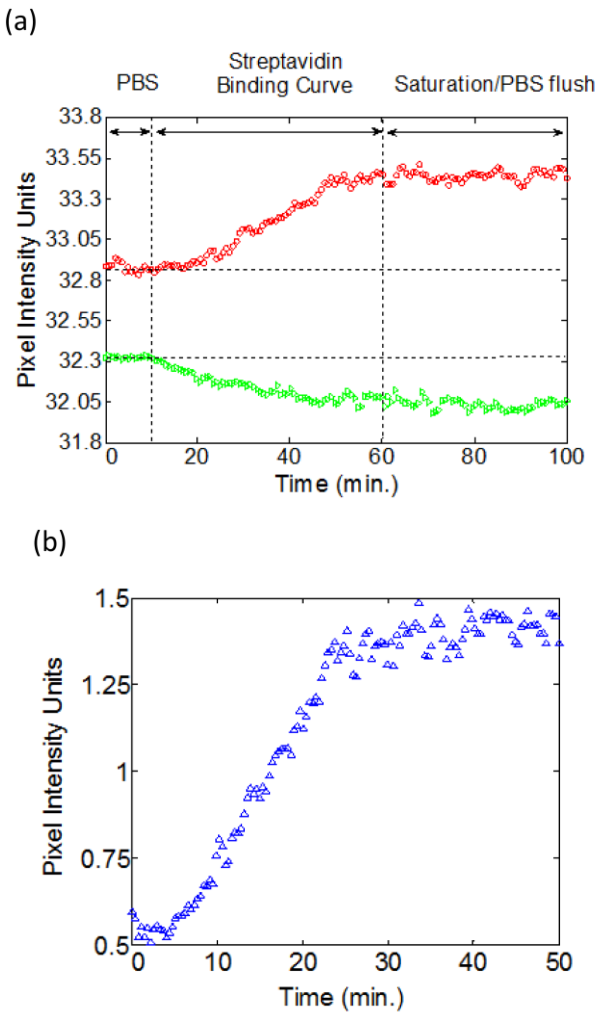

Figure 4. (a) Biotin-streptavidin binding curve for the array of 275-nm hole-size and 420-nm hole-pitch. The streptavidin solution was introduced at 10 min. And saturation was achieved after ~ 40 min. (b) Plot of the difference between red and green LED pixel intensities, which enhances the SNR of the system. This can be seen by observing how the binding response has been magnified, having increased by an approximate factor of 1.51 (where $SNR_{Sub.}$ /$SNR_{Ori.}$ = 17.2/11.4 = 1.51).

Appendix E

Quantitative Real-Time Plasmonic Sensing with an Integrated Microfluidic Concentration Gradient Generator

Quantitative Real-Time Plasmonic Sensing with an Integrated Microfluidic Concentration Gradient Generator

Escobedo, C[1], Gordon, R[2], Brolo, A. G.[3], Sinton, D.[1], Ferreira, J.[4,*]

[1]Department of Mechanical Engineering, University of Victoria, BC, V8W 3P6, Victoria, BC, Canada.

[2]University of Victoria, Department of Electrical and Computer Engineering, BC, V8W 3Z8, Victoria, BC, Canada.

[3]University of Victoria, Department of Chemistry, P.O. Box 3065, V8W 3V6, Victoria, BC, Canada.

[4]Centro de Ciências Químicas, Farmacêuticas e de Alimentos, Universidade Federal de Pelotas, P.O. Box 354, 96010-900, Pelotas, Rio Grande do Sul, Brazil

*E-mail: jacqueline.research@gmail.com

Tel: +55 53 3275 7356

FAX: +55 53 3275.7533

Abstract

In this work, a nanohole array SPR-based biosensor with an integrated microfluidic concentration gradient generator for imaging detection and quantification of ovarian cancer antibody (AB) and antigen (AG) was demonstrated. Calibration curves based on controlled concentrations of analyte were created using a microfluidic stepped diffusive mixing scheme. Quantification of samples with unknown concentration of analyte was achieved by image-intensity comparison with the calibrations curves, in analogy to well established standard biochemical macroscopic diagnostics. The biosensor was first used to detect and quantify the immobilization of antibody PAX8, revealing a concentration of *ca.* 24.85 ± 0.05μg.mL^{-1} agreeing within 5% with the effective concentration of the sample. The biosensor was then used in the detection of ovarian cancer AG r-PAX8 using the same sensing scheme. For this test, two concentrations of AG were used. Detection was achieved by SPR imaging and the quantification revealed AG concentrations 1.35 ± 0.08 μg/mL and 6.18 ± 0.09 μg/mL, which lay within 30% of the effective concentrations used for the test. The proposed biosensor demonstrated the ability of self-generating calibration curves on-chip in an integrated microfluidic-SPR based platform, representing a further step towards the development of comprehensive lab-on-chip biomedical diagnostics.

Keywords: biosensor, surface plasmon resonance, nanohole, microfluidic, quantitative detection, biomarker, antibody, antigen, ovarian cancer

Introduction

Biomarker detection and quantification are essential for early cancer detection [1]. In addition, quantitative monitoring of biomolecular interaction is appealing for many diagnosis applications and usually critical for those involving protein interactions for gene expression, virology, cell signaling and biomarker detection [2-4]. Specifically, biomarker detection involve different types of protein interactions, including specific and non-specific protein-protein interactions as well as protein interactions with other molecules such as metabolites, nucleic acids and drug molecules [2, 5, 6]. Several characteristics of these interactions, including dynamic binding characteristics of the binding event can be studied using quantitative sensors.

In the past decades, intensive efforts have been made for developing microfluidic-based biochemical diagnosis platforms that integrate several functions on-chip, towards the development of factual micro-total analysis systems (μTAS). The benefits offered by microfluidic-based technologies are well documented [7, 8], including their potential integration into portable point-of-care (POC) and point-of-use (POU) diagnostic systems [9]. Biomarker quantization in microfluidic-based systems frequently requires the use of standard methods and calibration at each test. Calibration curves are extensively used in traditional analytical chemistry for analyte quantization [10-12] and have been incorporated into microfluidic platforms in the past [13-15]. Thus, the conception of a microfluidic system with the capability of generating calibration curves integrated with a high-sensitive biosensing platform is particularly attractive.

Surface plasmons are electromagnetic waves resulting from coupling of electromagnetic radiation at the interface between a metallic film and a dielectric, confined to the near-interface region. Surface plasmons are highly sensitive to near-surface refractive index, making them suitable for biosensing applications [16]. Metallic nanostructures enable the excitation of surface

plasmons which are local to the structure [17]. Nanohole arrays in metal films support localized surface plasmons (LSPs) [18, 19] and exhibit extraordinary optical transmission (EOT) at resonant wavelengths [20, 21]. This unique characteristic of nanohole arrays is relevant for obtaining biosensors with simpler configuration than the proposed by Kretschman, allowing the fabrication of miniaturized devices. Additionally, as sensing elements, nanohole arrays have several advantages including a high level of reproducibility, small footprint, high sensitivity of the optical response to geometry, periodicity and lattice versus basis orientation and they enable the use of high numerical aperture optics under transmission mode at normal incidence [22]. Nanohole array based sensing is most applicable to the detection of adsorbed species, in analogy with conventional SPR sensing. Therefore, molecular adsorption may be detected directly, without a label. This has motivated the use of nanohole arrays as biosensors [23, 24].

Nanohole array SPR imaging is an optical technique based in the measurement of transmitted light across the nanohole array substrate. The location of the plasmon resonance shifts upon molecular adsorption which produces a change in transmitted intensity at a specific wavelength. Maybe, the main advantage of this method is the possibility of multiple analyte detection, in addition to a quantitative detection during a real-time measurement, without a label

Integration of nanohole arrays in microfluidic chips has been recently reported in several studies [2, 25, 26]. In many cases, single microchannels provided control of solutions as well as planar interfaces well-suited to optical transmission experiments [27, 28]. Arrays of nanohole arrays were integrated on-chip by DeLeebeeck et al. [29] and applied to detect a spatial concentration gradient and to monitor the sequential adsorption of a biotin-streptavidin system. More recently, studies have focused on minimizing the footprint of the sensors, increasing the density of nanoholes and arrays, improving the kinetics of adsorption and the sensitivity of the approach

[30, 31]. Lindquist et al. reported SPR imaging sensing with arrays of nanohole arrays enhanced by plasmonic Bragg mirrors [25]. In all these cases, multiplexed arrays were in a common fluidic environment, such as a chamber, similar to a microarray format.

All the advantages presented by nanohole based biosensor integrated to microfluidic systems can be explored on the detection of diseases that have caused the death of many patients. The number shows that early detection of cancer is critical to effective treatment and survival, for example, it is observed 95% survival rate for early detection of ovarian cancer, whereas late detection is almost always fatal. Hence, the need for screening is particularly acute for ovarian cancer which is generally asymptomatic until late stages, being one of the hardest to diagnose at early stages.

Recently the Ovarian Cancer Institute of Atlanta with the Georgia Institute of Technology have found that the transcription factor PAX8 is highly expressed in epithelial ovarian cancer but absent from the same cells of healthy individuals. Based on these information and concerns, in this paper, we demonstrate simultaneous and quantitative label-free detection of the ovarian cancer biomarker PAX8 using an array of nanohole arrays integrated with a microfluidic concentration gradient generator. The approach is used to generate, in every test, a calibration curve on-chip, using points of known analyte concentration for the quantification of a sample of unknown concentration flowing in parallel. The concentration gradient is achieved by stepped diffusive mixing of two base streams with known analyte concentration. Each of the diluted streams generated by the mixing process is directed along six outlet microchannels flowing in parallel with a microchannel containing the sample to analyze. Four in-line nanohole arrays are used for sensing each concentration of biomarker at the outlet channels, as well as for the individual sample channel. The quantification of biomarker concentration in the sample stream is achieved by SPR imaging via direct transmission on a CCD. As the amount of bound analyte to

the nanohole arrays is proportional to the analyte concentration in the specific outlet microchannel, the transmitted light from nanohole arrays in different microchannels also varies. These intensity variations are tracked and the determinations of unknown analyte concentrations are achieved by comparison with the standard curve. The approach presented here is a further step towards comprehensive affordable POC and POU biochemical diagnostics.

Materials and Methods

Nanohole array fabrication.

Nanohole arrays were fabricated by focused-ion beam (FIB) milling in commercial glass slides (EMF, Ithaca, NY) with 100 nm-thick Au coating and a 5 nm thick Cr adhesion layer. For milling, the ion beam was set to 30 keV with a beam current of 30 pA. The typical beam spot of the beam size was 10 nm, and the dwell time was 2 ms. The resulting arrays were 15 μm by 15 μm with holes of 200 nm in diameter and periodicity of 420 nm. A total of 28 nanohole arrays were fabricated in an arrangement consisting of 7 columns and 4 rows with a total footprint of less than 1.0 mm by 0.4 mm. The fabricated arrays were inspected using scanning electron microscopy (SEM). Figure 1 shows the SEM images from nanohole arrays detailing the nanostructure.

Microfluidic concentration gradient generator fabrication

For the fabrication of the microfluidic concentration gradient generator, replica molding technique was employed. This technique is widely used in microfluidic applications and it is reported in detail elsewhere [32]. The general steps during the fabrication procedure are described next. A mask with the microfluidic pattern was generated using CAD software. The

design included three inlets and two outlets of 1.5 mm and seven 90-μm wide microchannels, with a total footprint of 22 by 22 mm, as shown in Figure 2. Next, a master was fabricated by spin-coating SU-8 50 photoresist (MicroChem Corp., Newton, MA) onto a clean 3 inch silicon wafer (Silicon Quest International Inc, Santa Clara, CA). The coated wafer was then pre-baked at 65°C and 95°C for 1 and 6 minutes, respectively. The mask with the microfluidic pattern was then placed over the coated wafer and exposed to UV light for 90 seconds. Next, the exposed wafer was hard baked at 65°C for 1 minute and at 95°C for 10 minutes. The master was subsequently developed using SU-8 developer (MicroChem Corp., Newton, MA). A 14:1 mixture of Sylgard 184 elastomer to curing agent (Dow Corning, Midland, MI) was mixed, degassed and poured onto the master. After baking at 85°C for 20 minutes, the replica was removed from the mold. Inlets and outlets were provided 1-mm punched holes for fluidic access. Polyetheretherketone (PEEK) tubing (Upchurch Scientfic, Oak Harbor, WA) was used for fluidic connections. Microscrew syringe pumps (Harvard Apparatus, MA) were used to infuse the solutions into the microchip.

Experimental Setup.

A schematic representation of the experimental setup is shown in Figure 3. The microfluidic chip was placed on top of the nanohole arrays substrate, with the columns of nanohole arrays aligned with the outlet microchannels. An acrylic top plate was used to mechanically seal the system. A Helium-Neon (He-Ne) laser beam with emission at 632.8 nm was used as the excitation source on the nanohole arrays at normal incidence. Two 20X working distance microscope objectives (Leica Microsystems, Wetzlar, Germany) were used to expand the beam uniformly over the nanohole arrays. The transmitted light through the arrays was acquired using a cooled CCD

camera (Photometrics HQ_2, Austin, USA). The CCD images were acquired using a software-controlled shutter and an integration time of 20 milliseconds. The transmitted light intensity was measured by using a commercial image analysis software.

Chemicals

Dithiobis(succinimidyl undecanoate) (DSU, 92.7%) was purchased from Dojindo (Dojindo Molecular Technologies Inc., Japan). Dimethyl sulfoxide (DMSO) was purchased from Caledon (Caledon Labs, Georgetown, ON). Sodium chloride (99%), sodium phosphate dibasic (99%) and potassium chloride (99%) were purchased from ACP (ACP Chemicals Inc., Toronto, ON), and fluorescein was purchased from Invitrogen (Invitrogen Corp., Carlsbad, CA). Paired box gene 8 (PAX8) and the antigen r-PAX8 were provided by the Trev & Joyce Deeley Research Centre of the British Columbia Cancer Agency (Victoria, BC).

Results and Discussion

Microfluidic Chip Characterization

Figure 2 shows a CAD drawing of the microfluidic chip used in this work. The chip included a microfluidic network with 2 inlets branching and increasing the number of channels by one at each dilution step, ending in 6 independent microchannels with a common outlet. Pure phosphate buffer solution (PBS) were infused in one of the inlets and 1 mM fluorescein PBS into the second inlet. A flow rate of 5 µl/min was used for both inlets. The laminar regime of microfluidic flows allows the existence of co-laminar flows, where mixing is completely dominated by diffusion. In this chip design, the lengths of the microchannels were calculated, based in the required residence times, to ensure full mixing of the encountering streams. At each

mixing step and throughout the entire microfluidic network, the outer channels transported the original concentrations from the inlets and the mixture in the middle channels had a volume ratio of 1:1. A separate single channel with 1 inlet and 1 outlet ran parallel to the 6 outlet channels from the network and was used to transport the sample fluid containing the analyte at unknown concentration.

Fluorescence microscopy was used to characterize the dilution scheme resulting from the microfluidic concentration gradient generator (Figure 4). The fluorescein solution was visualized through a fluorescence visualization system comprised by a Leica DMI6000B epi-fluorescent microscope (Leica, Germany) and Orca AG CCD camera (Hamamatsu, Japan). Images were acquired at a rate of 2 frames per second and exposure time of 400 ms. The images were 1324 x 1024 pixels and had an 8-bit dynamic range. Figure 4a shows a fluorescence image of the 6 outlet microchannels under chip operation. Figure 4b shows the averaged relative concentration at each microchannel as function of pixel intensity (n=10).

SPR Biosensing

The nanohole arrays were cleaned in an ultrasonic bath for 3 min, rinsed with ethanol and with water, and dried with N_2 before the experiments. Next, to allow chemisorptions of the biomolecules, a DSU monolayer was assembled on the arrays by immersing the sample in 2 mM DSU in DMSO for 72 hours. The walls of the microfluidic chip were coated with 0.1 mM Bovine Serum Albumin (BSA) solution to avoid non-specific adsorption. The nanohole arrays were then aligned with the microchannels as shown in Figure 5. An acrylic top plate was used to mechanically seal the system..

Ovarian Cancer Antibody Immobilization

The first experiment involved the immobilization of ovarian cancer antibody PAX8 on the sensors. The microfluidic chip was then used to create a concentration gradient from a 27 μg/mL PAX8 solution in PBS (pH 7.5). One of the inlets was provided with the PAX8 solution while the other one was provided with pure PBS. Both solutions were transported into the microfluidic chip at a fixed flow rate of 10 $\mu L.min^{-1}$. This resulted in 6 different concentrations at the outlet channels flowing over the 6 column of nanohole arrays. At the same time, in the separate channel, a blind test was run by flowing a sample with PAX8 solution at an unknown concentration to the experimenter. The microfluidic configuration allowed parallel reading on the 7 microchannels at the detection zone (Figure 2). Figure 6 shows the SPR image of the sample acquired with the CCD camera after 15 min of the introduction of the AB solution. The transmitted light intensity through the arrays varies with the concentration of AB solution. The intensity of transmitted light in nanohole arrays with 420 nm of periodicity is expected to decrease with a corresponding increase in the refractive index of the surrounding medium [33]. This image suggests an increase of refractive index from column 1 to column 6. As the PAX8/PBS is a diluted solution, the refractive index of pure PBS and PBS containing the AB are the same (1.3333 at 22.1°C). Therefore, the transmitted light intensity differences observed in Figure 6 suggests changes on the effective refractice index, resulted from the immobilization of PAX8 on the arrays.

Figure 7a shows the normalized intensities for each channel, including the sample channel. The maximum normalized intensity occurs in microchannel 1 (*ca.* 30 Pixel), which has the most diluted solution flowing over the arrays, which means that few or even none PAX8 was adsorbed on the gold surface. Figure 7b shows the average normalized intensity from all the arrays in each

column. Notice the similarity of the curve shape with the one presented in Figure 4b. The unknown concentration of the sample was quantified by comparison with the standard curve, assuming that the solution concentration is proportional to the amount of molecules adsorbed on the surface, which causes changes on the effective refractive index. This comparison reveals a concentration of *ca.* $24.85 \pm 0.05 \mu g.mL^{-1}$, which is in close agreement with the effective concentration of the sample (23.70 $\mu g.mL^{-1}$), giving a relative error of *ca.* 4.8 %.

Ovarian Cancer Antigen Detection

Prior to the experiment, a DSU monolayer was assembled on the nanohole arrays as described in the previous section. PAX8 was then immobilized homogeneously on all the nanoholes arrays. Next, the microfluidic chip was used to generate an antigen concentration gradient by introducing an 8.50 $\mu g\ mL^{-1}$ r-PAX8 solution in PBS and pure PBS at the inlets, at a constant flow rate of 10 $\mu L\ min^{-1}$. Using a similar approach than in the experiment detailed in the previous section of this work, two blind tests were achieved by flowing samples of antigen solutions, with unknown concentration to the experimenter, in the individual sample channel of the chip. The concentration of AG was different in each test. One involved a less concentrated r-PAX8 solution (2.00 μg/mL), while the other one involved a more concentrated r-PAX8 solution (5.30 μg/mL). Figure 8 shows the SPR image at 15 min. following introduction of the antigen solution for the low antigen concentration experiment.

Figure 9 shows the normalized intensities of all the arrays in each channel for the detection of r-PAX8. Figures 9a and 9b present the normalized intensities of the low and high r-PAX8 concentration samples, respectively. For the arrays under the concentration gradient scheme (i.e. channels 1 to 6), the changes in intensity were not as pronounced as those observed in the

experiment using antibody PAX8. This may be related to: (i) the number of AG molecules adsorbed, which is lower than the AB concentration; and (ii) the size of the AG, which is smaller than the AB. Consequently, the immobilization of the AB on the biosensor may have a larger impact on the effective refractive index, resulting in higher intensity differences. The maximum intensity, as expected, was observed in channel 1 (*ca.* 50 pixels), corresponding to the most diluted solution with smallest effective refractive index. The minimum intensity was observed in channel 6, corresponding to the most concentrated solution. The concentrations of the samples were calculated by comparison to the concentration gradient curve as shown in Figure 10. The best fit to this curve was a polynomial, which differ from the sigmoidal fitting from the previous experiment. Although the imaging-SPR based sensor presented in this work was successfully applied on the detection of the AG, the different curve may be resulted from the difficulty to detect the AG through a direct assay, due its relative small size when compared to an AB molecule. Based on the standard curve, the analysis of the "unknown" solutions. revealed concentrations of 1.35 ± 0.08 μg/mL and 6.18 ± 0.09 μg/mL for the low and high AG concentration solutions, respectively. The relative errors for these measurements were 32% and 17%, respectively.. Even when the agreement is not as close as that in the AB estimation, these results demonstrate the detection and quantification capacities of the methodology presented in this work.

Conclusions

In summary, this paper demonstrated a SPR-based biosensor integrated into a microfluidic concentration gradient generator for the quantitative assessment of ovarian cancer biomarkers. Sensing was achieved by SPR imaging of 28 nanohole arrays (arranged in columns),

simultaneously. Despite the integrated immunoassay be successful applied on a quantitative detection of cancer biomarkers, improvements must be done on the sensitivity and limit of detection to decrease the relative error, allowing an effective application as POC and POU lab-on-chip biomedical diagnostics on the early stage cancer detection, and maybe on the evolution of the patient after a treatment, by for instance analyzing the biomarkers concentration in his blood.

The quantification of analyte was achieved by comparison of the transmitted light intensity from nanohole arrays in contact with sample solutions, to a standard curve generated with the intensities from nanohole arrays under a controlled microfluidic concentration gradient scheme. The concentration gradient was self-generated on-chip via microfluidic stepped diffusive mixing. The experiments consisted of blind tests with sample solutions at concentrations unknown to the experimenter. The ability of the integrated platform to quantify the amount of AB in sample solution during the immobilization of ovarian cancer antibody PAX8 was first tested. The concentration of the sample solution was quantified by comparison with its corresponding standard curve and the results agreed within 5% with the effective concentration. Then, detection of r-PAX8 AG binding and associated quantification of the AG concentration was demonstrated for two solutions differing in AG concentration. The detection of AG binding was successfully achieved and the quantification of AG concentration in each case was achieved with an accuracy of ~ 70% relative to the effective concentration values. Overall, the transmission intensities varied with biomarker concentration. Nanohole arrays in less concentrated solutions, corresponding to higher effective refractive indexes, exhibited higher transmission intensities, in agreement with previous reports. The quantitative assessment of biomarker with the integrated

microfluidic concentration gradient generation scheme presented here is a further step towards the development of comprehensive POC and POU lab-on-chip biomedical diagnostics.

References

1. Xiao, Y. and X. Gao, *Use of IgY antibodies and semiconductor nanocrystal detection in cancer biomarker quantitation.* Biomarkers in Medicine, 2010. **4**(2): p. 227-239.
2. Ji, J., et al., *High-throughput nanohole array based system to monitor multiple binding events in real time.* Analytical Chemistry, 2008. **80**(7): p. 2491-2498.
3. Rao, J., et al., *Using Surface Plasmon Resonance to Study the Binding of Vancomycin and Its Dimer to Self-Assembled Monolayers Presenting d-Ala-d-Ala.* Journal of the American Chemical Society, 1999. **121**(11): p. 2629-2630.
4. Lin, L., et al., *Surface Plasmon Resonance-based Sensors To Identify cis-Regulatory Elements.* Analytical Chemistry, 2004. **76**(22): p. 6555-6559.
5. Hellstrom, I., et al., *The HE4 (WFDC2) Protein Is a Biomarker for Ovarian Carcinoma.* Cancer Res, 2003. **63**(13): p. 3695-3700.
6. Rifai, N. and P.M. Ridker, *High-Sensitivity C-Reactive Protein: A Novel and Promising Marker of Coronary Heart Disease.* Clin Chem, 2001. **47**(3): p. 403-411.
7. Whitesides, G.M., *The origins and the future of microfluidics.* Nature, 2006. **442**(7101): p. 368-373.
8. Fujii, T., *PDMS-based microfluidic devices for biomedical applications.* Microelectronic Engineering, 2002. **61-62**: p. 907-914.
9. Yager, P., et al., *Microfluidic diagnostic technologies for global public health.* Nature, 2006. **442**(7101): p. 412-418.
10. Yacoub-George, E., et al., *Automated 10-channel capillary chip immunodetector for biological agents detection.* Biosensors and Bioelectronics, 2007. **22**(7): p. 1368-1375.
11. Huizing, M., et al., *Pharmacokinetics of paclitaxel and metabolites in a randomized comparative study in platinum-pretreated ovarian cancer patients.* Journal of Clinical Oncology, 1993. **11**(11): p. 2127-2135.
12. Kyriakopoulou, L.G., et al., *Prognostic value of quantitatively assessed KLK7 expression in ovarian cancer.* Clinical Biochemistry, 2003. **36**(2): p. 135-143.
13. Yang, W., et al., *Integrated Microfluidic Device for Serum Biomarker Quantitation Using Either Standard Addition or a Calibration Curve.* Analytical Chemistry, 2009. **81**(19): p. 8230-8235.
14. Fan, R., et al., *Integrated barcode chips for rapid, multiplexed analysis of proteins in microliter quantities of blood.* Nature Biotechnology, 2008. **26**(12): p. 1373-1378.
15. Herr, A.E., et al., *Microfluidic immunoassays as rapid saliva-based clinical diagnostics.* Proceedings of the National Academy of Sciences of the United States of America, 2007. **104**(13): p. 5268-5273.
16. Homola, J., S.S. Yee, and G. Gauglitz, *Surface plasmon resonance sensors: Review.* Sens. Actuat. B, 1999. **54**: p. 3-15.
17. Stewart, M.E., et al., *Nanostructured plasmonic sensors.* Chemical Reviews, 2008. **108**(2): p. 494-521.

18. Zhao, J., et al., *Localized surface plasmon resonance biosensors.* Nanomedicine, 2006. **1**(2): p. 219-228.
19. Gordon, R., et al., *A new generation of sensors based on extraordinary optical transmission.* Accounts of Chemical Research, 2008. **41**(8): p. 1049-1057.
20. Ebbesen, T.W., et al., *Extraordinary optical transmission through sub-wavelength hole arrays.* Nature, 1998. **391**(6668): p. 667-669.
21. Genet, C. and T.W. Ebbesen, *Light in tiny holes.* Nature, 2007. **445**(7123): p. 39-46.
22. Sinton, D., R. Gordon, and A.G. Brolo, *Nanohole arrays in metal films as optofluidic elements: progress and potential.* Microfluidics and Nanofluidics, 2008. **4**(1-2): p. 107-116.
23. Brolo, A.G., et al. *Development of plasmonic substrates for biosensing*. in *Biosensing*. 2008. San Diego, CA, USA: SPIE.
24. Sharpe, J.C., et al., *Gold nanohole array substrates as immunobiosensors.* Analytical Chemistry, 2008. **80**(6): p. 2244-2249.
25. Lindquist, N.C., et al., *Sub-micron resolution surface plasmon resonance imaging enabled by nanohole arrays with surrounding Bragg mirrors for enhanced sensitivity and isolation.* Lab on a Chip, 2009. **9**(3): p. 382-387.
26. Hwang, G.M., et al., *Plasmonic Sensing of Biological Analytes Through Nanoholes.* Ieee Sensors Journal, 2008. **8**(11-12): p. 2074-2079.
27. Tetz, K.A., L. Pang, and Y. Fainman, *High-resolution surface plasmon resonance sensor based on linewidth-optimized nanohole array transmittance.* Optics Letters, 2006. **31**(10): p. 1528-1530.
28. Liu, Y., et al., *Biosensing based upon molecular confinement in metallic nanocavity arrays.* Nanotechnology, 2004. **15**(9): p. DOI 10.1088/0957-4484/15/9/043|PII S0957-4484(04)79391-5.
29. DeLeebeeck, A., et al., *On-Chip Surface-Based Detection with Nanohole Arrays.* Anal. Chem., 2007. **79**(11): p. 4094-4100.
30. Yang, J.-C., et al., *Metallic Nanohole Arrays on Fluoropolymer Substrates as Small Label-Free Real-Time Bioprobes.* Nano Lett., 2008. **8**(9): p. 2718-2724.
31. Lindquist, N.C., et al., *Sub-micron resolution surface plasmon resonance imaging enabled by nanohole arrays with surrounding Bragg mirrors for enhanced sensitivity and isolation.* Lab on a Chip, 2009. **9**(3): p. 382-387.
32. McDonald, J.C., et al., *Fabrication of microfluidic systems in poly(dimethylsiloxane).* Electrophoresis, 2000. **21**(1): p. 27-40.
33. Oh, B.K., et al. *Immunosensor for detection of Legionella pneumophila using surface plasmon resonance*. 2003: Elsevier Advanced Technology.

Figures

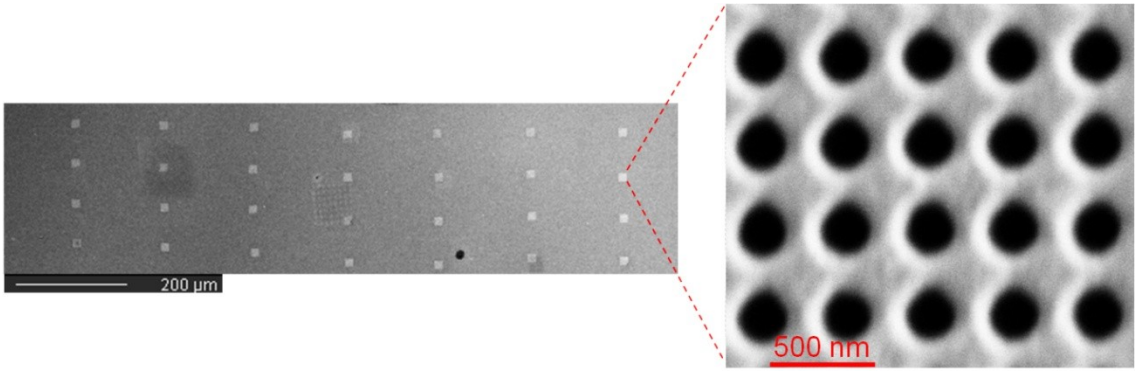

Figure 1. Scanning electron microscope images of the fabricated nanohole arrays via FIB milling through a gold film. The nanohole arrays were 420 nm in periodicity with holes of 200 nm in diameter. The arrays were arranged in 7 columns and 4 rows, spaced 150 µm and 60 µm respectively.

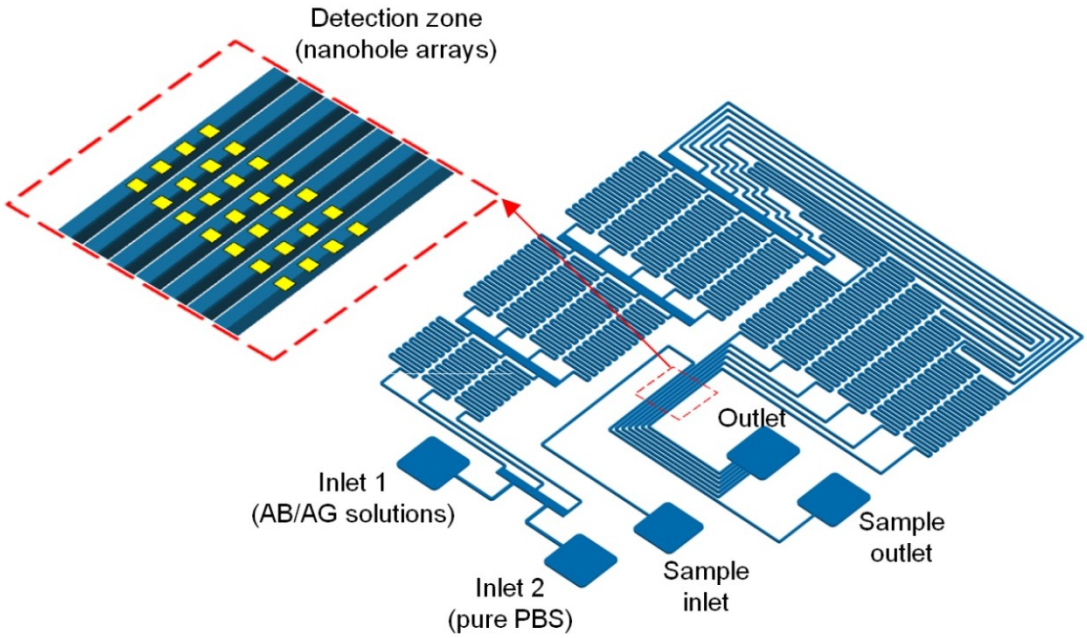

Figure 2. Schematics of the microfluidic chip used to generate the concentration standard curve and to measure the analyte concentration of the biomarker in real-time operation. PBS and AB/AG solutions were infused at the inlets and diluted to generate 6 different concentrations at the outlet microchannels. An independent microchannel is used to flow a sample with unknown

concentration of analyte. The nanohole arrays are aligned with the microchannels at the detection zone.

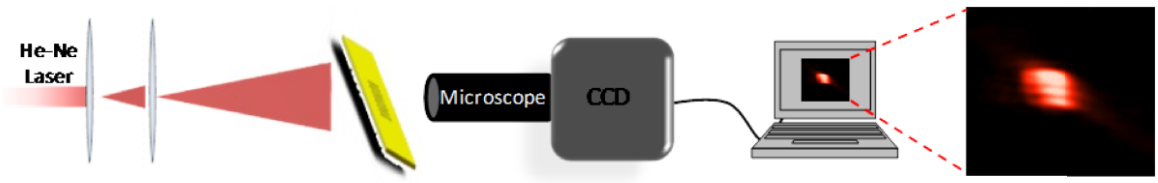

Figure 3. Schematics of the experimental setup used for SPR imaging acquisition.

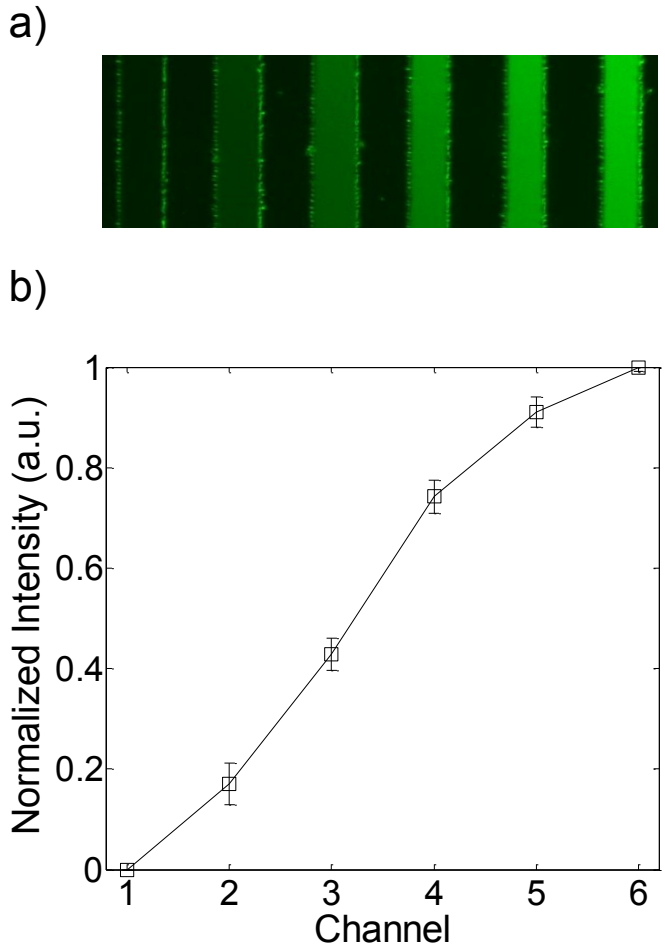

Figure 4. Fluorescence microscopy characterization of the microfluidic concentration gradient generator. a) Fluorescence image at the 6 outlet channels, demonstrating the generation of a

fluorescein concentration gradient. One inlet of the microfluidic chip was supplied with pure PBS while the other inlet was supplied with 1 mM fluorescein PBS. b) Normalized average fluorescence intensities of each channel over an area of 20 by 20 pixels.

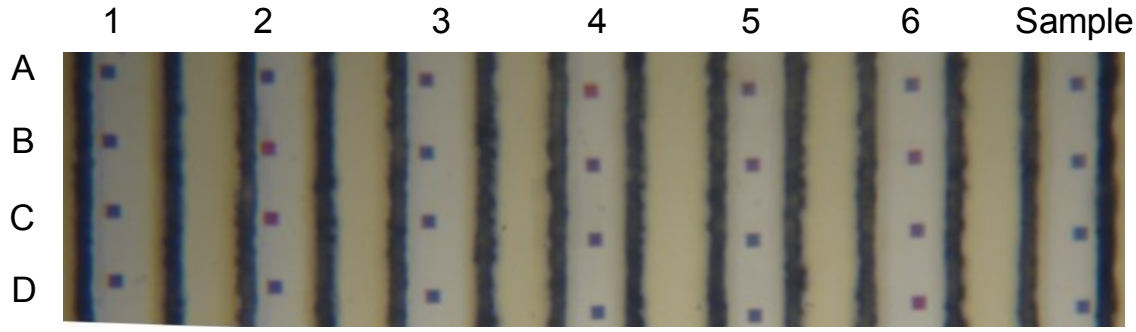

Figure 5. Picture of the nanohole arrays aligned with the outlet channels of the microfluidic chip.

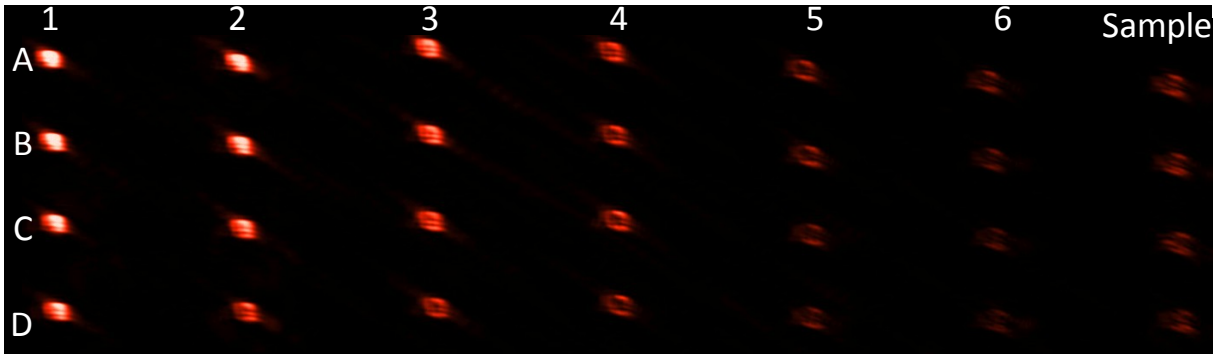

Figure 6. SPR image of the sensing platform operating under the microfluidic concentration gradient generation scheme. The picture was acquired with a CCD camera and shows the intensity variation of the transmitted light from the nanohole arrays modified with PAX8.

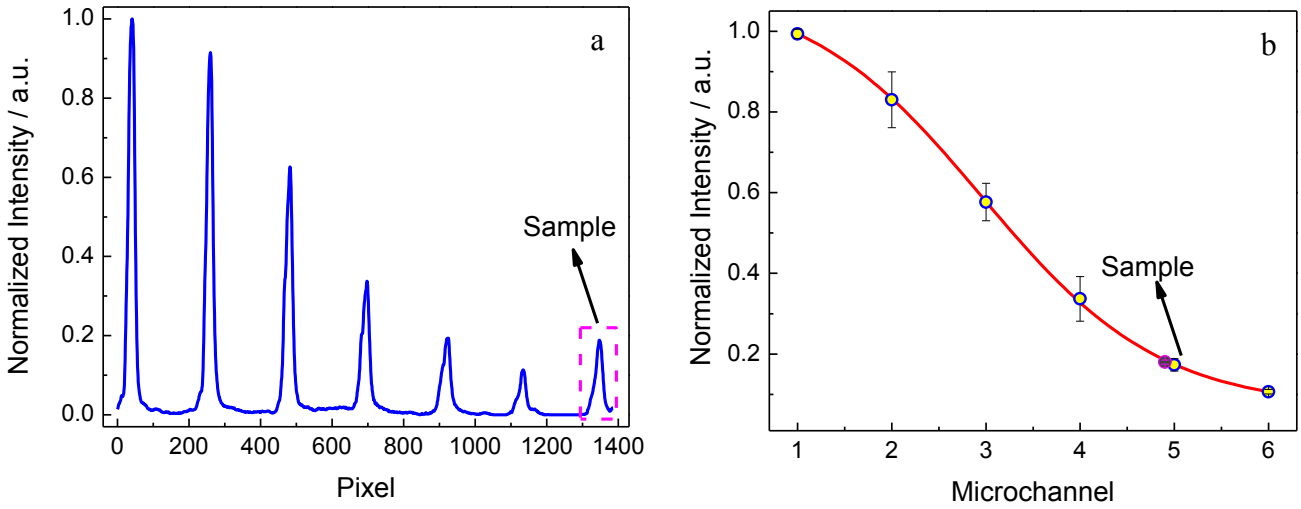

Figure 7. a) Normalized intensities for row B after flowing PAX8 solution. b) Average calculated to the arrays in each microchannel. A Sigmoidal equation was used to fit the curve.

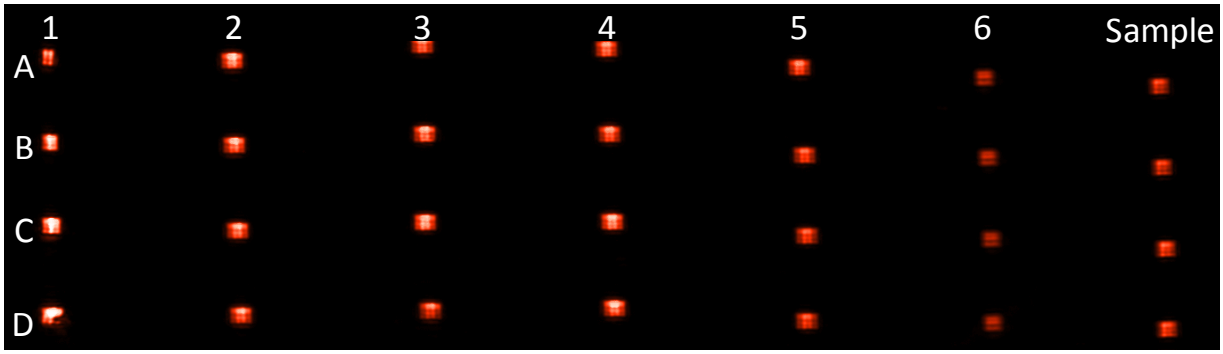

Figure 8. CCD image of the arrays aligned with the microfluidic chip. The arrays were previously modified with PAX8 and the antigen solution (r-PAX8) was diluted over the sample (from column 6 to 1). R-PAX8 solution of "unknown" concentration flowed over the last column (at right side).

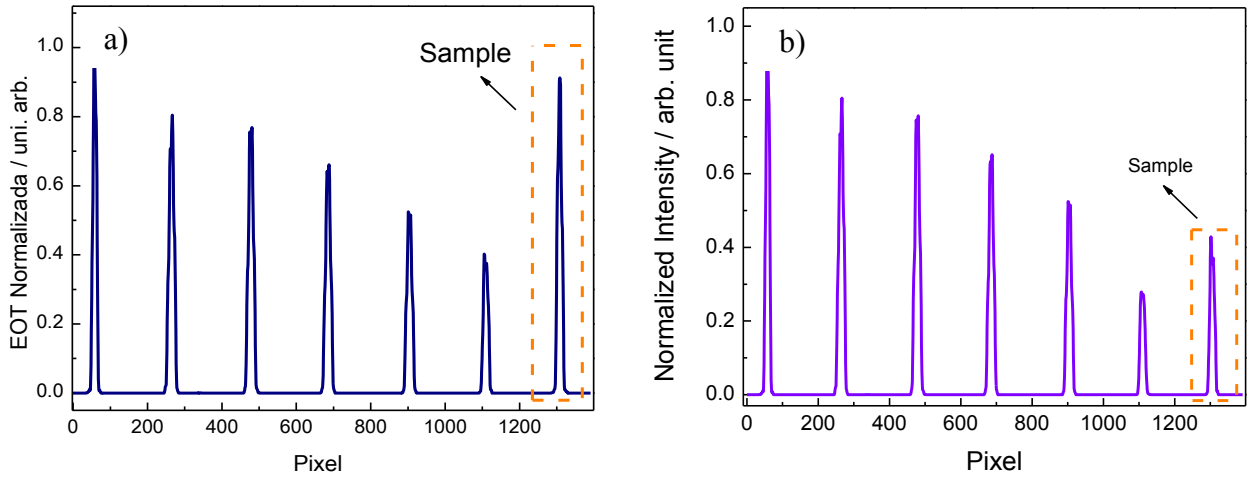

Figure 9. Normalized Intensities for row B after flowing r-PAX8 (antigen) solution. A microchannel parallel to the dilution chip was used to detect the antigen in a solution of unknown concentration. a) Detection of r-PAX8 in a diluted solution and b) in a concentrated solution.

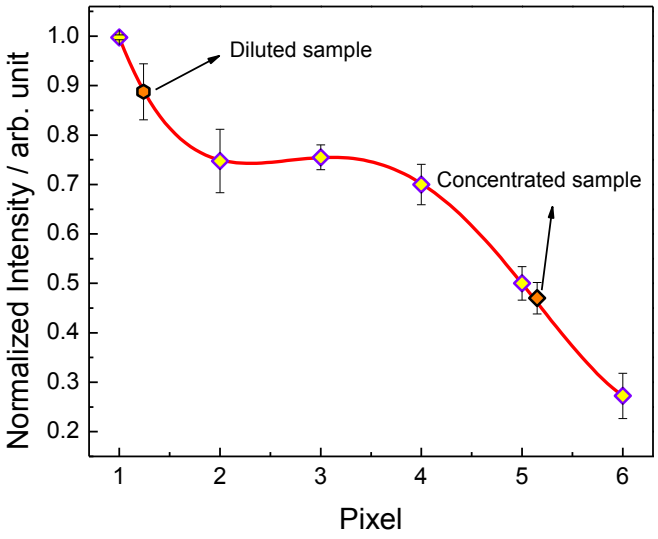

Figure 10. Average calculated to the normalized intensities for all the arrays inside each microchannel. A 4th order polynomial was used to fit the curve.

Appendix F

Microfluidic Liquid Actuation through Ground-Directed Electric Discharge

Microfluid Nanofluid
DOI 10.1007/s10404-011-0831-4

RESEARCH PAPER

Microfluidic liquid actuation through ground-directed electric discharge

Carlos Escobedo · David Sinton

Received: 7 April 2011 / Accepted: 3 June 2011

Abstract In this article, we present a new technique to actuate liquids in microchannels using ground-directed electric discharge generated by a portable corona device. When an electric discharge is applied, the air in the microchannel is ionized causing a change in the surface energy. The resulting change in the contact angle induces rapid liquid transport through the channel by capillary action. In contrast to established plasma treatment this method employs a ground electrode that guides the electric field. This approach enables rapid treatment of select microchannels and thus provides a means of real-time fluid actuation as opposed to simply a pretreatment process. Instantaneous fluid velocities show power-law dependence with time and fit theoretical models at a contact angle of 65°. Average fluid velocities are on the order of 5 cm/s, and thus channels on the order of 1-cm long are filled in ~ 0.2 s. To demonstrate the potential of this technique for integrated lab-on-a-chip applications, the method was employed in serpentine channel, for on-demand fluid routing, to initiate a mixing process, and through an on-chip integrated microelectrode.

Keywords Electric discharge · Plasma · Microfluidic · Nanofluidic · Contact angle · Capillary flow · Surface tension · Microfluidic liquid actuation · Corona

Electronic supplementary material The online version of this article (doi:10.1007/s10404-011-0831-4) contains supplementary material, which is available to authorized users.

C. Escobedo · D. Sinton (✉)
Department of Mechanical Engineering, University of Victoria, P.O. Box 3055, STN CSC, Victoria, BC V8W 3P6, Canada
e-mail: dsinton@me.uvic.ca

1 Introduction

A central advantage of microfluidics is the potential to integrate complex analytical functions (Thorsen et al. 2002; Whitesides 2006). Achieving this integration requires real-time fluid control, or actuation, on the scale of individual channels. Existing methods for real-time flow control in an integrated chip include multilayer elastomeric switching valves (Unger et al. 2000), electrokinetic control with integrated electrodes (Horiuchi and Dutta 2006), burst valves for centrifugal microfluidics (Juncker et al. 2002; Kim et al. 2008), and electro-wetting for droplet systems (Fair 2007; Luk and Wheeler 2009). While the simplicity of capillary-valve-based flow control is attractive, it is not possible to dynamically alter the order or timing of fluidic operations.

Surface treatment is commonly required to increase the wetting properties of microfluidic systems to enable filling. One of the most commonly used materials, poly(dimethylsiloxane) (PDMS), is natively hydrophobic and can be rendered hydrophilic by exposure to oxygen plasma (Makamba et al. 2003). Plasma is a particular phase of matter, commonly referred to as ionized gas, wherein gas particles are electrically charged. Plasma can be artificially produced in air around an electrode at sufficiently high potential gradients. Due to the conductive nature of plasma, an electric discharge may occur within the ionized gas cloud (Bittencourt 2004). Exposure to plasma introduces polar groups on the polymer surface resulting in an increase in surface wettability. A natively hydrophobic polymeric surface thus becomes wettable after plasma exposure (Sun et al. 1999; Zenkiewicz 2005). Most commonly, this is achieved prior to chip bonding by exposing the entire chip surface to plasma under vacuum in a plasma oven. An alternative to the oven-based treatment was

Published online: 15 June 2011

presented by Haubert et al. (2006) where a low cost handheld corona discharge device was applied. The device produces a high voltage (10–50 kV) at 4–5 MHz, ionizing the atmospheric pressure air around the electrode which enabled instantaneous oxidation of the proximate chip surface (Zenkiewicz 2005; Thorslund and Nikolajeff 2007).

Active flow control of gases has been achieved using electric discharges in MEMS devices (Hsu et al. 2007). The phenomenon is usually referred to as ionic wind and has been studied since the eighteenth century (Robinson 1962; Kim et al. 2000; Sung Kwon et al. 2003; Chih-Peng et al. 2007). The electric field strength on a sharply shaped electrode exceeding a certain threshold results in the local ionization of the air. The ionized air molecules emerge as a pale purple cloud and have the same electric charge as the electrode. Charge repulsion results in the expansion of the ionized air cloud away from the conductor, creating a net gas flow (Hilpert and Kern 1974). However, this form of flow actuation using an electric discharge is exclusive to gases (Moreau 2007).

For liquid flows in microfluidics, localized treatment of microfluidic structures has been achieved using corona devices (Evju et al. 2004; Zenkiewicz 2005; Thorslund and Nikolajeff 2007). Localized treatment is enabled by the inherent confinement of the electric field around the electrode (Hilpert and Kern 1974; Seimandi et al. 2009). Additionally, electrohydrodynamic flows generated by corona discharge devices have been used for the promotion of microvortices for mixing and particle trapping (Yeo et al. 2006) and for microfluidic blood plasma separation (Arifin et al. 2007). These previous works demonstrate the ability to locally treat microchannel surfaces using electric discharges from a corona device.

In this article, we demonstrate ground-directed electric discharge that enables rapid treatment of select microchannels, providing a means of real-time fluid actuation. The method is characterized through one- and two-dimensional channel flow experiments, and comparison with mathematical models. To demonstrate applicability to integrated lab-on-chip systems, selective liquid routing and the actuation of a mixing process are demonstrated, as is the application of the technique using an integrated microelectrode. In contrast to previous pretreatment methods, this technique enables the direct control, routing, and actuation of microfluidic flows in real time.

2 Theoretical background

Figure 1 shows a schematic representation of microfluidic liquid actuation through ground-directed electric discharge. A basic configuration with a closed all-PDMS microchannel, a corona electrode and a ground electrode is shown in the schematics of Fig. 1a, b.

Two analytical models outlined below are applied in the analysis of the experimental results. The Hagen–Poiseuille equation for laminar flow can be expressed as:

$$Q = \frac{\mathrm{d}V}{\mathrm{d}t} = \left(\frac{\pi R^4}{8\eta}\right)\left(\frac{p_0 - p_{\mathrm{int}}}{l}\right) \tag{1}$$

where Q is the flow rate, V is the volume, t is the time, R is the hydrodynamic radius of the microchannel, η is the dynamic viscosity of the liquid, p_0 is the liquid pressure at the entrance of the microchannel, p_{int} is the liquid pressure at the meniscus, and l is the distance from the microchannel

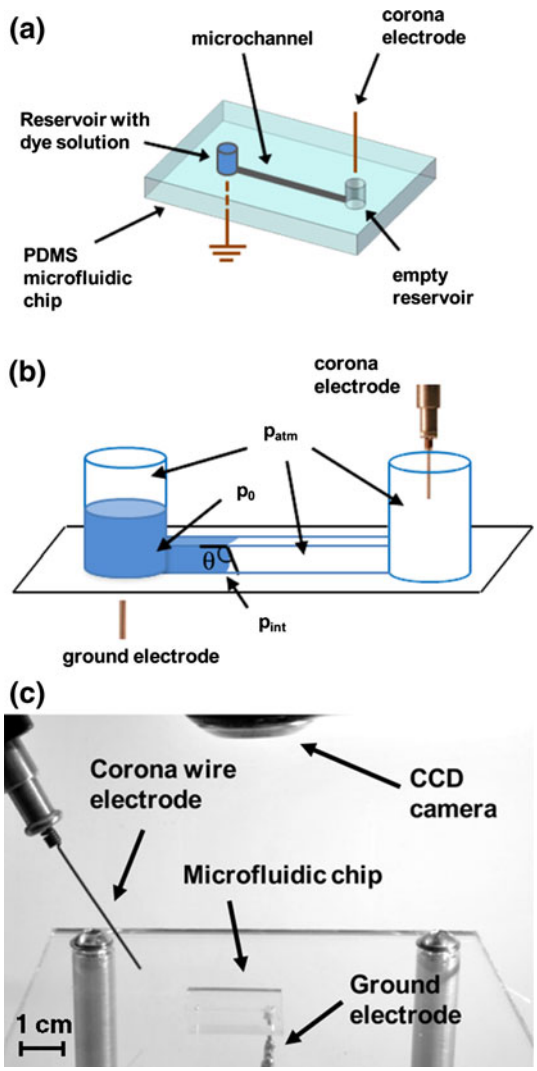

Fig. 1 The ground-directed electric discharge liquid actuation setup. **a** Schematic showing the corona electrode is placed in one of the reservoirs and a ground electrode is placed under the second reservoir containing solution, **b** diagram showing the geometry and parameters relevant to the system, and **c** image of the experimental setup. The acrylic working surface had a 2-mm circular opening for ground electrode access

inlet to the air–liquid interface, or penetration length. The capillary pressure is defined by the Young–Laplace equation as:

$$p_{\text{atm}} - p_{\text{int}} = \frac{2\sigma}{R}\cos\theta \tag{2}$$

where p_{atm} is the atmospheric pressure, σ is the surface tension, and θ is the liquid–gas interface contact angle at the solid. Substituting Eq. 2 in 1 and rearranging the terms the following expression is obtained:

$$\frac{2\sigma}{R}\cos\theta = \left(\frac{8\eta}{R^2}\right)\left(\frac{\mathrm{d}l}{\mathrm{d}t}\right) + (p_{\text{atm}} - p_{\text{int}}) \tag{3}$$

If θ is considered constant, Eq. 3 is an ODE and can be integrated by separation of variables:

$$l = f(t) = \left[\left(\frac{R\sigma\cos\theta}{2\eta}\right) + \left(\frac{\mathrm{R}^2}{4\eta}\right)(p_0 - p_{\text{atm}})\right]^{\frac{1}{2}}(t)^{\frac{1}{2}} \tag{4}$$

and can be rearranged as:

$$\cos\theta = \left(\frac{4\eta}{R\sigma}\right)\left[lu - \left(\frac{R^2}{4\eta}\right)(p_0 - p_{\text{atm}})\right] \tag{5}$$

where u is the instantaneous velocity of the air–liquid interface. Assuming hydrostatic pressure within the reservoir is negligible, Eq. 5 can be simplified to a form of the Washburn equation (Washburn 1921; Hilpert 2009) as follows:

$$l^2 = \frac{\sigma R t}{2\eta}\cos\theta \tag{6}$$

where l is the liquid penetration length.

For small time scales, however, the velocity predicted by Washburn equation approaches infinity as $t \to 0$. An alternative model was presented by Adams and White (2008) for surface-tension-driven flow in capillaries of arbitrary cross section. The liquid penetration length in the model by Adams and White for flows with wall friction is defined as:

$$l = \left\{2t_{\text{chr}}\left(\frac{p_0}{\rho} + \frac{2\sigma\cos\theta}{\rho R}\right)(t - t_{\text{chr}}[1 - \exp(-t/t_{\text{chr}})])\right\}^{\frac{1}{2}} \tag{7}$$

where ρ is the fluid density and t_{chr} is the characteristic time of the system provided by:

$$t_{\text{chr}} = \frac{\rho R}{C\mu} \tag{8}$$

where C is a constant depending on the geometry of the cross section of the microchannel (Adams and White 2008). Neglecting hydrodynamic effects, Eq. 7 can be differentiated with respect to time resulting in the following expression (Adams and White 2008):

$$u = u_{\text{chr}}\left(\frac{\sqrt{2t_{\text{chr}}}}{2}\right)\left[\frac{1 - \exp(-t/t_{\text{chr}})}{[t - t_{\text{chr}}(1 - \exp(-t/t_{\text{chr}}))]^{1/2}}\right] \tag{9}$$

where u_{chr} is a characteristic velocity defined as:

$$u_{\text{chr}} = \left(\frac{2\sigma\cos\theta}{\rho\mathrm{R}}\right)^{1/2} \tag{10}$$

For larger time scales and constant contact angles, Eq. 7 reduces to the Washburn equation (Adams and White 2008).

3 Experimental

3.1 Microfluidic chips

PDMS (Sylgard, Dow Corning Corporation, Midland, MI) chips were fabricated using the established soft lithography technique (Duffy et al. 1998; Whitesides and Stroock 2001). Five different chip designs were used in the experiments. The first chip design consisted of a 10-mm long straight channel. Two openings for fluidic and electrode access were punched at the ends of the microchannel. The second design consisted of a group of five straight channels with lengths of 10, 14, 18, 22, and 25 mm, separated 7 mm from each other. Each channel in this chip included two punched holes for electrodes and fluids access. The third design consisted of a serpentine microchannel with eight 90° elbows and a total channel length of 20 mm. The cross-sectional area of all the microchannels was 250 μm by 250 μm. A fourth design consisted on a star-shape microfluidic chip, having three 3.5-mm long microchannels converging into a single 7-mm long microchannel. The distal end of every microchannel was connected to a reservoir. The cross-sectional areas of all the microchannels in this design were 50 μm by 50 μm. The fifth chip design consisted of a Y-shape chip with two converging microchannels ending in a common single channel. The converging microchannels and the common outlet channel in this chip were 3.5 and 6.5 mm in length, respectively, and the microchannels were 50 μm by 50 μm. Thin PDMS layers were separately cast over a clean silicon wafer (Silicon Quest International, Santa Clara, CA). With the exception of the integrated microelectrode chip, all chips were irreversible bonded to a piece of the thin PDMS layer by oxygen plasma exposure. After bonding the chips were baked for at least 6 h at 85°C to ensure a uniform hydrophobic initial surface condition.

3.2 Dye solutions

Dye solutions for visualization experiments were prepared by diluting concentrated commercial brilliant blue (E133),

yellow (E102) and allura red (E129) food dyes (McCormick, Baltimore, MD) and ultrapure water (Millipore, Billerica, MA). The dye solutions were filtered with 0.45 μm PVDF membrane syringe-driven filters (Millipore, Billerica, MA) prior the experiments. The conductivity and pH of the resulting diluted dye solutions were measured using an Oakton Con 6 conductivity meter (Oakton Instruments, Vernon Hills, IL) and a pH5 Acorn series pH meter (Oakton Instruments, Vernon Hills, IL). The conductivities of the blue, yellow, and red solutions were 530, 480, and 510 μS/cm, respectively. The pH of all solutions was 7.5.

3.3 Integrated microelectrode

In order to demonstrate applicability of the method in integrated lab-on-a-chip applications, liquid actuation was achieved using an integrated microelectrode. Gold microelectrodes were fabricated using conventional gold wet etching technique as follows. A commercial glass slide with a 100-nm gold layer and a 5-nm chromium adhesion layer (EMF Corp., Ithaca, NY) was spin-coated with SU8-25 photoresist (MicroChem, Newton, MA). Next, the slide was prebaked at 65°C for 3 min and then baked at 95°C for 10 min. After cooling, a mask with the microelectrodes patterns was placed over the coated glass slide and exposed to UV light for 140 s, followed by post-bake steps at 65 and 95°C for 3 and 15 min, respectively. The photoresist pattern was developed using SU8 developer (MicroChem, Newton, MA). The slides were then placed in a gold etching solution made prior to the electrodes fabrication by mixing 8 g of KI and 2 g of I_2 in 80 ml of water. An 8% to 22% (v:v) solution of acetic acid to ceric ammonium nitrate was then used to remove the chromium adhesion layer. The remaining photoresist on top of the gold pattern was removed using Nano^{TM} Remover PG (MicroChem, Newton, MA) and IPA. A single conductor copper stranded 24-gauge wire (Pico Wire, Canada) was then connected to the microelectrode using conductive epoxy (MG Chemicals, Vancouver, BC, Canada).

3.4 Experimental setup

Figure 1a shows a schematic representation of the experimental setup. The experimental configuration, with a liquid inside the microchannel, a ground electrode underneath the inlet and the corona electrode in the outlet, is shown in Fig. 1b. Figure 1c shows a picture of the experimental setup used in this study. As shown in the picture, an electrically isolated working surface was used for the experiments. The surface was a 1/4-inch thick PMMA plate with a 2-mm diameter circular opening fixed to an optical table using four rods. The circular opening in the surface was used for ground electrode access. A corona handheld device (Electro-Technic Products Inc., Chicago, IL) which produces a voltage of 10–50 kV at 4–5 MHz was fixed to the optical table using a stand-rod holder. A Logitech Pro900 digital webcam (Logitech, Fremont, CA) and a Miro4 high-speed CCD camera (Vision Research, NJ) were used for video acquisition. A Nikon D60 digital SLR (Nikon, Tokyo, Japan) was used for still image acquisition. Figure 1c shows the experimental setup with the webcam. It is important to note that although the electrical current is limited, the electromagnetic field in the vicinity of the high frequency and high voltage electrode can disturb electronics and digital cameras in particular. For this reason, imaging at a distance was required. Specifically, 10 cm between the camera chip and the electrode was found to be sufficient while providing sufficient image data.

4 Results and discussion

4.1 Ground-directed electric discharge liquid actuation

Microfluidic liquid actuation through ground-directed electric discharge is enabled by a change in surface energy at the solid–liquid interface. The instantaneous surface oxidation caused by the plasma generated by the electric discharge results in a reduction of the liquid–gas interface contact angle at the solid. In a common sessile droplet system, the surface energy change caused by the electric discharge is manifested by a sudden and dramatic spreading of the droplet over the substrate. Figure 2 shows an ultrapure water droplet on a planar PDMS surface exhibiting a contact angle of 122° prior to exposure to the electric discharge. Following exposure the surface becomes highly wetting, exhibiting a contact angle approaching zero (<5°). The contact angles for each case were measured

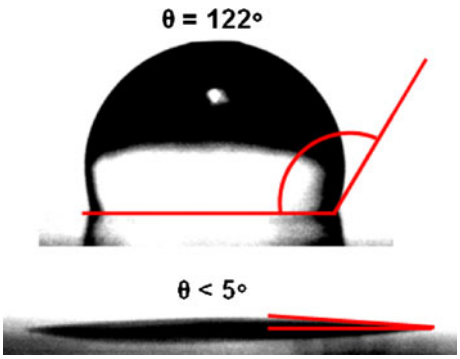

Fig. 2 Images of a nanopure water droplet on a flat PDMS surface prior and after the application of an electric discharge. The contact angles of the droplet-on-PDMS system were measured using low bond axisymmetric drop shape analysis, resulting in values of 122° for the initial condition and <5° after the surface treatment

using low bond axisymmetric drop shape analysis through Image J software.

Figure 3a presents the schematics of the first experimental configuration. A simple straight microchannel was employed. The inlet reservoir was filled with blue dye solution and the ground electrode was positioned underneath the inlet reservoir, within 1 mm of the bottom PDMS surface of the chip. The wire electrode from the corona device was placed in the outlet. The corona device was then started causing the ionization of the air surrounding the wire electrode. As shown schematically in Fig. 3a, an electric discharge and a distinctive glow from the air ionization is guided along the channel to the liquid interface, and exits the chip below the inlet reservoir to reach the ground electrode.

Figure 3b shows an image sequence of the experimental results. As shown, the directed electric discharge and subsequent surface energy change resulted in the rapid advance of the liquid along the microchannel (movie of this experiment is available in Online Resource 1). By $t = 0.006$ s following the application of the electric discharge, the liquid had advanced into the microchannel. As shown in the magnified portions inset in Fig. 3b, the initial wetting pattern mirrored the visualized electric discharge. The channel was half-filled by $t = 0.04$ s, and completely filled by 0.2 s representing an average velocity of ~ 7 cm/s.

Figure 4 shows the liquid velocity data determined from the imaging experiments and comparison with that predicted from the theoretical models. The liquid meniscus position was recorded with the high-speed CCD camera at 600 frames per second and a resolution of 800 by 600 pixels. Instantaneous velocities at different lengths along the microchannel were then calculated using a post-processing imaging software (Vision Research, NJ). These experimental results were compared with the two theoretical models described in Sect. 2, using Eqs. 6 and 9. The value of contact angle in each theoretical model was used as a fitting parameter to compare with the experimental data. Both the scaling exponent and the constant from the power law curve trend from the theoretical models were used to obtain the best fit to the experimental data for a given contact angle. The Washburn model, Eq. 6, and the model presented by Adams, Eq. 9, show a best fit at a contact angle of 65°. As expected from theory, the velocity of the liquid front reduces as it penetrates the microchannel and shows a power law dependence on time. The theoretical models and experimental data agreed within 5% for each case. This agreement suggests the PDMS surfaces had uniform wetting conditions prior to testing. It is important to note that the post-treatment surface conditions in the channel are different than those for the sessile droplet discussed above. Differences in the treatment are primarily due to the variations in field intensity and geometry in the two cases. It was not possible to get highly accurate direct measurements of the contact angle in the channels due to imaging artifacts. However, the observed contact angles are in line with those determined from the resulting transport. Also, the most important measure of surface treatment, in the context of this work, is the extent to which transport is enabled in the microchannel.

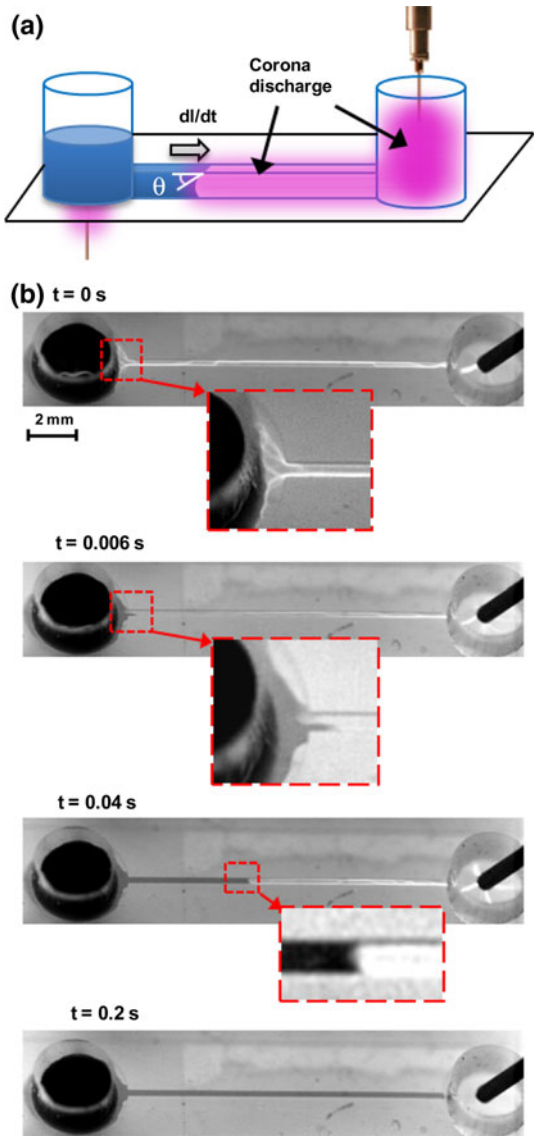

Fig. 3 **a** Schematic showing the path of a ground-directed electric discharge. After the electric discharge application, the PDMS surface becomes wetting, enabling the transport of the liquid through the microchannel by capillary action. **b** Images of an experiment demonstrating microfluidic actuation through ground-directed electric discharge. The selected pictures are part of a sequence acquired at 600 frames per second using the high-speed camera. The electric discharge is observed as it travels along the microchannel walls, ionizing the air inside, treating the surface, and subsequently enabling liquid transport. Details at the liquid–gas interface are shown *inset*. A movie of the experiment is available in Online Resource 1

The dependence of the surface treatment on the length and the power of the corona discharge device are investigated in the following sections.

4.2 Influence of channel length

The dependence of the length of channel over which the electric discharge is applied was investigated using the chip with five parallel straight microchannels, as shown in Fig. 5. The inlets of each of the micro-channels were filled with dyed solution. The ground electrode was placed at the inlet and the wire electrode from the corona device at the outlet. An electric discharge, lasting approximately 0.2 s, was applied to each of the channels at a time. Liquid actuation was achieved only in the three shorter micro-channels, as shown in Fig. 5. Under these conditions, the maximum length for achieving liquid actuation was found to be 18 mm. Importantly, longer lengths may be achieved at higher power intensities or longer applications of the electric discharge. However, these results show that sub-second applications of discharges, at the relatively low power intensities used here can actuate fluids over length-scales on the order of $\sim$1 cm. The influence of power intensity is considered below.

4.3 Influence of power intensity

The influence of the electric discharge power intensity on the fluid velocity was investigated. Figure 6 shows the total average velocities as a function of power intensity. The length of the microchannels used in this experiment was 18 mm and the cross section was 250 μm × 250 μm. Due to the lack of a quantitative power indicator in the portable

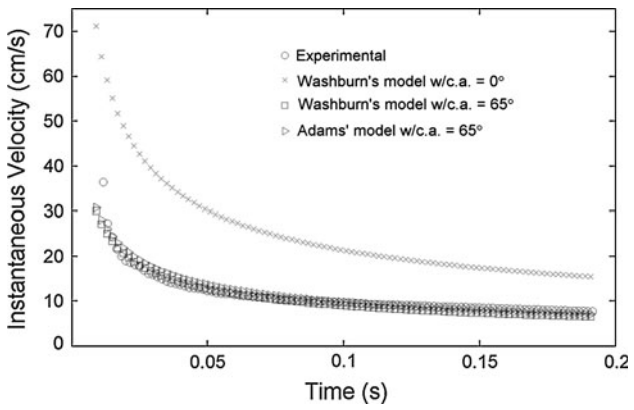

Fig. 4 Instantaneous velocities achieved through electric-discharge-induced flow. Theoretical models are used to fit the experimental data collected through imaging (in Fig. 3). Both models exhibit a best fit at a contact angle is 65°. The microchannel used in the experiment was 14 mm in length

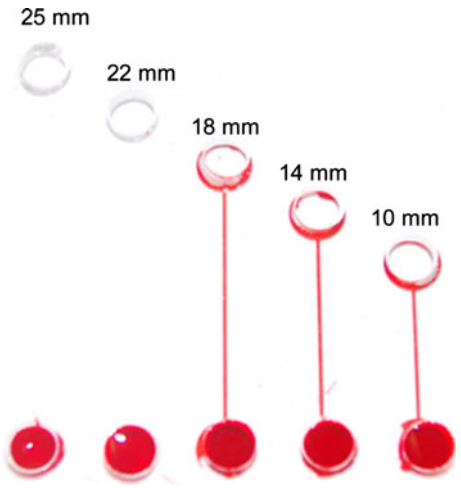

Fig. 5 Influence of channel length in ground-directed electric discharge liquid actuation. A fixed power intensity level was applied in five microchannels with lengths indicated. Liquid actuation was achieved in the three shorter microchannels, suggesting the spatial treatment is limited at a given power intensity and duration

corona device used in this study, a relative power intensity level scheme was required. The power levels were set by turning increments of 45° on the knob from a set base position. The total average velocity of the liquid transported through the channel was calculated using visualization techniques with the experimental setup shown in Fig. 1c. Figure 6a shows the average velocities at different relative power levels. The average liquid flow velocity increased linearly with the power intensity, however, relatively little change ($\sim$20%) was observed over the full scale of powers tested. Figure 6b shows the average effective contact angle, calculated from Washburn's equation using the observed velocities, as a function of power intensity. As shown, the contact angle resulting from the treatment decreases linearly with power intensity. As the power increases, the average effective contact angle decreases at a rate of $\sim$0.73° per relative intensity level. Although the simple knob adjustment on the device is not quantitative, these results indicate that once ground-directed discharge is achieved, differences in surface condition achieved with further increasing power through this control are negligible. That is, a sufficient power setting was required to initiate the discharge, and further increases in the power setting of the device showed little change in the resulting treatment and flow actuation.

4.4 Application in non-straight microchannels

Microfluidic chip applications rarely involve exclusively straight microchannels. Figure 7 shows the application of ground-directed electric discharge liquid actuation to a serpentine channel structure. The experimental setup and

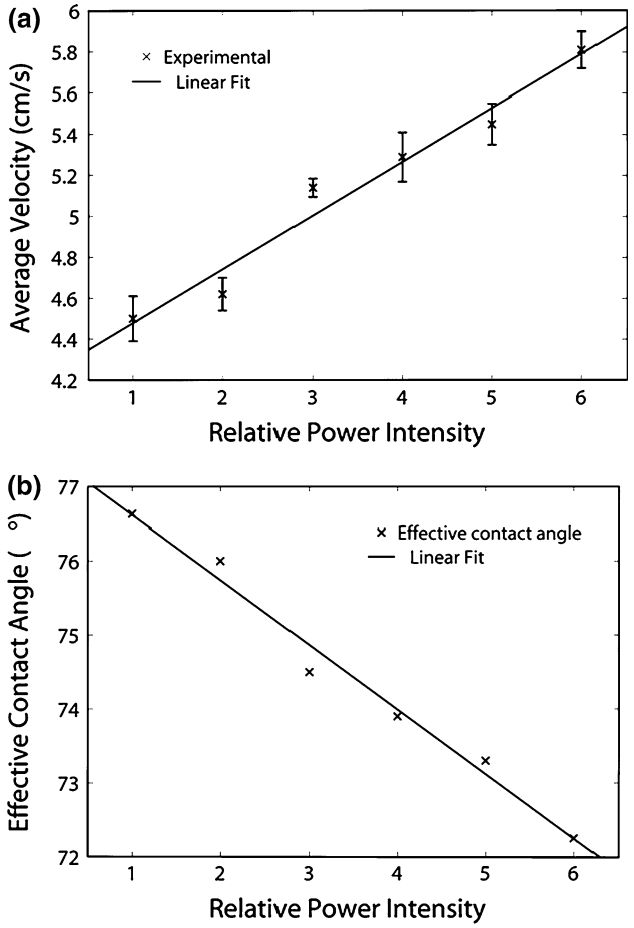

Fig. 6 **a** Average liquid velocities as a function of relative power intensity. The intensity was increased by advancing the knob of the handheld corona device 45° at each level. **b** Corresponding effective contact angle obtained by fitting the experimental data to the Washburn theoretical model

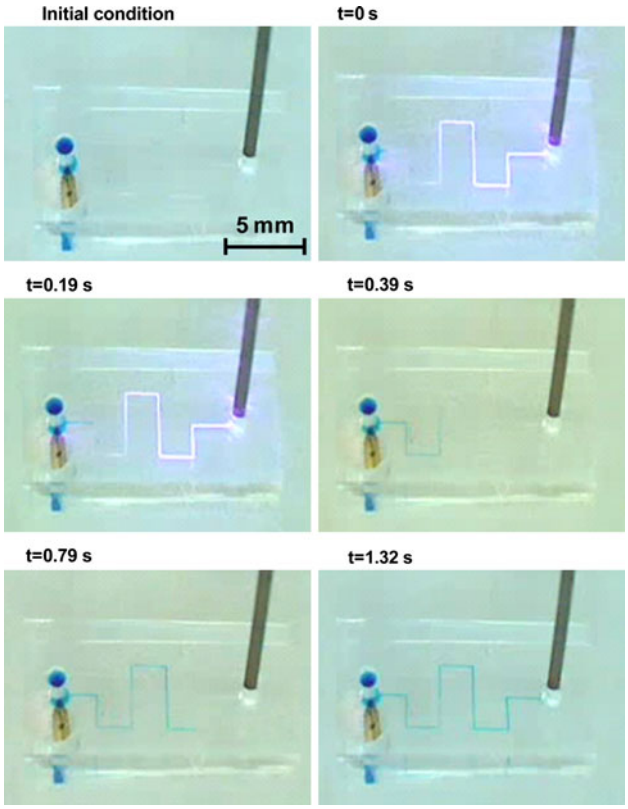

Fig. 7 Ground-directed electric discharge liquid actuation in a non-straight microchannel. The channel has eight 90° elbows and a total length of 20 mm. The discharge provided sufficient surface treatment to initiate flow back to the outlet in ~1.3 s. A movie of the experiment, at 0.25× speed, is available in Online Resource 2

experimental procedures were otherwise similar to those employed previously. As visualized in the images in Fig. 7, the electric discharge followed the channel through eight 90° turns in a relatively long (2 cm) channel, and provided sufficient surface treatment to initiate flow back to the outlet. A movie of this experiment is available in Online Resource 2. The time required from the initiation of the discharge to the completed filling of the channel was approximately 1.3 s. The results clearly indicate that this method is readily applicable to non-straight microchannel geometries.

4.5 Application in liquid routing

Figure 8a shows a schematic representation of the star-shaped chip design used to demonstrate directed sequential liquid routing, through ground-directed electric discharge. In this experiment, the ground electrode was placed at the divergence point, underneath the bottom PDMS layer of the hydrophobic microfluidic chip. The corona electrode was placed successively at each reservoir of the chip to route the liquid through each corresponding channel. Figure 8b shows the image sequence of the liquid routing experiment. The first electric discharge, applied at the inlet, resulted in liquid actuation along the microchannel with a penetration length equal to the distance between electrodes. Two aspects are noteworthy here: this actuation configuration is opposite that shown in the previous figures as the discharge is applied to the liquid directly and then directed through the channel; and no liquid transport in the other three microchannels resulted from this discharge. The corona electrode was then placed at an outlet and a second discharge was applied. This application resulted in the preferential transport of the liquid along the corresponding microchannel, linking the reservoir to the inlet reservoir. The third and fourth discharges routed fluid from the intersection to the remaining outlet reservoirs. A movie of experiment is available in Online Resource 3. The individual channel actuation achieved in this experiment demonstrates the potential of the ground-directed electric

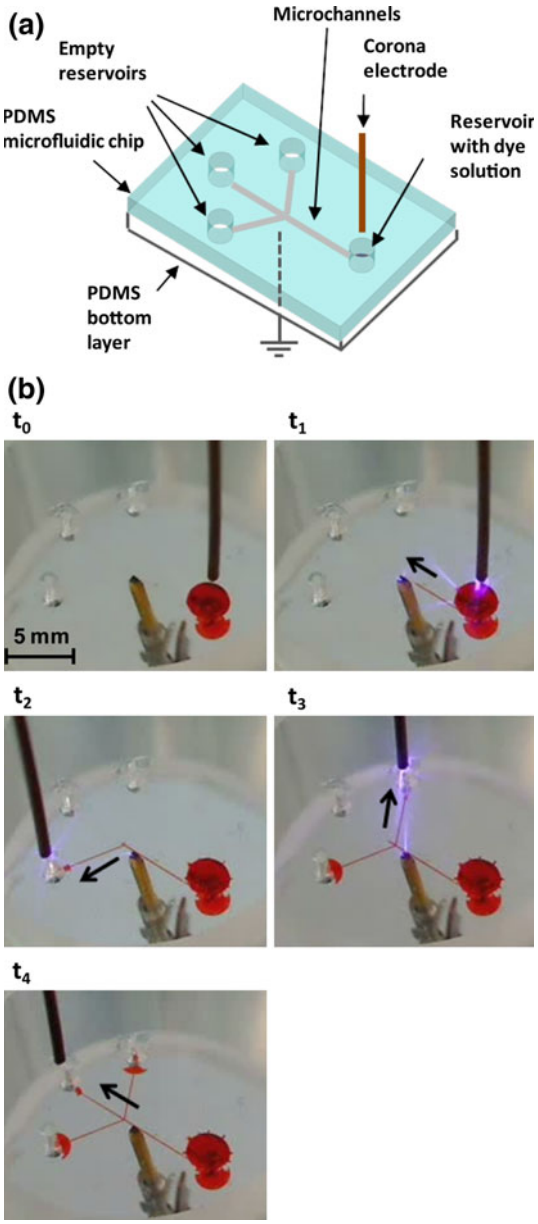

Fig. 8 Application in liquid routing. **a** Schematic representation of the star-shaped microfluidic configuration used in the experiment. The ground electrode was placed below the chip at the divergence point. **b** Image sequence of the experiment. The electric discharge was applied successively at each reservoir of the chip to route the liquid through each corresponding channel. A first discharge, applied at the inlet, resulted in liquid actuation along the microchannel with a penetration length equal to the distance between electrodes (this application of discharge at the liquid reservoir is opposite that of Fig. 1). A second discharge applied at an outlet reservoir resulted in the preferential transport of the liquid along the corresponding microchannel, linking that reservoir to the inlet reservoir. The third and fourth discharges routed fluid from the intersection to the remaining outlet reservoirs. A movie of experiment is available in Online Resource 3

discharge actuation technique for controlled preferential routing of liquid samples in complex microfluidic systems and lab-on-a-chip devices.

4.6 Ground-directed electric discharge liquid actuation to initiate solution mixing

Figure 9 shows the Y-shape chip and experimental configuration used in a mixing process initiated through ground-directed electric discharge liquid actuation. Figure 9a shows the initial configuration, having one inlet filled with yellow dye solution and the second inlet with blue dye solution. The ground electrode was placed underneath the bottom PDMS layer of the chip, at the channels' intersection, while the corona electrode was placed at the outlet. Figure 9b shows the results of the mixing process initiated by the electric discharge. After a discharge was applied, both dye solutions flowed through their respective channels to the intersection, and mixed on the way to the outlet reservoir, as indicated by the green hue in the channel and outlet. It is noteworthy that in this case, the treated region reached beyond the ground-directed channel sufficiently to induce wetting in both adjacent 3-mm channels. This was achieved by applying a higher power discharge over a longer period (6, >1 s). The residence length for diffusive mixing for this flow rate was on the order of $\sim$3 mm, and the mixing channel length was 6 mm. This experiment demonstrates completion of an individual unit operation relevant to lab-on-chip applications. To integrate many such operations on a chip, delivery of the actuation via integrated microelectrodes would be required, and is demonstrated next.

4.7 Ground-directed electric discharge liquid actuation with an on-chip integrated microelectrode

Figure 10 shows the gold microelectrode fabricated on a gold-on-glass substrate, using a wet etching technique (as described in the experimental section). The resulting microelectrode had a 4-mm long tip with average width of 70 μm. A single-channel microfluidic chip was placed over the glass substrate, having one of the reservoirs, the outlet, positioned over the tip of the microelectrode. The inlet was filled with blue dye solution and the ground electrode placed underneath the glass substrate. A discharge was remotely applied to the microelectrode via a 24-gauge wire resulting in the liquid transport of the dye solution through the microchannel, as shown in Fig. 10 (movie of experiment is available in Online Resource 4). The liquid reached the outlet after 0.4 s, resulting in an average fluid flow velocity of 4.7 cm/s, in agreement with results achieved using the handheld corona device directly. This experiment demonstrates the flexibility of the ground-directed electric discharge liquid actuation technique and its potential for on-chip integration. Additionally, wetting-based techniques are applicable to a range of fluids of interest in microfluidic systems. Most

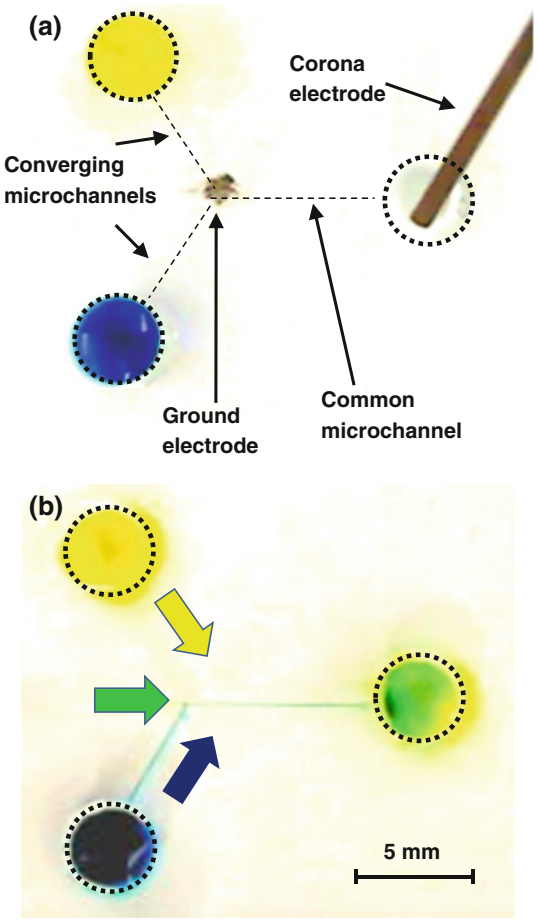

Fig. 9 Ground-directed electric discharge liquid actuation to initiate solution mixing. **a** The two inlets in the Y-shape chip were filled with *light* (shown *yellow* online) and *dark* (shown *blue* online) dye solutions. The ground electrode was placed underneath the intersection from the converging channels, and the corona device electrode was placed at the outlet. **b** Image of the resulting liquid mixing process initiated by electric discharge liquid actuation. After an electric discharge was applied, both dye solutions flowed through their respective channels to the intersection, and mixed on the way to the outlet reservoir, as indicated by the intermediate hue (shown *green* online) in the channel and outlet

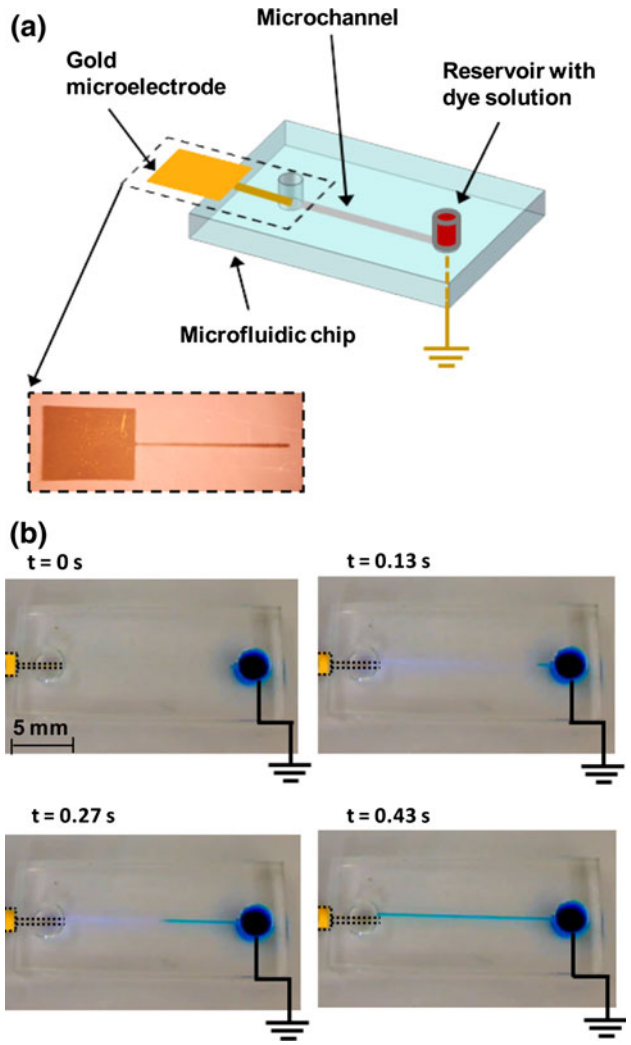

Fig. 10 Ground-directed electric discharge liquid actuation with an on-chip integrated microelectrode. **a** Schematic representation of the single-channel microfluidic chip with an integrated gold microelectrode used in the experiment. The tip of the microelectrode was 4 mm in length and had a width of ~70 µm. The outlet reservoir was filled with dye solution and a ground electrode was placed underneath, as previously. A picture of the microelectrode is shown as an *inset*. **b** Sequence of images showing electric discharge liquid actuation with an integrated microelectrode. The liquid reached the outlet after 0.4 s, resulting in an average fluid flow velocity of 4.7 cm/s, in agreement with results achieved using the handheld corona device directly. A movie of the experiment is available in Online Resource 4

notably, the ability to direct fluids using on-chip electrodes presents opportunities to achieve highly multiplexed, programmable fluidic functions through this technique. It is also important to note that, for applications in the biomedical field, we foresee minimal damage to biological samples as the field is chiefly applied to the gas in the microfluidic system, and as the field application time is very short. The relatively simple control methods developed here have potential to be integrated at high density to provide for much more complicated functions. Analogously, relatively simple pneumatically actuated microfluidic valve structures have enabled a vast array of complex on-chip processes.

5 Conclusions

In this study, a novel liquid actuation technique using a ground-directed electric discharge was demonstrated. High-speed visualization analysis of discharge-induced liquid flows in straight microchannels indicated velocities up to 7 cm/s. Two theoretical models were used to fit the experimental data, finding a best fit at a contact angle of 65°. Fluid flow velocities exhibited a linear dependence on microchannel length. The increase in power setting of the

device showed a minimal change in the resulting treatment and flow actuation. We found that longer lengths may be achieved at higher intensities or longer exposure times. Together these results show that sub-second applications can actuate fluids over length-scales on the order of $\sim$1 cm. The average liquid flow velocities were found to increase linearly with the power intensity, with average flow velocities in the order of $\sim$5 cm/s. The potential of this technique for integrated lab-on-a-chip applications was also demonstrated by application in a serpentine channel structure, for on-demand fluid routing, to initiate a mixing process, and through an on-chip integrated microelectrode. Still, when these demonstrations involve basic fluidic actuation and routing, the combination, integration, and multiplexing of these operations may be used to achieve applications with higher level of complexity. The applications shown here demonstrate the ability to complete and control individual unit operations relevant to lab-on-chip applications in diverse microchannel geometries, and to effectively direct fluids to achieve highly multiplexed, programmable fluidic functions.

Acknowledgments The authors would like to acknowledge funding from the Canada Research Chairs Program as well as a scholarship to CE and a research grant to DS from the Natural Science and Engineering Council of Canada (NSERC). Infrastructure funding from the Canadian Foundation for Innovation is also gratefully acknowledged. The authors would also acknowledge helpful discussions with Te-Chun Wu.

References

Adams TM, White AR (2008) Macroscopic conservation equation based model for surface tension driven flow. Adv Fluid Mech Vii 59:133–141

Arifin DR, Yeo LY, Friend JR (2007) Microfluidic blood plasma separation via bulk electrohydrodynamic flows. Biomicrofluidics 1(1):014103–014113

Bittencourt JA (2004) Fundamentals of plasma physics. Springer, New York

Chih-Peng H, Jewell-Larsen NE, Krichtafovitch IA, Montgomery SW, Dibene JT, Mamishev AV (2007) Miniaturization of electrostatic fluid accelerators. J Microelectromech Syst 16(4): 809–815

Duffy DC, McDonald JC, Schueller OJA, Whitesides GM (1998) Rapid prototyping of microfluidic systems in poly(dimethylsiloxane). Anal Chem 70(23):4974–4984

Evju JK, Howell PB, Locascio LE, Tarlov MJ, Hickman JJ (2004) Atmospheric pressure microplasmas for modifying sealed microfluidic devices. Appl Phys Lett 84(10):1668–1670

Fair RB (2007) Digital microfluidics: is a true lab-on-a-chip possible? Microfluid Nanofluid 3(3):245–281

Haubert K, Drier T, Beebe D (2006) PDMS bonding by means of a portable, low-cost corona system. Lab Chip 6(12):1548–1549

Hilpert M (2009) Effects of dynamic contact angle on liquid infiltration into horizontal capillary tubes: (Semi)-analytical solutions. J Colloid Interface Sci 337(1):131–137

Hilpert J, Kern J (1974) Electric wind in a corona discharge—theory and measurement. Arch Elektrotech 56(1):50–54

Horiuchi K, Dutta P (2006) Electrokinetic flow control in microfluidic chips using a field-effect transistor. Lab Chip 6(6):714–723

Hsu CP, Jewell-Larsen NE, Krichtafovitch IA, Montgomery SW, Dibene JT, Mamishev AV (2007) Miniaturization of electrostatic fluid accelerators. J Microelectromech Syst 16(4):809–815

Juncker D, Schmid H, Drechsler U, Wolf H, Wolf M, Michel B, de Rooij N, Delamarche E (2002) Autonomous microfluidic capillary system. Anal Chem 74(24):6139–6144

Kim J, Chaudhury MK, Owen MJ (2000) Hydrophobic recovery of polydimethylsiloxane elastomer exposed to partial electrical discharge. J Colloid Interface Sci 226(2):231–236

Kim J, Kido H, Rangel RH, Madou MJ (2008) Passive flow switching valves on a centrifugal microfluidic platform. Sens Actuators B 128(2):613–621

Luk VN, Wheeler AR (2009) A digital microfluidic approach to proteomic sample processing. Anal Chem 81(11):4524–4530

Makamba H, Kim J, Lim K, Park K, Hahn JH (2003) Surface modification of poly(dimethylsiloxane) microchannels. Electrophoresis 24(21):3607–3619

Moreau E (2007) Airflow control by non-thermal plasma actuators. J Phys D 40(3):605–636

Robinson M (1962) A history of electric wind. Am J Phys 30(5):366

Seimandi P, Dufour G, Rogier F (2009) An asymptotic model for steady wire-to-wire corona discharges. Math Comput Model 50(3–4):574–583

Sun C, Zhang D, Wadsworth LC (1999) Corona treatment of polyolefin films—a review. Adv Polym Technol 18(2):171–180

Sung Kwon C, Hyejin M, Chang-Jin K (2003) Creating, transporting, cutting, and merging liquid droplets by electrowetting-based actuation for digital microfluidic circuits. J Microelectromech Syst 12(1):70–80

Thorsen T, Maerkl SJ, Quake SR (2002) Microfluidic large-scale integration. Science 298:580–584

Thorslund S, Nikolajeff F (2007) Instant oxidation of closed microchannels. J Micromech Microeng 17(4):N16–N21

Unger MA, Chou HP, Thorsen T, Scherer A, Quake SR (2000) Monolithic microfabricated valves and pumps by multilayer soft lithography. Science 288:113–116

Washburn EW (1921) The dynamics of capillary flow. Phys Rev 17(3):273

Whitesides GM (2006) The origins and the future of microfluidics. Nature 442(7101):368–373

Whitesides GM, Stroock AD (2001) Flexible methods for microfluidics. Phys Today 54(6):42–48

Yeo LY, Hou D, Maheshswari S, Chang HC (2006) Electrohydrodynamic surface microvortices for mixing and particle trapping. Appl Phys Lett 88(23):233512

Zenkiewicz M (2005) Oxidation of the filled-polyolefin-film surface layer by corona treatment. Przem Chem 84(10):733–739